

MASTER

EEG analysis in full-term neonates
spectral analysis of medication in stroke patients and 3D source

Dankers, F.J.W.M.

Award date:
2012

[Link to publication](#)

Disclaimer

This document contains a student thesis (bachelor's or master's), as authored by a student at Eindhoven University of Technology. Student theses are made available in the TU/e repository upon obtaining the required degree. The grade received is not published on the document as presented in the repository. The required complexity or quality of research of student theses may vary by program, and the required minimum study period may vary in duration.

General rights

Copyright and moral rights for the publications made accessible in the public portal are retained by the authors and/or other copyright owners and it is a condition of accessing publications that users recognise and abide by the legal requirements associated with these rights.

- Users may download and print one copy of any publication from the public portal for the purpose of private study or research.
- You may not further distribute the material or use it for any profit-making activity or commercial gain

EEG analysis in full-term neonates:

Medication effects
&
3D source localization

Frank Dankers
February 2012

Master's thesis

Graduation period: March 2011 – February 2012

Student number: 552109

Eindhoven University of Technology

Faculty of applied physics

Graduation performed at:

Máxima Medical Center, Veldhoven

Supervisors:

Dr. W. Jennekens (TU/e, MMC)

Dr. P. Andriessen (MMC)

Prof.dr.ir. P.F.F. Wijn (TU/e, MMC)

Abstract

Perinatal encephalopathy, is an important cause of neonatal morbidity and mortality. The electroencephalogram (EEG) is a critical diagnostic tool for detecting brain injury shortly after birth. In clinical practice, longitudinal bed-side monitoring is performed by the amplitude-integrated EEG (aEEG), which is a time-compressed version of the EEG measured using four electrodes. Perinatal encephalopathy is often accompanied by seizure activity, which is treated with antiepileptic drugs (AEDs). It is well known that AEDs can actively change (a)EEG characteristics, which may hamper interpretation of the (a)EEG and assessment of brain injury.

The first aim of this study is to quantify the effects of two common AEDs, midazolam and lidocaine, on EEG spectral power for full-term infants presenting with seizures after perinatal arterial ischemic stroke (PAIS). The patient group consists of 12 full-term neonates with PAIS, undergoing multi-channel EEG and aEEG recordings, and receiving midazolam and/or lidocaine for seizure control. Spectral analysis using the Fourier transform is performed on 4-hour EEG segments surrounding the time of AED administration. Artifacts are detected and omitted from analysis by restrictions of frequency power. The frequency spectrum is divided in δ (1-4 Hz), θ (4-8 Hz), α (8-13 Hz) and β (13-30 Hz) frequency bands. This is the first study investigating the spectral effects of AEDs in neonates.

The results of the spectral analysis show that both drugs induce a shift from low to high frequency electrocortical activity. For lidocaine, the effects are more pronounced in the stroke-affected hemisphere. Additionally, midazolam reduces total EEG power. These spectral changes differ from those seen in adult studies. aEEG data shows that midazolam has a low seizure suppression effectiveness, whereas lidocaine is highly effective in terminating seizures.

Early detection of neonatal encephalopathy is important to timely enact treatment and prevent additional brain injury. EEG can be recorded immediately following birth, whereas MRI is typically available one week after birth. 3D source localization of neonatal EEG data might provide additional information about possible encephalopathy in the early stage. Therefore, the second aim of this study is to evaluate the monitoring feasibility of EEG source localization by standardized weighted low resolution brain electromagnetic tomography (swLORETA) in full-term newborns with hypoxic-ischemia. Three representative examples of neonatal hypoxic-ischemia are included. EEG source localization results are compared with magnetic resonance imaging (MRI) data obtained within the same day of EEG recording. Source localization is calculated for a generic anatomical head model from EEGs recorded with 19 scalp electrodes, placed according to the international 10-20 EEG montage. This is the first study investigating monitoring capabilities of EEG source localization in neonates.

The results of the EEG source localization show that regions of low signal intensity on 3D swLORETA inverse solutions correlate well with hypoxic-ischemic areas, as are visible on MRI. In addition, neonatal seizure activity may be localized using swLORETA. Furthermore, the results indicate that the current implementation may be less sensitive for WM lesions. The calculated current density probability distributions may provide easy-to-interpret localized information about neonatal brain function, which may enable detailed longitudinal monitoring and potential assessment of treatment efficacy. Additionally, since EEG data are available from the first day after birth, whereas MRI data are typically available one week after birth, EEG source localization may allow early diagnosis of possible encephalopathy in neonates.

Contents

Abbreviations	vii
1 Introduction	1
2 Theory	3
2.1 Anatomy of the brain	3
2.1.1 Main anatomical features	3
2.1.2 Cerebral blood flow	6
2.1.3 Cellular structure.....	7
2.1.4 Origin of the EEG	10
2.2 EEG acquisition.....	11
2.2.1 International 10-20 system	11
2.2.2 Full 10-20 EEG.....	12
2.2.3 Amplitude-integrated EEG.....	12
2.3 EEG spectral analysis	14
2.3.1 Fourier transform	14
2.3.2 Spectral leakage	14
2.3.3 Filters	16
2.4 EEG spectral properties	18
2.4.1 Frequency bands	18
2.4.2 Band powers	18
2.4.3 Artifacts.....	19
3 Spectral effects of antiepileptic drugs in perinatal stroke	21
3.1 Introduction	21
3.2 Theory.....	21
3.2.1 Types of medication.....	21
3.2.2 Medication protocol	22
3.3 Methods	22
3.3.1 Patient group.....	23
3.3.2 Data acquisition	23
3.3.3 Data analysis.....	24
3.3.4 Statistics	26
3.4 Results.....	27

3.4.1	aEEG	27
3.4.2	EEG spectral analysis.....	29
3.5	Discussion	34
3.5.1	aEEG	34
3.5.2	EEG spectral analysis.....	34
3.5.3	Limitations.....	35
3.6	Conclusion	37
4	swLORETA source localization	39
4.1	Introduction	39
4.2	Theory	39
4.2.1	Inverse problem	39
4.2.2	swLORETA.....	39
4.3	Methods	40
4.3.1	Patient group.....	40
4.3.2	Data acquisition	42
4.3.3	Data analysis.....	42
4.4	Results.....	45
4.5	Discussion	51
4.6	Conclusion	53
5	Summary	55
6	Recommendations	57
Appendix A	Classification of aEEG	59
Appendix B	Midazolam spectral power values	63
Appendix C	Lidocaine spectral power values	65
Appendix D	Literature on EEG spectral effects of AEDs	67
Appendix E	The forward problem	69

Abbreviations

A/D	analog to digital
ACA	anterior cerebral artery
ADC	apparent diffusion coefficient
AED	antiepileptic drug
aEEG	amplitude-integrated electroencephalogram
BS	burst suppression
CLV	continuous low voltage
CNS	central nervous system
CNV	continuous normal voltage
CT	computed tomography
DFT	discrete Fourier transform
DNV	discontinuous normal voltage
DWI	diffusion-weighted imaging
ECG	electrocardiogram
EEG	electroencephalogram
EMG	electromyogram
EPSP	excitatory postsynaptic potential
FFT	fast Fourier transform
FT	flat trace
GABA	gamma-aminobutyric acid
GM	gray matter
HIE	hypoxic-ischemic encephalopathy
IPSP	inhibitory postsynaptic potential
IQR	interquartile range
LGN	lateral geniculate nuclei
LORETA	low resolution brain electromagnetic tomography
MCA	middle cerebral artery
MRI	magnetic resonance imaging
nCPAP	nasal continuous positive airway pressure
NICU	neonatal intensive care unit
PAIS	perinatal arterial ischemic stroke
PCA	posterior cerebral artery
SEF	spectral edge frequency
swLORETA	standardized weighted low resolution brain electromagnetic tomography
US	ultrasound
WM	white matter

1 Introduction

The birth of a child is a highly dynamic and complex process and is therefore sensitive for a variety of complications. One of these complications is perinatal encephalopathy, or brain injury, which is responsible for a large number of neonatal mortalities each year. Critical factors in development of encephalopathy are genetic abnormalities, preterm birth, perinatal asphyxia, hemorrhage and cerebral infarction. Reduced cerebral blood flow can lead to hypoperfusion of brain tissue, i.e. an insufficient supply of freshly oxygenated blood to the brain. In the neonate this is termed perinatal asphyxia or hypoxic-ischemic encephalopathy (HIE) and occurs in 3 to 9 of 1000 live births [1]. Cerebral infarction occurs in 1 of 5000 live births [2] and can also lead to rapid loss of brain function. An extensive review study covering 30 years has shown that following perinatal stroke 40% of the neonates developed normally, 57% had motor and/or cognitive disorders and 3% died [3].

Hypoxic-ischemia develops rapidly following a lack of oxygen to brain tissue. In the ischemic core there is immediate cell necrosis resulting in irrevocable loss of brain function in this area. The penumbra surrounds the ischemic core and undergoes delayed cell necrosis within five hours following the ischemic event. Rapid diagnosis is therefore critical to allow immediate treatment so that additional cell necrosis can be prevented.

Identification of neonates at risk of encephalopathy is started immediately after birth by use of clinical scoring systems. The Apgar scoring system is used to assess general health of the neonate and is based on skin color, pulse rate, reflex irritability, muscle tone and breathing [4]. The test is performed at 1, 5 and 10 minutes after birth, and scores range from 0 to 10. Prognosis of neonates with scores below 3 is poor, whereas a score of 7-10 represents a good prognosis. The Sarnat scoring system is another common test that is performed to assess grades of HIE based on clinical and EEG findings [5]. Possible grades are I, II and III, indicating mild, moderate and severe HIE respectively.

Clinical scoring can be followed by several imaging modalities and functional monitoring. Possible modalities are ultrasound (US), computed tomography (CT), magnetic resonance imaging (MRI), electroencephalogram (EEG) and amplitude-integrated EEG (aEEG). Cranial US is cheap and readily available, but spatial resolution and contrast is low compared to MRI. Cranial CT has been used widely before the advent of MRI and is sensitive for detection of hemorrhage and stroke, but involves high radiation exposure to the neonate. MRI does not require ionizing radiation, but is less sensitive to brain injury shortly after birth. Diffusion-weighted MRI (DWI) is most sensitive at 2 to 4 days after birth and conventional T₁- and T₂-weighted imaging reaches peak sensitivity at 1 week after injury [6]. MRI is also expensive, requires transportation of the neonate and sedation is necessary due to long measuring times.

Imaging modalities are useful for diagnosis and prediction of outcome, but not until 24 hours or more after birth. Functional monitoring with (a)EEG is a critical diagnostic tool since it is sensitive for brain injury shortly after birth [7]. EEG provides spatial information on background activity, seizure activity, antiepileptic drug (AED) effectiveness and possible occurrences of abnormal transients. The aEEG is a time-compressed version of a single- or two-channel EEG and is used for continuous bed-side monitoring of at-risk neonates. It does not provide the localization of abnormalities, but background and seizure activity are easily assessed. Both aEEG and EEG have been shown to be predictive of outcome in asphyctic neonates [8-12]. In summary, Apgar and Sarnat scores are determined immediately after birth. Continuous monitoring of aEEG is also started immediately for at-risk neonates. US and EEG

measurements can be performed from the first day of life for additional diagnostic information. Finally, MRI is typically performed at the end of the first week of life.

Treatment strategies are started at the onset of clinical symptoms of brain injury, e.g. lowered EEG background activity or seizure activity. Seizures occur in approximately 3 per 1000 live births [13]. They are a consequence of underlying encephalopathy, but are believed to actively contribute to ongoing brain injury [14, 15]. Treatments therefore focus on the suppression of seizure activity by use of AEDs. It is well known that AEDs can actively change (a)EEG characteristics, which may hamper interpretation of the (a)EEG and assessment of brain injury. A correct understanding of the effects of AEDs is therefore important.

Studies into predictors for neurological disease have mainly focused on imaging modalities, e.g. MRI-based techniques, and longitudinal (a)EEG monitoring. The topic of 3D reconstruction of electrical sources in the brain, which are responsible for the measured EEG activity, has attracted increased attention in recent years, due to advances of models reducing source localization errors [16-18]. However, studies have mainly been limited to adults, and source reconstruction is not frequently used in newborns because of technical difficulties, e.g. lack of data concerning the newborn skull conductivity, thickness and homogeneity [19]. Since EEG is sensitive for brain injury immediately after birth, source reconstruction of the EEG might provide 3D localization information of encephalopathy at a very early stage, when MRI data are typically unavailable.

Aims and outline

This thesis has two important aims. Neonates with perinatal encephalopathy are monitored by (a)EEG. If neonatal seizures are present, they are treated with AEDs. However, these AEDs change the characteristics of the (a)EEG and this may hamper the clinical interpretation of the (a)EEG. A correct understanding of the effects of AEDs on (a)EEG is therefore important. The **first aim** of this study is to quantify the effects of two common AEDs, midazolam and lidocaine, on EEG spectral power for full-term infants presenting with seizures after perinatal arterial ischemic stroke (PAIS).

Additionally, early detection of neonatal encephalopathy is important for the quick enactment of treatment, in order to prevent ongoing brain injury. EEG recordings are readily available shortly after birth, whereas MRI typically is not. Therefore, the 3D source localization of EEG recordings might provide additional information about possible brain injury. The **second aim** of this study is to evaluate the monitoring feasibility of EEG source localization by standardized weighted low resolution brain electromagnetic tomography (swLORETA) in full-term newborns with HIE.

In **Chapter 2**, the anatomy of the brain is explained as well as acquisition and analysis techniques of (a)EEG. In **Chapter 3**, the effects of AEDs (midazolam and lidocaine) on EEG spectral power are quantified for full-term infants presenting with seizures after perinatal arterial ischemic stroke (PAIS). Additionally, the effects of these AEDs are also quantified for aEEG recordings. In **Chapter 4**, the feasibility of monitoring applications of 3D source localization by swLORETA is investigated in full-term neonates with HIE. In **Chapter 5**, the results from previous chapters are summarized and recommendations are given in **Chapter 6**.

2 Theory

2.1 Anatomy of the brain

2.1.1 Main anatomical features

The human brain (encephalon) comprises the upper part of the central nervous system (CNS). It exerts centralized control over all other organs of the body. It receives and processes sensory inputs, maintains motor control of body movements and controls the autonomic nervous system. The main anatomical features of interest in this study are located in the cerebrum, which is attached to the brain stem, see Figure 2.1 and Figure 2.2.

The cerebellum is located below the cerebrum and behind the brainstem. Unlike the cerebral cortex its surface is made of parallel fine grooves. It plays an important role in motor coordination, precision, timing and learning. Damage to the cerebellum does not directly result in paralysis, but produces problems of fine movement. Functional imaging studies have shown that the cerebellum is not only connected to motor-specific areas of the cerebral cortex, but also plays an important role in learning, attention and mental imagery [20-22].

The cerebrum, or telencephalon, comprises the most superior part of the CNS. It consists of two approximately symmetric hemispheres and can be subdivided into the cerebral cortex, limbic system and basal ganglia (i.e. the caudate nucleus and putamen). Since the cerebrum consists of many sub-regions, which have a wide variety of different functions, these regions will be discussed separately.

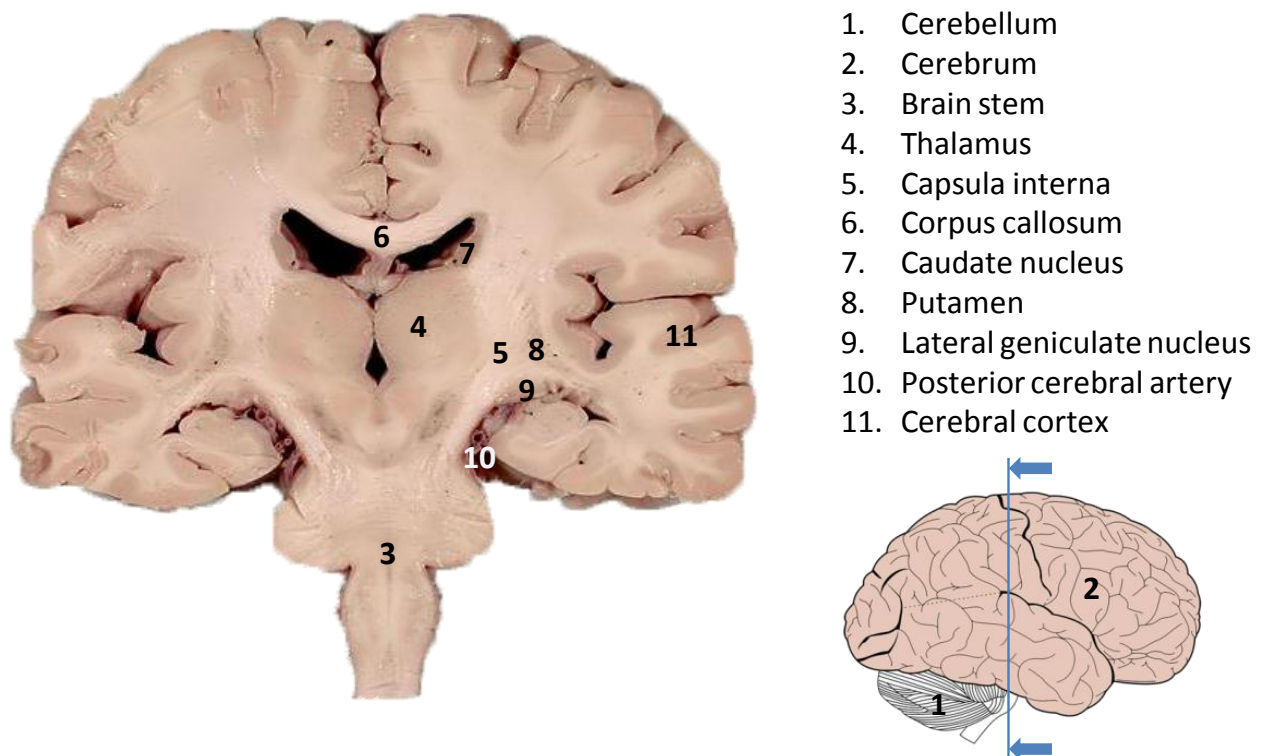


Figure 2.1: Overview of the main anatomical regions in the human brain.

The thalamus is a mass of gray matter (GM) located in the middle of the brain and functions as a processing and relay station. It consists mainly of long projection neurons connecting subcortical areas with the entire cerebral cortex. All sensory information, except for the olfactory system (sense of smell) is relayed to the cortex by the thalamus. The thalamus also regulates the different states of sleep and wakefulness and it is believed to be involved in generating consciousness through the thalamo-cortical circuitry.

The internal capsule, or *capsula interna*, is a V-shaped tract of white matter (WM) separating thalamus and caudate nucleus from the putamen (Figure 2.2). The flexure of the V is called the *genu* and connects the anterior and posterior limb of the internal capsule. The anterior limb consists of frontopontine fibers connecting the frontal cortex to the pons inside the brainstem. Additionally, it contains thalamo-cortical fibers connecting the thalamus with the frontal cortex. The posterior limb contains corticospinal fibers, connecting the spinal cord with the cerebral cortex.

The corpus callosum is the largest mass of WM in the brain and is situated beneath the GM of the cortex. This large bundle of nerve fibers connects the left and right hemispheres facilitating interhemispheric communication. The anterior portion is called the genu of the corpus callosum and the posterior part is called the splenium. Agenesis (i.e. an underdevelopment) of the corpus callosum can lead to a number of disorders, e.g. seizures, motor problems and visual and auditory memory problems.

The caudate nucleus, or *nucleus caudatus*, is a C-shaped curved mass of GM and is part of the basal ganglia. Two caudate nuclei exist; each hemisphere contains one bordering the thalamus. It consists of a large anterior head and an elongated posterior tail. The caudate has long been believed to be involved in motor behavior, but more recently has also been shown to be highly involved in learning and memory tasks [23].

Connected to the anterior limb of the caudate nucleus is the putamen and together they are referred to as the dorsal striatum. The putamen, like the caudate nucleus, is made of GM and is also part of the basal ganglia. It contains feedback loops responsible for motor learning, performance and preparation [24, 25]. It releases several types of neurotransmitters, including gamma-aminobutyric acid (GABA), which control neural excitability. The putamen plays an important role in Alzheimer's, Huntington's and Parkinson's disease.

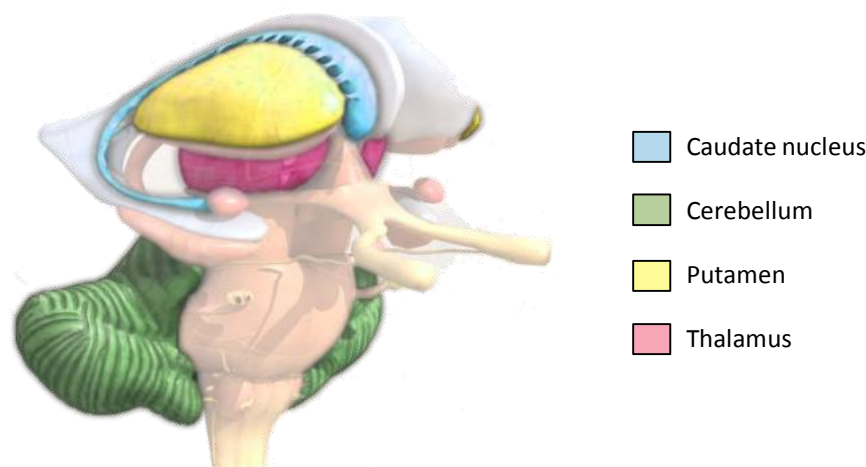


Figure 2.2: Orientation of caudate nucleus, cerebellum, putamen and thalamus. Image adapted with permission from Healthline BodyMaps™ [26], copyright © 2005-2012 Healthline Networks, Inc.

The visual system is depicted in Figure 2.3. Optic nerves originate from the eyes and cross each other in the optic chiasm. From there optic tracts travel to the lateral geniculate nuclei (LGN) residing on either side of the thalamus. The LGN are a sensory processing and relay nucleus and consist of six layers from which neurons originate, together called the optic radiation, which travel to the visual cortex at the most posterior part of the cerebrum.

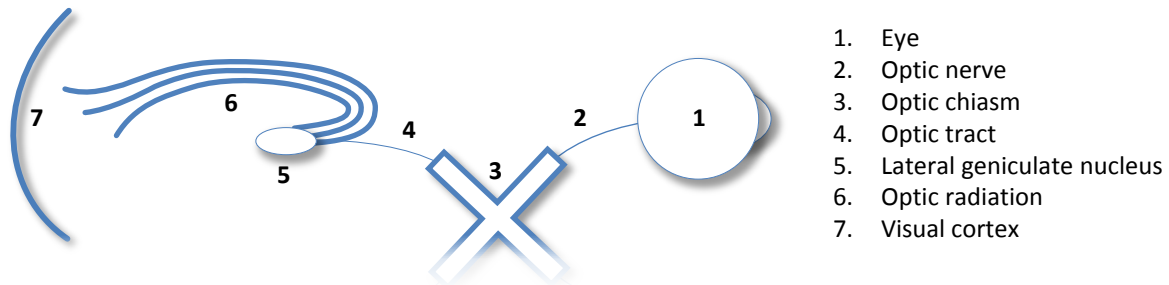


Figure 2.3: Schematic overview of the visual system. Visual signals are transferred through the optic nerve, chiasm and tract to the lateral geniculate nucleus. From here the optic radiation transfers the signal to the visual cortex at the posterior part of the cerebrum.

The outermost layer of the cerebrum is called the cerebral cortex. It consists of GM and is approximately 2-4 mm thick. It is connected with subcortical structures like the thalamus and the basal ganglia. The cerebral cortex is folded, the peaks are termed *gyri* and the troughs are termed *sulci*, and thus only a third of the cortex is located at the surface of the brain. The cortex contains a number of large sulci called fissures that divide it into lobes, see Figure 2.4. The frontal lobe is associated with higher mental functions, e.g. attention, short-term memory, planning and motivation. The temporal lobe is situated to the sides of the brain and is linked with auditory perception, speech and long-term memory. The parietal lobe is situated behind the frontal lobe and is related to sensory information processing and spatial aptitude. The occipital lobe is the most posterior part of the human brain. It contains the primary visual cortex and thus visual sensory information is processed in this region.

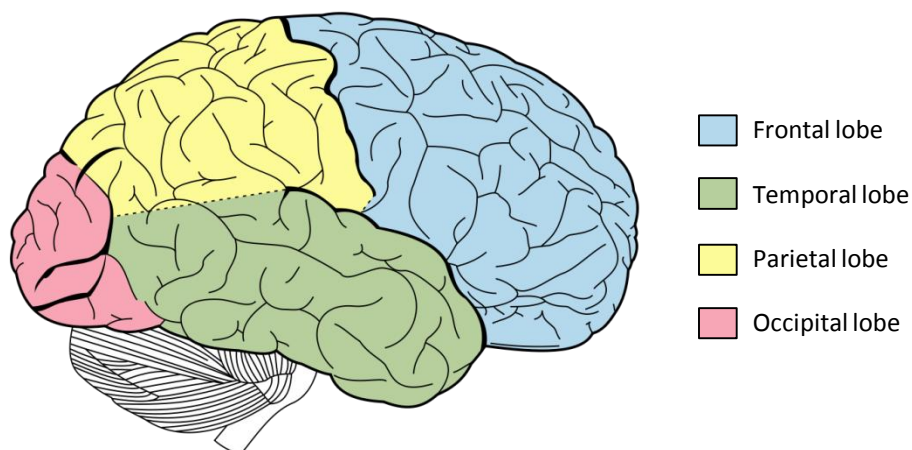


Figure 2.4: Classification of the cerebral cortex into lobes based on apparent fissures.

Ninety percent of the cerebral cortex is made up of the neocortex. It is an important region since it is linked with sensory information processing, motor planning, visual aptitude, language and conscious thought. It is made up of two types of neurons, 80% are excitatory pyramidal neurons and 20% are inhibitory interneurons that project their axons locally.

Classically, the neocortex is said to consist of six layers divided by cell type and neuronal connections, labeled I to VI (with VI the innermost layer). The number of layers as well as their thickness and cell types can vary depending on specific brain areas. Generally, layers I and II process non-thalamic information and project locally to other cortical areas. Layer III consists of pyramidal cells which project axons to distant areas within the neocortex. Layer IV consists of neurons that receive synaptic connections from thalamus and all other sensory areas and relay this information locally to other areas of the cortex. Layer V projects its axons outward to the brain stem, spinal cord and basal ganglia, whereas layer VI projects outward to the thalamus.

2.1.2 Cerebral blood flow

The human brain receives its blood from two main pairs of arteries: the internal carotid arteries and the vertebral arteries. A schematic overview depicting the main arteries that provide the cerebral blood flow is depicted in Figure 2.5. The internal carotid arteries branch into two anterior and two middle cerebral arteries (ACAs and MCAs). The vertebral arteries join to form the basilar artery at the brain stem and subsequently branches into two posterior cerebral arteries (PCAs). An arterial ring, called the Circle of Willis, is formed by communicating arteries; the anterior communicating artery connects both ACAs, and two posterior communicating arteries connect both MCAs with the PCAs. The Circle of Willis provides collateral blood flow in the event of a major cerebral artery occlusion.

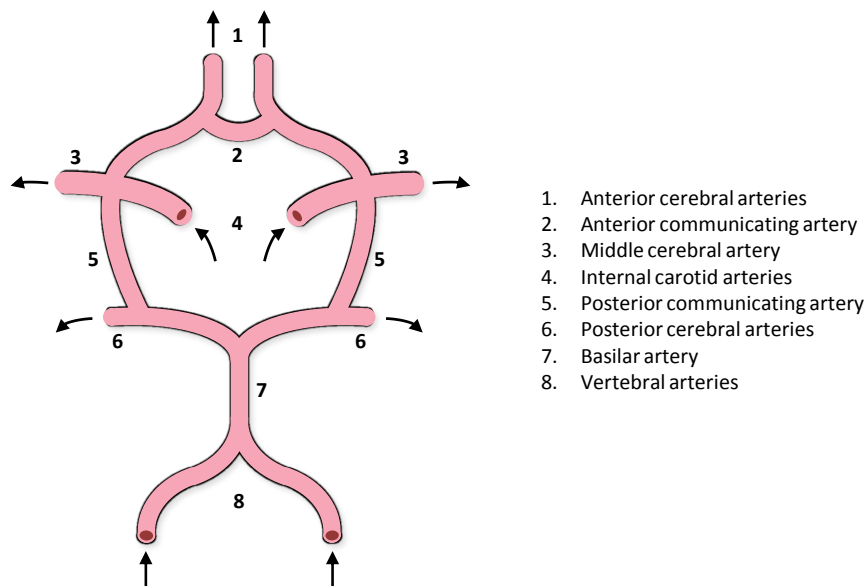


Figure 2.5: Major arteries providing cerebral blood flow in the brain. Blood is pumped towards the brain through the vertebral and internal carotid arteries and distributed within the brain by the anterior, middle and posterior cerebral arteries. An arterial ring, called the Circle of Willis is formed by additional communicating arteries. Flow direction is indicated by the arrows.

The approximate areas of the human brain provided with blood by the major cerebral arteries are depicted in Figure 2.6. The ACA provides blood to the medial parts of the frontal lobe and to the superior medial parts of the parietal lobe. It also supplies anterior parts of the corpus callosum, basal ganglia and internal capsule with blood. The MCA accommodates the bulk of the lateral hemispheres (i.e. both temporal and parietal lobes), with the exception of the most superior part of the parietal lobe (supplied by ACA) and the most inferior part of the temporal lobes (supplied by PCA). The MCA also provides blood to the basal ganglia and the internal

capsule. Finally, the PCA supplies the occipital lobe with blood as well as the inferior part of the temporal lobes.

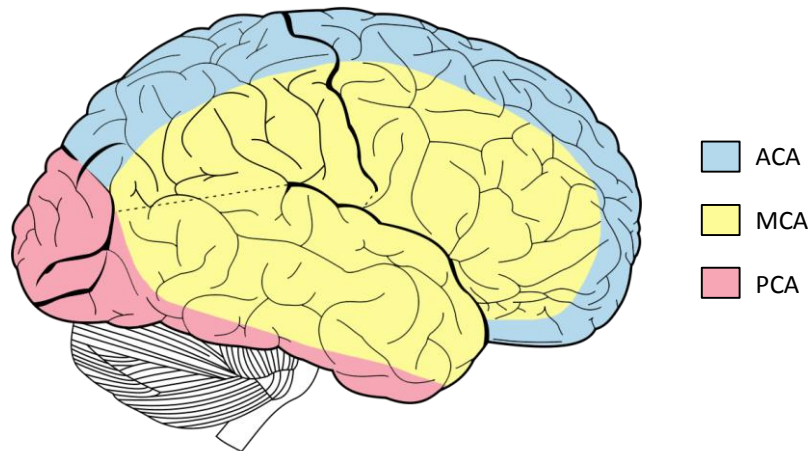


Figure 2.6: Blood supply to different areas of the brain as provided by the anterior cerebral arteries (ACAs), middle cerebral arteries (MCAs) and posterior cerebral arteries (PCAs). Note that the ACA provides blood not only to the frontal lobe, but also to large areas of the parietal lobe, and the PCA provides blood not only to the occipital lobe, but also to parts of the temporal lobe.

2.1.3 Cellular structure

The basic cell types of the CNS are neurons and glial cells. Neurons process and distribute information by electrical and chemical signaling. Functionally, they can be divided into afferent neurons (sensory neurons), receiving information from tissues and organs to the CNS, efferent neurons (motor neurons), transmitting impulses outwards from the CNS, and interneurons, which connect with other neurons inside the CNS.

Neurons consist of a cell body (soma), dendrites and an axon, see Figure 2.7. Dendrites are thin structures extending from the cell body for up to 100 micrometers and may branch multiple times. Their function is to receive signals from other neural cells and transmit them to the cell body. A single axon originates from the cell body, has a typical length of a millimeter and may also branch multiple times before terminating at dendrites or cell bodies of other neurons. Their function is to transmit neural signals to other cells. The axons of neural cells can be surrounded by a myelin sheath, produced by glial cells called oligodendrocytes, which serves as insulation and reduces ion leakage and cell membrane capacitance, and also increases impulse speed inside the axon. WM consists of these myelinated axons and glial cells, whereas GM is made of neuronal cell bodies, unmyelinated axons and dendrites. The typical white and gray colors originate from the appearance of the (un)myelinated axons after preservation in formaldehyde.

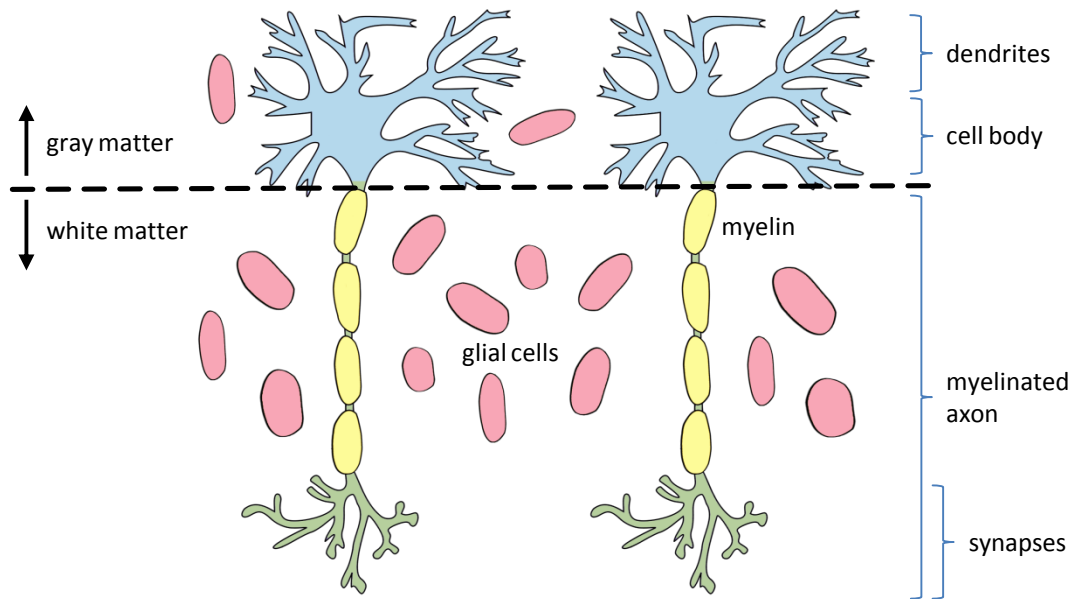


Figure 2.7: The neuron and its main constituents. The neuron receives its input via the dendrites and transmits its signals through the axon. The axon can terminate into a multitude of synapses that are connected to other neurons. The axons in WM are myelinated increasing impulse speed.

The extracellular space and the nerve fibers contain sodium (Na^+), potassium (K^+) and chloride (Cl^-) ions. Inside a nerve fiber there is an abundance of Cl^- resulting in a net negative charge, in the extracellular space there is more Na^+ and K^+ than Cl^- resulting in a net positive charge. This difference in ion concentrations causes the neurons to be electrically polarized; they maintain a membrane resting potential of $-70 \mu V$ with respect to the extracellular fluid. A signal inside a nerve fiber is simply a local charge reversal in the axon and adjacent extracellular fluid. The signal is transmitted by opening sodium gates at the head of the signal and potassium gates at the tail of the signal. This leads to an inflow of Na^+ at the front and an outflow of K^+ at the tail, resulting in the propagation of the local positively charged signal. This process is depicted in Figure 2.8. When the signal has passed, the resting state of the nerve is restored by metabolic pumps. The inversion of cell membrane potential is called the action potential. The positive feedback loop of continuously opening ion gates in the cell membrane, which propels the signal forward, is called the Hodgkin cycle [27].

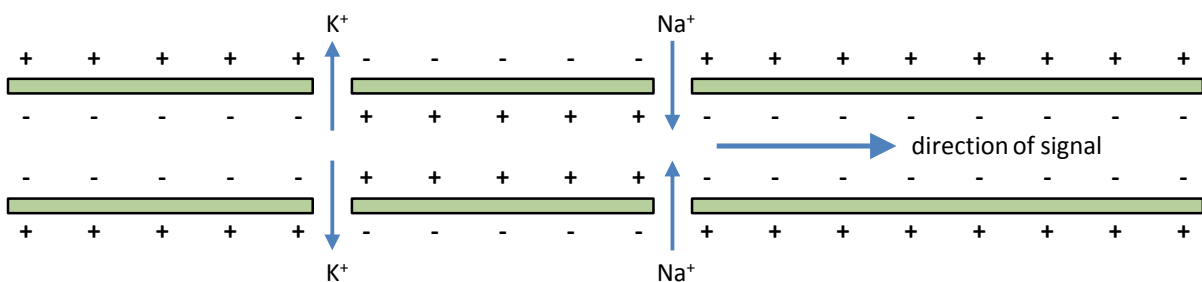


Figure 2.8: Signal propagation inside a nerve fiber. The signal consists of a local charge reversal and travels forward by the opening of sodium and potassium gates at the head and tail of the signal respectively.

The transmission of information between neurons occurs at junctions, called synapses, that are located at the endpoints of axons and connect with cell bodies or dendrites of other neurons, see Figure 2.9 (a). When a signal that travels along a nerve fiber reaches a synapse it

causes the release of neurotransmitters. These neurotransmitters have the ability to travel across the synaptic cleft and reach receptors that are located on the cell body or dendrite to which the synapse is connected, see Figure 2.9 (b). Neurotransmitters are either excitatory or inhibitory, encouraging or discouraging the target neuron from firing. They hyperpolarize (excitatory postsynaptic potential, EPSP) or depolarize (inhibitory postsynaptic potential, IPSP) the membrane potential of the target neuron. EPSPs and IPSPs have durations of approximately 1 second and spread over a small area of the membrane of the target neuron. This leads to a spatial and temporal summation of EPSPs and IPSPs and if a threshold of $-55 \mu\text{V}$ is surpassed the Hodgkin cycle is started and the target neuron will fire an action potential.

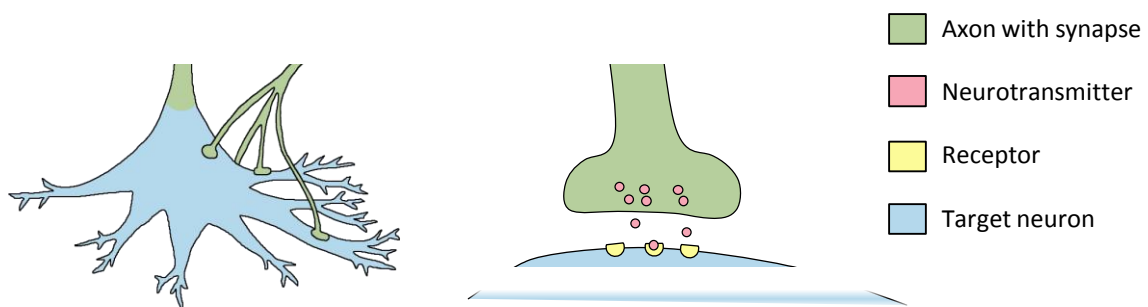


Figure 2.9: (a) The axon of a neuron projects to the cell body or dendrites of another neuron. The transmission of the electrical signals occurs at junctions called synapses. (b) When a signal reaches the synapse neurotransmitters are released that cause a local hyper- or depolarization of the cell membrane of the target neuron. If the spatial and temporal summation of these polarizations surpasses a certain threshold the target neuron will fire.

2.1.4 Origin of the EEG

The EEG measures electrical activity at the scalp, generated by electrically charged neurons in the brain. The cerebral sources of EEG potentials are 3D volumes of the cortex that produce 3D potentials inside the human brain. These potentials can then be measured by electrodes at the scalp as a 2D varying potential field. The main generator for EEG potentials is synaptic activity in the cerebral cortex [28]. In order to record cerebral electrical activity, the generator must be of sufficient strength and duration. The EPSPs and IPSPs, as produced by neurotransmitters in the synapse, cause intra- and extracellular currents that add up spatially and temporally, and form the main source for EEG activity. The extracellular current as produced by synaptic activity is shown in Figure 2.10.

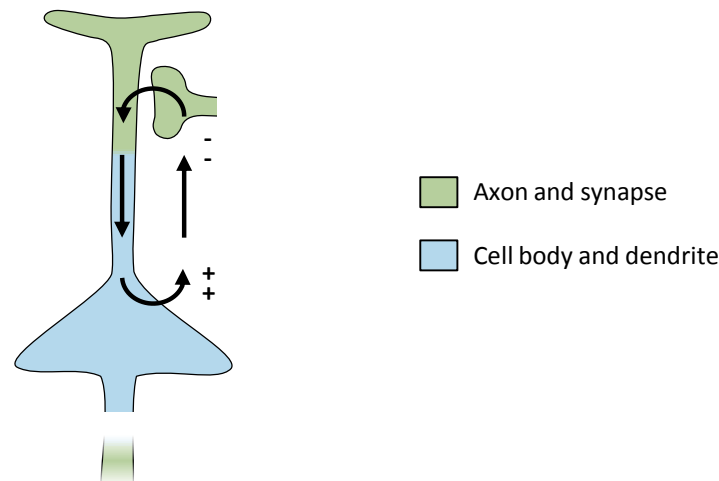


Figure 2.10: An extracellular current is generated by synaptic activity. Spatial and temporal summation of a multitude of these extracellular currents leads to detectable EEG activity.

A special type of neuron, called a pyramidal cell, is the largest contributor to EEG activity. These neurons are situated in the neocortex, i.e. the layer closest to the scalp, and are mostly orientated perpendicular to the surface of the cerebral cortex. Since one third of the cerebral cortex is orientated tangentially to the scalp (two thirds is situated deeper inside the brain due to cortical folding) a large number of pyramidal cells are perpendicularly orientated with respect to the scalp. The extracellular current produced by these pyramidal cells can thus be recorded by scalp electrodes, whereas tangentially orientated neurons would not result in a net voltage change at the scalp. Hämäläinen *et al.* have calculated that typical cluster sizes of simultaneously active synapses of 40-200 mm² are necessary for generating experimentally measured current densities of 100-250 nA/mm² [29]. Others have proposed that 108 simultaneously active neurons in an area of 600 mm² are necessary to produce visible EEG activity [28].

Subcortical structures are also believed to have a measurable effect on EEG activity. The thalamus is considered to be an EEG rhythm generator since it is highly connected with the cerebral cortex through the extensive thalamo-cortical circuits. It plays an important role in regulating different states of sleep and wakefulness and this has a measurable effect in EEG recordings [30].

2.2 EEG acquisition

2.2.1 International 10-20 system

The international 10-20 system is a standardized method for placing EEG scalp electrodes at fixed positions on the head of a patient based on anatomical landmarks [31, 32]. It allows for reproducible EEG measurements and ensures that scalp electrode placement is identical between different studies and results can be compared with each other. The electrode locations correspond to distinct underlying areas of the cerebral cortex. The distances between electrodes are either 10% or 20% of the left-right or front-back distance from the skull.

A graphical representation of the 10-20 system is shown in Figure 2.11. Two initial landmarks are used as reference for all scalp electrode placements. These are the nasion, located between the nose and the forehead, and the inion, the lowest point of the skull on the back of the head which is commonly identifiable by a bump. The line connecting these two points is referred to as the midline. Scalp electrode locations are spaced apart either 10% or 20% of the length of the midline or the line connecting the ears. Names of electrodes consist of a combination of a letter and a number. The letter corresponds to the lobe: *F* is frontal (and *Fp* is frontopolar), *T* is temporal, *C* is central (part of the parietal lobe), *P* is parietal and *O* is occipital. Referential electrodes are commonly attached to the earlobes, indicated by the letter *A*. Even numbers correspond to the right hemisphere, odd numbers to the left hemisphere. Higher numbers correspond with increasing distance from the midline and *z* refers to zero, i.e. placed on the midline. The actual number of electrodes used in EEG measurements can differ depending on the amount of spatial resolution that is desired. When an EEG is recorded with 9 electrodes (marked in green in Figure 2.11) this is commonly referred to as the reduced 10-20 system.

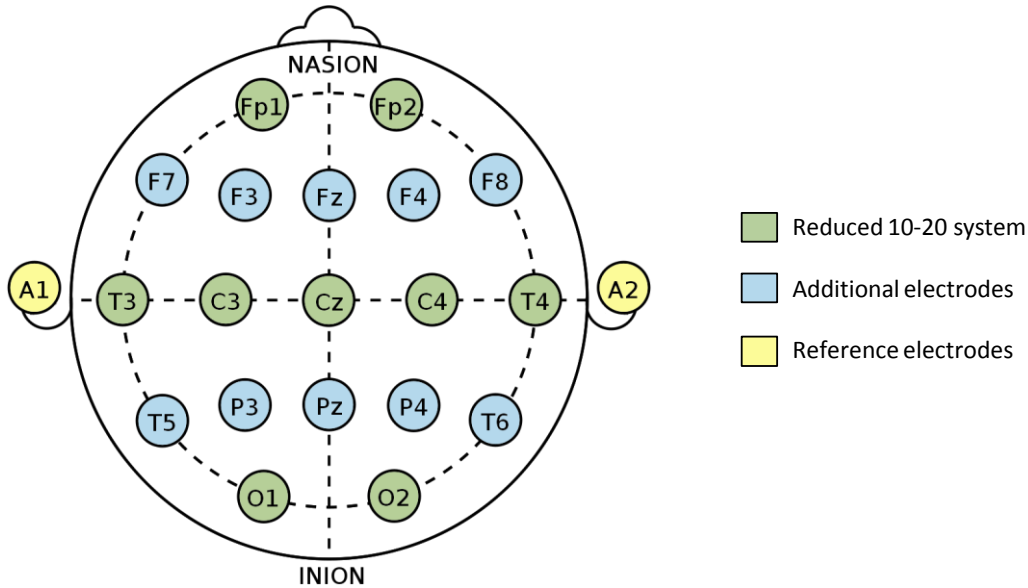


Figure 2.11: The international 10-20 system that is used for consistent scalp electrode placement based on anatomical landmarks of the head. The green electrodes, commonly called the reduced 10-20 system, refer to a minimum of 9 scalp electrodes which are used in the spectral analysis study of this thesis. The additional blue electrodes result in a total of 19 scalp electrodes which are used for the 3D source localization study of this thesis. The two pink electrodes are reference electrodes placed on the earlobes of a patient.

Electrocortical activity is derived from the electrode signals by use of a montage that combines the voltages measured by the electrodes to enhance relevant signals and suppress noise. Different montages can result in highly different representations of the EEG. Changing

from one montage to another is always possible, since any montage can be derived mathematically from another. The three most common montages are:

- Common reference montage: A referential electrode is placed on a patient at a location where EEG activity is minimal, e.g. the earlobes or mastoids, and this signal is subsequently subtracted from all other scalp electrodes.
- Average reference montage: A reference signal is calculated by averaging the signal from all scalp electrodes and this reference is then subtracted from all scalp electrodes.
- Bipolar montage: The output voltage is calculated by subtracting two adjacent electrodes.

The bipolar montage is chosen in this study as it is used most often in clinical practice.

2.2.2 Full 10-20 EEG

When detailed and local information on the electrocortical information of a patient is required, a full 10-20 EEG can be made, e.g. in neonates with suspicion of brain injury. Electrodes are placed according to the international 10-20 system (described in section 2.2.1). The number of electrodes can vary. Commonly, 9 scalp electrodes are used for neonates, and this is termed the reduced 10-20 system. The number of electrodes can be increased to 19 scalp electrodes for higher spatial resolution. Measurements are usually around 30 minutes long. For diagnostic purposes it is common to investigate the spectral content of an EEG. A full 10-20 EEG provides spatial information on background activity, seizure activity, AED effectiveness and can show the possible occurrence of abnormal transients. These abnormal EEG transients appear to be an important prognostic indicator [33].

2.2.3 Amplitude-integrated EEG

The aEEG is a highly compressed representation of a patient's EEG, commonly recorded with four electrodes. This method and the first clinical device, referred to as a cerebral function monitor, have initially been developed by Maynard *et al.* around 1970 [34, 35]. Its primary use was continuous electrocortical monitoring in adults with *status epilepticus*, cardiac arrest or during anesthesia. In the early 80s it became clear that the method was of value in the continuous monitoring of neonates with encephalopathy or seizures. Several studies have shown that aEEG measurements are a good predictor of outcome [7, 11, 12, 36, 37]. Studies on AED effectiveness have also been performed with aEEG [38-41]. Currently, aEEG is widely used as a continuous bed-side monitoring tool for at-risk neonates. When detailed spatial information of electrocortical activity is required a complete 10-20 EEG can be recorded, as described in section 2.2.2.

It is common practice to perform EEG measurements for both hemispheres simultaneously for construction of the aEEG. This makes it possible to assess interhemispheric asymmetry, especially useful in neonates with unilateral stroke (i.e. restricted to one hemisphere). Signals are usually recorded from electrodes at F3-P3 and F4-P4, see Figure 2.11. The acquired signals are amplified and processed by an asymmetric band-pass filter, suppressing frequencies below 0.5 Hz and above 30 Hz, since little electrocortical activity and mainly artifacts are situated outside this frequency range (e.g. sweating, movement, muscle artifacts and electrical interference). Then, the amplitude of the signals is compressed on a semi-logarithmic scale, rectified and smoothed and a large time compression is applied (sample frequency $\rightarrow 1/60$ Hz).

An example aEEG is displayed in Figure 2.12. On continuous function monitors, this signal is typically displayed together with the EEG and the electrode impedance. The bandwidth of the aEEG reflects variations in the minimum and maximum amplitude of the signal. Based on these values, a classification of aEEG background patterns has been agreed upon [37, 42-44]. The five possible backgrounds are continuous normal voltage (CNV), discontinuous normal voltage (DNV), continuous low voltage (CLV), burst suppression (BS) and flat trace (FT). Seizure activity can be classified as single seizures, repetitive seizures or *status epilepticus* [44]. For an overview of background and seizure classifications and example data see Appendix A.

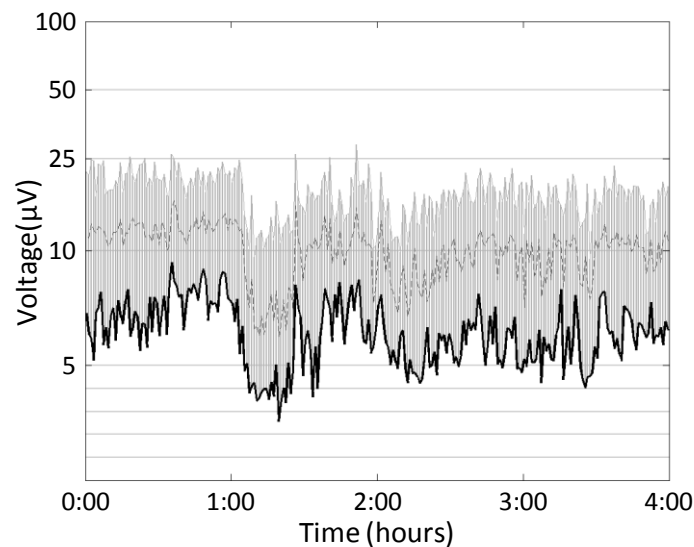


Figure 2.12: An example of an aEEG signal. Note the large time compression along the x-axis and the semi-logarithmic scale on the y-axis. The background pattern of this aEEG is classified as CNV with a brief moment of DNV during the second half of the first hour. See Appendix A for a full classification of all categories.

One of the main advantages of the aEEG is the easy interpretation of the EEG background pattern and the detection of electrographic seizures. It requires significantly less skill to interpret an aEEG than a full EEG and it is relatively easy to acquire. It can also help in evaluating the effectiveness of AED administration. Furthermore, it allows for long-term bedside monitoring (e.g. spanning multiple days) and the prediction of outcome. However, not all seizures are detected by aEEG, e.g. frontal seizures can be missed. Secondly, apart from interhemispheric asymmetry, it does not provide local information in contrast with a full EEG. Therefore, an aEEG does not replace a full EEG, which is still required when complete and local information is desired about the electrocortical activity of a patient, but it is excellent for monitoring tasks.

2.3 EEG spectral analysis

2.3.1 Fourier transform

A powerful tool for the investigation of EEG properties is spectral analysis. The EEG frequency spectrum can be obtained by applying the Fourier transform. It is used to decompose a signal into its spectral components, yielding a frequency domain representation or spectrum of the signal. The Fourier transform of a continuous signal $x(t)$ is defined as

$$X(f) = \int_{-\infty}^{+\infty} x(t) e^{-i2\pi ft} dt \quad \text{Eq. 2.1}$$

with f the frequency and t the time. The amount of power at different frequencies present in a signal can be found by computation of the power spectrum, which is defined as

$$P(f) = X(f) \overline{X(f)} = |X(f)|^2 \quad \text{Eq. 2.2}$$

where $\overline{X(f)}$ denotes the complex conjugate of $X(f)$. These equations are used for continuous signals, but in practice signals are sampled at discrete time points. To obtain the frequency spectrum of a discrete signal $x[n]$ the discrete Fourier transform (DFT) is used. This transform is defined as

$$X[n] = \sum_{k=0}^{N-1} x[k] e^{-i2\pi kn/N}, \quad n = 0, 1, \dots, N-1 \quad \text{Eq. 2.3}$$

If $x[n]$ consists of N samples the computation of the DFT requires $O(N^2)$ calculations. In order to speed up this process a collection of algorithms have been designed, commonly known as the fast Fourier transform (FFT). The FFT obtains the same result as the DFT, but at significantly less computation time when the number of samples equals 2^m (with integer m). For arbitrary segment lengths this can still be achieved by zero-padding; adding zeroes at the end of the segment, until the number of samples equals the next integer power of 2. The number of calculations is then of order $O(N \log N)$. Zero padding does not affect the spectral content or spectral resolution. The FFT applied in this study uses the Cooley-Tukey algorithm [45], which recursively breaks down a DFT into smaller DFTs, reducing the number of computations.

2.3.2 Spectral leakage

The FFT calculates the frequency spectrum by breaking down a DFT into smaller segments. It assumes that the signal is periodic in each segment, but this is generally not the case for measured signals. The calculation of the FFT of a non-periodic signal results in a localized spreading of the frequency components amongst neighboring spectral lines (i.e. bins), which is called spectral leakage [46]. In other words, it occurs when the signal is not exactly periodic with the length of the data block. The resulting effect is a broadening of the frequency peaks in the frequency spectrum.

Spectral leakage is undesired since it can obscure frequency peaks in the spectrum. It can be diminished by multiplying the segment with a window function prior to calculating the Fourier transform [47]. The amount of spectral leakage is determined by the size of the mismatch at the discontinuities on either side of the data block. Therefore, window functions often approach zero at the edges of the window to minimize spectral leakage.

Many different window functions exist and all have their own strengths and weaknesses [48]. Three windows are shown in time and frequency domain in Figure 2.13. The rectangular equals one inside the window, but has large discontinuities at the edges of the window, where it drops off to zero instantly. The Hann window is an elevated cosine and touches zero right before the edge of the window and therefore has no discontinuities. The Hamming window is also an elevated cosine, but it approaches a value of 0.08 at the edges of the window, allowing a small discontinuity.

The frequency responses of the three window functions best show their strengths and weaknesses (also displayed in Figure 2.13). A narrow main lobe, which is located at 0 Hz, corresponds with a high spectral resolution. The rectangular window outperforms the other windows in this regard. However, a narrow main lobe is accompanied by high side lobes, which cause spectral leakage, if the periodicity of the signal and length of the data block do not match. The Hamming and Hann windows perform better than the rectangular window in this regard. The Hamming window is slightly discontinuous, which results in a slower roll-off of the side lobes compared to the Hann window, but the first side lobe is lowered by 10 dB.

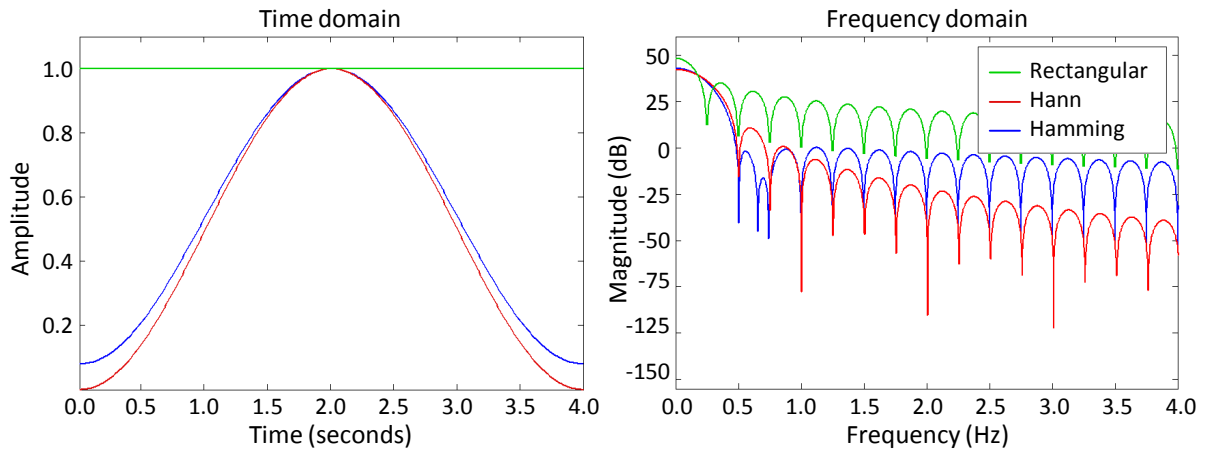


Figure 2.13: Three different window functions together with their frequency response. Note the wider main lobes of the Hann and Hamming window resulting in a lowered spectral resolution, but also the suppressed side lobes quenching spectral leakage.

The correct choice of window is determined by the input signal, which in this case is the EEG. Both Hann and Hamming windows provide adequate spectral resolution combined with decent spectral leakage suppression. For this study the Hamming window has been chosen because of the 10 dB additional suppression of the first side-lobe when compared to the Hann window [48]. The Hamming window is defined as

$$w(n) = 0.54 - 0.46 \cos\left(\frac{2\pi n}{N-1}\right), \quad n = 1, \dots, N \quad \text{Eq. 2.4}$$

with sample number n and total number of samples N .

All window functions, except the rectangular window, alter the amplitude of the signal. Applying the Fourier transform and calculating the power spectrum after multiplication with a window function will result in an incorrect estimation of that power. By calculating the power of the window function itself, it is possible to compute a correction factor that accounts for this effect (the correction factor as applied in this study is described in section 3.3.3).

Another drawback of applying windows that approach zero near the edges is the loss of signal near these areas. An improvement can be made by using overlapping windows. The parts of the signal that are near the edge of the window and get suppressed, are unaffected in the next window, since they are now close to the center. A larger overlap between windows results in a better spectral estimate, but increases the computation time (the values as applied in this study are described in section 3.3.3).

2.3.3 Filters

When performing EEG measurements the signal often contains artifacts, e.g. signal originating from the 50 Hz power line frequency. A digital filter can then be used to remove these unwanted frequencies from the sampled signal. The properties of a filter can be evaluated from their frequency response. Typical filters are low-pass filters, which can easily be converted to high-pass filters. Both can be used in conjunction to construct band-pass and band-stop filters. The passband refers to the frequencies that are transmitted, while the stopband refers to the frequencies that are suppressed. The transition from passband into stopband is termed the transition band, which it is centered on the cut-off frequency [47]. The frequency response of an ideal filter has the form of a step function at the location of this cut-off frequency, i.e. immediate roll-off without introducing artifacts in stop- or passband.

By plotting the frequency spectrum of different filter designs it is possible to assess their individual qualities. Figure 2.14 shows the frequency response of four common filters: Butterworth, Chebyshev type I/II and the elliptical filter. The Butterworth filter is a maximally flat type of Chebyshev filter without ripples in either the pass- or stopband [49]. Both Chebyshev filters achieve faster roll-off by allowing ripple in either the passband (type I) or the stopband (type II). The elliptical filter, also known as Cauer filter, has the steepest roll-off, but it has ripples in both pass- and stopband.

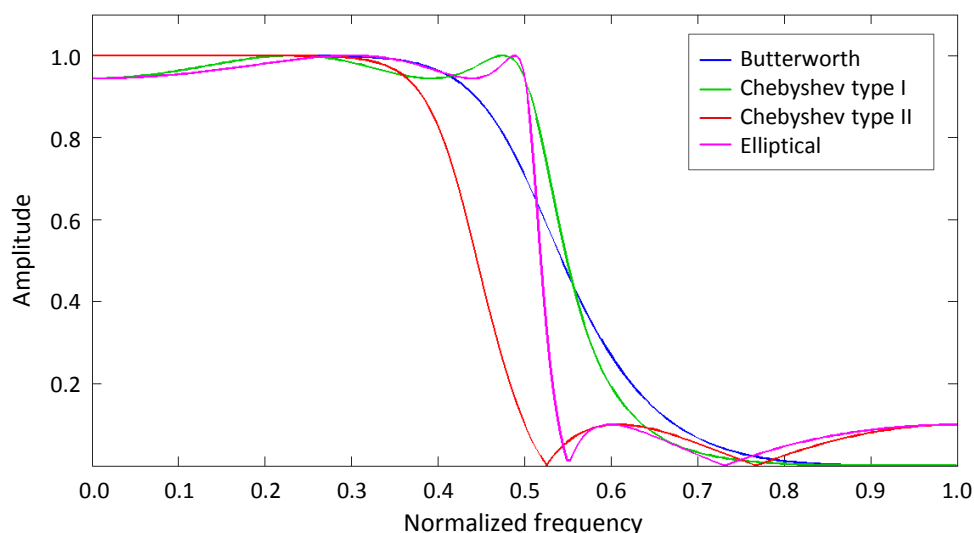


Figure 2.14: Frequency response of four different filter types. Steeper roll-off at the cut-off frequency comes with the added cost of ripples in either or both pass- and stopband.

Another method for increasing the filter steepness at the cut-off frequency is increasing the order of the filter. This results in faster roll-off, but also increases computation time. For example, the performance of the Butterworth filter for different filter orders is shown in Figure 2.15. The slope of the roll-off of this filter is $20n$ per decade, with n the filter order. The frequency response of an n^{th} order Butterworth filter is given by

$$|H(f)| = \frac{1}{\sqrt{1 + (f/f_c)^{2n}}} \quad \text{Eq. 2.5}$$

with frequency f , cut-off frequency f_c and order n .

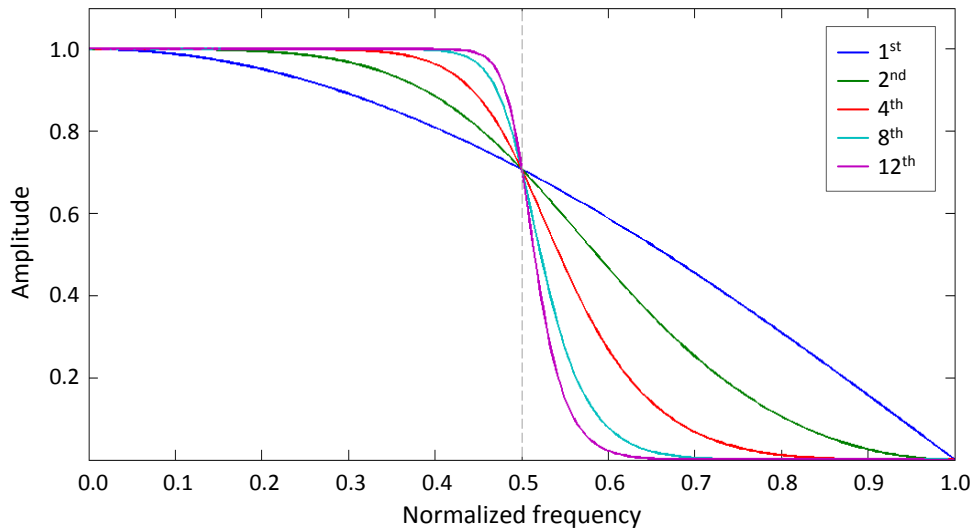


Figure 2.15: Frequency response for five different orders of Butterworth filters. Higher order increases roll-off steepness. Due to zero-phase filtering with 4th order Butterworth filters as applied in this study, the resulting filters are of order 8.

When choosing between different filters, a trade-off has to be made between filter steepness, filter artifacts and computation time. The filter of choice in this spectral study of neonatal EEG is the Butterworth filter. The absence of artifacts is favored over the increased steepness in the transition band with respect to the other filters. An adequate roll-off at the cut-off frequency is achieved by applying 4th order Butterworth filters. A detailed description of the different cut-off frequencies as applied in this study is given in section 3.3.3.

Using filters not only alters the amplitude of the frequency components, but also introduces an undesired phase shift. This can be nullified by using the zero-phase filtering technique; apply the filter twice, once in forward direction and once in backward direction [50]. The transfer function of a zero-phase filter is simply the square of the original transfer function, and the order is two times the original order. Since 4th order Butterworth filters are applied in this study, the resulting zero-phase filter is of order 8.

2.4 EEG spectral properties

2.4.1 Frequency bands

In clinical practice EEG frequency ranges are usually divided into different bands. The classification can differ slightly in literature, which can hinder direct comparison. The band definitions as adopted in this study are given in Table 2.1. Sometimes the very low frequency range of 0.5-1.0 Hz is separated into a distinct band, but this is not possible in the current study due to equipment limitations. Neonatal band power is mostly situated in the low frequency bands, i.e. the δ and θ bands.

Table 2.1: Classification of frequency bands in this study.

Frequency band	Range
δ	1-4 Hz
θ	4-8 Hz
α	8-13 Hz
β	13-30 Hz

2.4.2 Band powers

The power spectrum is calculated by multiplication of the Fourier spectrum with its complex conjugate, as described in section 2.3.1. The absolute power inside a frequency band is calculated by a simple sum of the powers at each frequency bin that falls within the range of the band. Relative band powers can be used for easy comparison between patients and are calculated by

$$P_{rel,band} = \frac{P_{band}}{P_{\delta} + P_{\theta} + P_{\alpha} + P_{\beta}} \cdot 100, \quad band = \delta, \theta, \alpha, \beta \quad \text{Eq. 2.6}$$

with P_{band} the power in one of the four bands. The calculated (relative) powers can also be normalized with respect to baseline values for easier detection of changes. This is defined as

$$P_{norm,band} = \frac{P_{band}}{P_{band,baseline}} \cdot 100, \quad band = \delta, \theta, \alpha, \beta \quad \text{Eq. 2.7}$$

where baseline is defined as the hour preceding administration of the AED. Finally, spectral edge frequency (SEF) is defined as the frequency below which 95% of spectral power resides. It can be found by taking the cumulative sum of spectral power for all the frequency bins up until the frequency where 95% of spectral power is surpassed.

2.4.3 Artifacts

Potentials measured on the scalp of a patient that do not originate from the brain are labeled as artifacts. The electrocortical activity measured at the scalp is in the order of 10-100 μV . Compare this with the potential from a heartbeat of 1 mV and from the power grid of 1 V and it is easily understood that the EEG is sensitive to artifacts. Since the potentials of artifacts are generally much higher than that of true electrocortical activity, it is important to localize and omit them before signal analysis. Artifacts can be classified as either physiologic or extraphysiologic. A number of possible artifacts are listed in Table 2.2 [51-53]. In this study frequency thresholds are applied to identify and discard artifacts. A detailed description on the approach used in this study is given in section 3.3.3.

Table 2.2: Possible physiologic and extraphysiologic artifacts in EEG recordings.

Physiologic artifacts	Extraphysiologic artifacts
EMG (electromyogram) Induced by muscle movement, e.g. clenching of the jaws. Generally in the 20-100 Hz range.	Electrode movement Low frequency artifact in the 1-8 Hz range, due to e.g. improper placement.
ECG (electrocardiogram) Rhythmic spike activity originating from the heart. Pulse artifacts due to electrode placement on blood vessels are also directly related to the ECG.	Electrode popping Single or multiple sharp waves due to abrupt electrode impedance change.
Eye-movement Eye acting as a dipole. Eye movements and eye blinks produce artifacts in the 4-13 Hz range at the frontal electrodes.	Power grid Artifact at 50 Hz frequency from power lines due to poor electrode grounding.
Glossokinetic Tongue acting as a dipole, e.g. sucking and chewing. Generally in the 1-4 Hz range. Common in neonates.	Movement in environment Movement inside the room, respirator movement and even intravenous infusion can result in artifacts.
Respiration Slow and rhythmic, synchronous with body movement. Or sharp during inhalation or exhalation.	
Skin Impedance change of skin due to biological processes, e.g. sweating. Generally very slow baseline sways in the 0.25-0.5 Hz range.	

3 Spectral effects of antiepileptic drugs in perinatal stroke

3.1 Introduction

Neonates with encephalopathy often present with seizures due to the underlying brain injury (occurring in 3 of 1000 live births [13]). These seizures are believed to actively contribute to further damage of the brain [14, 15], and treatment strategies are focused on seizure suppression by administration of AEDs. Administration of AEDs has an effect on neuronal signal transmission and thus alters the appearance of (a)EEG significantly. This may hamper clinical interpretation of aEEG and EEG, which are essential tools in diagnostic and prognostic assessment, and a correct understanding of the EEG effects after AED administration is therefore critical. Previous studies of AED effects in neonates have only focused on aEEG [38-41], whereas more detailed spectral studies have only been performed in adults [54-60]. This is the first study of the spectral effects of AEDs performed in neonates. The aim of the study presented here is to quantify the effects of common AEDs, midazolam and lidocaine, on EEG spectral power for full-term infants with seizures after PAIS.

3.2 Theory

3.2.1 Types of medication

The treatment strategy to control and suppress seizure activity is based on the administration of different types of AEDs in successive order until seizure activity is terminated (see section 3.2.2 for a description of the medication protocol). A description of the AEDs that are used in this medication protocol is given in this section.

Phenobarbital belongs to the class of barbiturates (derived from barbituric acid) and is the most commonly used AED to suppress seizures. Barbiturates increase the effectiveness of GABA, which is the primary inhibitory neurotransmitter in the CNS. They increase the permeability of neuronal Cl^- ions. In mature brains the extracellular concentration of Cl^- is lower than the intracellular concentration and this leads to an influx of Cl^- into the cell causing hyperpolarization and decreased excitability [14]. In neonates however, this Cl^- gradient is reversed and GABA receptor activation by midazolam increases Cl^- efflux and can cause depolarization and increase excitability [61]. Spectral studies of the effects of phenobarbital show an increase of high frequency power [62, 63]. Phenobarbital is a long-acting AED and has a median half-life of 115 hours [64, 65].

Midazolam is a benzodiazepine and, like barbiturates, this group of drugs enhances the effect of GABA. Neuron excitability is decreased and this results in seizure suppression. Conflicting effects of EEG spectral power changes after midazolam administration in adults have been reported [54-60]. See Appendix D for an overview of results from several literature studies on the spectral effects of midazolam. Suppression of 30-120 minutes of aEEG background pattern is reported in literature after midazolam administration [39, 41]. Mixed success rates of seizure control are reported in literature [39, 40, 66]. Midazolam is a short-acting AED and has a half-life of 2 to 5 hours [59, 67].

Another anticonvulsive benzodiazepine is clonazepam, again decreasing neuronal activity by enhancing the effect of GABA. It has been reported that clonazepam does not alter aEEG background [39], but the patient group is small in this study. In another study it has been found that clonazepam did prove effective in suppressing seizure activity [66], again for a small patient group. Unlike midazolam, it is a long-acting AED with a half-life of 18 to 50 hours.

Lidocaine is a local anesthetic and class I antiarrhythmic agent that blocks the fast voltage gated sodium channels in the neuronal cell membrane, decreasing conduction of sodium ions and thus signal propagation (for a description of signal propagation see section 2.1.3). With sufficient blockage, the membrane of the postsynaptic neuron will not depolarize and no action potential will be transmitted [68]. Spectral studies on EEG effects by lidocaine are limited and report absolute power increase of δ and β bands [69], or an increase of relative δ powers and a decrease of relative powers in higher frequency bands [70]. Lidocaine is a short-acting AED with a half-life of approximately 100 minutes [71].

Pyridoxine is part of the vitamin B₆ group, and is an AED for patients with pyridoxine-dependent epilepsy. This is an extremely rare form of epilepsy (occurring in 1 of 10⁵ people) that requires lifelong supplements of vitamin B₆ [72]. It is standard protocol to test neonates for this type of epilepsy when seizure control is impossible with other AEDs.

3.2.2 Medication protocol

Different AEDs are administered following a strict order and dosage scheme in neonates presenting with seizures. Increase of dosage or a switch to another AED is made when seizures are recurrent. Dosage levels are dependent on weight and administration can be either intravenously or through continuous infusion.

An overview of the drug protocol, as applied in all patients in this study, is given in Figure 3.1 [73]. First-line AED is intravenous phenobarbital given as a loading dose of 20 mg/kg, and is increased if needed with an additional dose of 10 mg/kg to a maximum cumulative loading dose of 30 mg/kg. Additional AED treatment relies on clinical and/or EEG indications. Midazolam is administered as second-line agent at 0.05 mg/kg as a loading dose, given over a ten minute period, followed by a continuous infusion of 0.15-0.2 mg/kg/hr as a maintenance dose. If seizure activity persists, or when recurrence of seizures is noted, lidocaine is added to midazolam with a loading dose of 2 mg/kg in 10 minutes, followed by a step-down maintenance dose of 6-4-2 mg/kg for 6-12-12 hours respectively. A pyridoxine test is performed when seizure activity still persists, consisting of intravenous single or multiple boluses of 50 mg/kg of pyridoxine. When pyridoxine-dependent epilepsy is ruled out, clonazepam can be added to the treatment regime with single or multiple boluses of 0.1 mg/kg.

Similar protocol strategies are applied in other treatment centers around the world, though sometimes with slightly varying dosage levels [40, 41, 74, 75].



Figure 3.1: The drug protocol as applied in patients in this study presenting with seizures.

3.3 Methods

3.3.1 Patient group

Fifty-one full-term neonates (gestational age ≥ 37 weeks, defined as number of weeks since the mother's last menstrual period) diagnosed with PAIS during the neonatal period have been admitted to the Wilhelmina Children's Hospital (Utrecht, the Netherlands), between 2003 and 2010. A sub-selection of 25 neonates with multi-channel aEEG recordings is included in this retrospective study. Within these aEEG recordings, annotations describing AED administration are available for 12 neonates. Of the 12 subjects included in this study, 6 have received midazolam followed by lidocaine at a later time-point (see medication protocol in section 3.2.2), 2 have received only midazolam and 4 only lidocaine during neurophysiologic monitoring (for these infants midazolam is administered pre-recording). Details of the study population are presented in Table 3.1.

Table 3.1: Details of the study population receiving midazolam and/or lidocaine treatment. Values are expressed as median (range).

	Midazolam	Lidocaine
Population (#)	8	10
Male/Female (#)	2/6	5/5
Gestational Age (wks ^{days})	41 ³ (37 ⁶ -41 ⁵)	41 ⁰ (39 ⁶ -41 ⁵)
Birth Weight (g)	3380 (2150-3700)	3208 (2430-3700)
Apgar Score at 5 min	9 (5-10)	7 (4-10)
Umbilical Cord pH	7.1 (7.0-7.2)	7.1 (7.0-7.2)
Lactate (mmol/l)	3.2 (2.0-8.0)	3.5 (1.6-6.4)
Start of Medication (hrs after birth)	32 (5-133)	37 (7-135)

Of the 12 included infants, 11 have unilateral PAIS and 1 has bilateral PAIS (with one side dominating in ischemic damage over the other). In 7 neonates the stroke is a MCA and in 5 neonates a PCA infarction. No ACA artery infarctions are present in the patient group.

3.3.2 Data acquisition

Multi-channel aEEG recordings are obtained with Brainz BRM2 and BRM3 digital brain monitors (Natus® Medical Incorporated, CA, USA). These devices record the EEG and calculate the aEEG from these data for three channels (F3-P3, F4-P4, and P3-P4, see Figure 2.11). Data are high-pass filtered (BRM2: -3 dB at 0.5 Hz, BRM3: -3 dB at 0.3 Hz), and a 30 Hz anti-aliasing filter (low-pass) is applied before sampling the EEG at 64 Hz and calculation of the aEEG.

In general, data acquisition is started in the first or second day of life (10 neonates). For two neonates, monitoring has started on the third and sixth day of life, respectively. The median recording duration is 107 hours (range: 83-176 hours).

3.3.3 Data analysis

Data segments are selected for analysis when annotations, describing the exact time of the administration of the loading dose of either midazolam or lidocaine, are present. These segments are four hours long, starting one hour before administration until three hours after. The initial hour before AED administration allows for adequate determination of (a)EEG baseline values, and drug related changes in the EEG recording are anticipated to occur within the following 3 hours, as has been illustrated by several aEEG studies on both midazolam and lidocaine [38, 39].

Baseline aEEG background patterns and seizure activity of the hour preceding AED administration are visually classified by a trained neonatologist according to the classification described in section 2.2.3 and Appendix A. These are compared to the background patterns and presence of seizures in the three hours following AED administration to detect drug-related changes. Comparisons between both hemispheres are made by analysis of the fronto-parietal bipolar deductions (F3-P3 and F4-P4).

Spectral analysis of the EEG is performed using Matlab® (The MathWorks, MA, USA). Before performing spectral analysis the frequency response of all data are to be corrected to match the response of the BRM3 monitor. This is necessary since measurements on different monitors, and even on different firmware versions of the same monitor, can show significant differences in frequency response. Towards this end, the frequency response of a monitor is measured by an oscilloscope after each firmware update, by using a function generator to apply signals of known amplitude and frequency. The result of this procedure is shown in Figure 3.2 (a) for two firmware versions of BRM2 and one of BRM3. Significant differences in frequency response can be seen for frequencies below 3 Hz and above 15 Hz. Correction factors are calculated from these data to match both BRM2 responses to the BRM3 monitor. The result is shown in Figure 3.2 (b) for the 0-2 Hz frequency range. Similar correction factors are necessary from 15-30 Hz but are not shown here, since absolute spectral power content in this range is typically around 1-2 %. The large correction factors at low frequencies amplify noise and therefore frequencies below 1 Hz are omitted from analysis in this study (a definition of neonatal frequency bands is given in section 2.4.2).

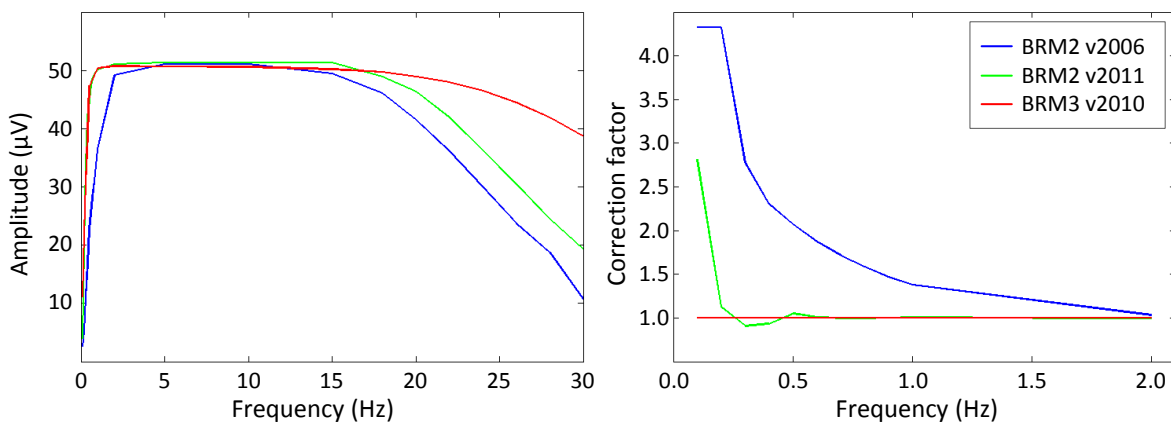


Figure 3.2: Frequency response of aEEG monitors to 50 μ V waves of varying frequency (a) and the correction factors necessary for both BRM2 versions to match the response of the BRM3 monitor (b). Note that the correction factors in the high frequency range are also significant, but are not displayed in this graph for practical reasons (also, only about ~3% absolute spectral power resides in the high frequency range).

An overview of the different processing steps of the EEG spectral analysis is given in Figure 3.3. The four hour data segments are subdivided into blocks of 1 hour for spectral analysis. An hour of data is read and voltages are corrected for the analog to digital convertor (A/D, division by 30.9976). The first step is to read out all events that have been annotated in the data stream, e.g. feeding or care. If events are present, 10 minutes of data surrounding the event are omitted from the analysis. Electromyogram (EMG) and muscle artifacts reside in the 20-100 Hz frequency range (discussed in section 2.4.3). Filtering with a low-pass filter at 20 Hz is not possible since high frequency electrocortical activity can reach values up to 30 Hz in neonates. Therefore another approach is taken; EMG artifacts can be detected by setting a power threshold value for the absolute power above 25 Hz [76]. The data stream is duplicated and high-pass filtered at 23 Hz to attenuate the signal below this frequency (8th order Butterworth filter, zero-phase shift). The data is subdivided into 0.25-second segments and the Fourier and power spectra are calculated (Hamming window, no overlapping segments [77]). An empirical power threshold of 100 μV^2 is used to identify EMG artifacts which are subsequently omitted from the analysis.

The original 1 hour block of data is then high-pass filtered at 0.5 Hz and low-pass filtered at 30 Hz (8th order Butterworth filter, zero-phase shift). The data is subdivided into 4-second segments, resulting in a 0.25 Hz frequency resolution which is adequate for this study. An overlap of two seconds between segments is taken to prevent loss of data at the edges of the segments due to windowing (explained in section 2.3.2). To prevent spectral leakage, the resulting 1800 segments are all multiplied by a Hamming window. The FFT is now taken and the power spectrum is calculated. The power spectrum is corrected for the power of the 4 second Hamming window itself (division by 0.39585, see Harris 1978 [48]). Additionally, the power spectrum is corrected to match the BRM3 monitor if necessary. The frequency bins below the δ band (below 1 Hz) are omitted due to large correction factors. Finally noise, e.g. due to bad electrodes, is detected by a power threshold of 0.1 μV^2 and movement artifacts are detected by a threshold of $10^4 \mu\text{V}^2$, and both are excluded from further analysis [77].

The artifact detection results in a median exclusion of 16.7% of the 4-second segments per hour of data for all patients (with interquartile range (IQR): 0.1%-18.5%, indicating that 25% of the 1-hour segments is artifact- and event-free). A single power spectrum for each hour of data is now calculated for each patient by taking the median of all power spectra from the remaining artifact-free 4-second segments. The total power is defined as the sum of powers across all frequency bins. Band powers, (normalized) absolute or relative, as well as SEF follow definitions as given in section 2.4.2. Like the aEEG analysis, the EEG spectral analysis is performed for both hemispheres by use of fronto-parietal bipolar deductions (F3-P3 and F4-P4). Median and IQR values are calculated per hour over all patients and displayed graphically to indicate general trends across the patient group.

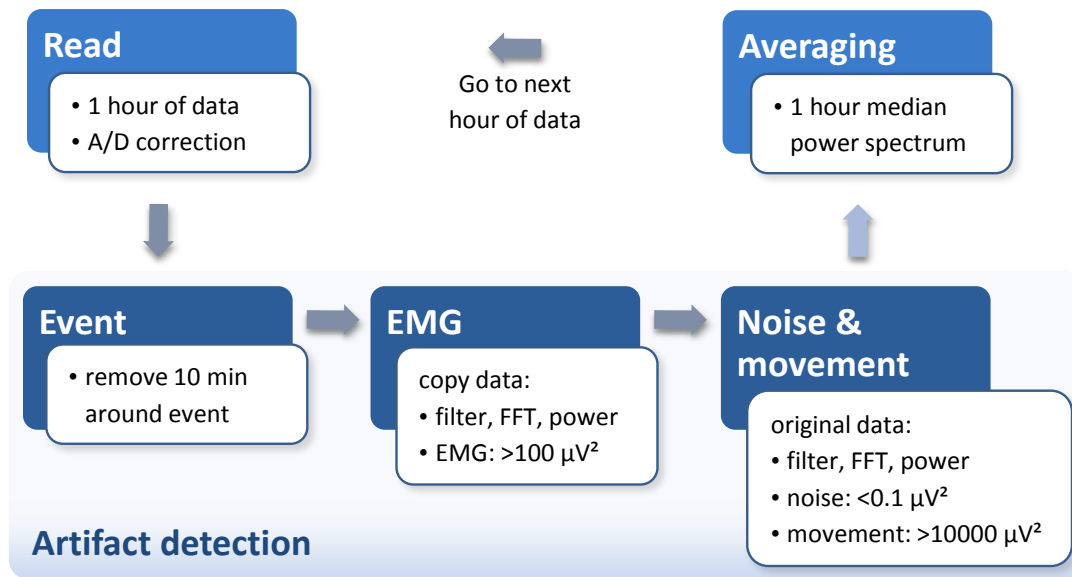


Figure 3.3: Different processing steps as applied when performing spectral analysis of the EEG signal. Segments starting one hour before until three hours after AED administration are selected for analysis. The data is analyzed and averaged per hour, after artifacts are detected and omitted. The power spectra are corrected for the use of a Hamming window and also to match the frequency response of the BRM3 monitor.

3.3.4 Statistics

An average power spectrum for each hour of data is obtained by calculating the median values over all 4-second segments and for each frequency bin. A Lilliefors test is used to test the null hypothesis that the data comes from a normal distribution [78]. The test is an adaptation from the Kolmogorov-Smirnov test, but does not require the mean and variance of the dataset to be known. The Lilliefors test shows that the data in this study is not normally distributed (with a p-value below 0.001). Therefore, the median value is favored over a simple mean when calculating the average spectrum. The median value is less sensitive for outliers, e.g. due to artifacts, as compared to the mean. Variability is indicated with IQR instead of using standard deviations, again since the data is not normally distributed.

Statistical significance of power spectra after administration of AEDs with respect to baseline power spectra is determined by a Wilcoxon signed-rank test (sometimes referred to as the Wilcoxon T-test). This non-parametric test is preferred over the paired Student's T-test since our data is not normally distributed. It is designed to assess whether the population mean ranks differ between two related samples [79]. The 1 hour median power spectra in our study are related since they are calculated from repeated measurements. A p-value below 0.05 is considered statistically significant.

3.4 Results

3.4.1 aEEG

Midazolam: A total of eight patients have received midazolam as a first-line AED. See Figure 3.4 for an overview of background and seizure activity changes for both hemispheres following AED administration. An immediate and moderate background suppression following AED administration is observed in all patients. The suppression is visible within minutes and lasted between 30 and 60 minutes. In four patients this suppression is so large that the background pattern in the ipsilateral (stroke affected) hemisphere degrades from CNV to DNV in three patients and from DNV to BS in one patient. A similar effect is seen for the contralateral (unaffected) hemisphere, in four patients CNV degrades to DNV. Generally, the background patterns are better contralateral than ipsilateral (larger number of patients with CNV in healthy hemisphere than in affected hemisphere).

Seizure activity is most prominent in the ipsilateral hemisphere with six patients having repetitive seizures and two showing *status epilepticus*. After AED administration repetitive seizures disappeared in two patients, but changed into *status epilepticus* in another two patients. The initial *status epilepticus* in two patients prior to AED administration remained unaffected. The contralateral aEEG shows no *status epilepticus* and two infants with repetitive seizures, which are reduced in one. Typical aEEG responses in the absence and presence of seizures are shown in Figure 3.5.

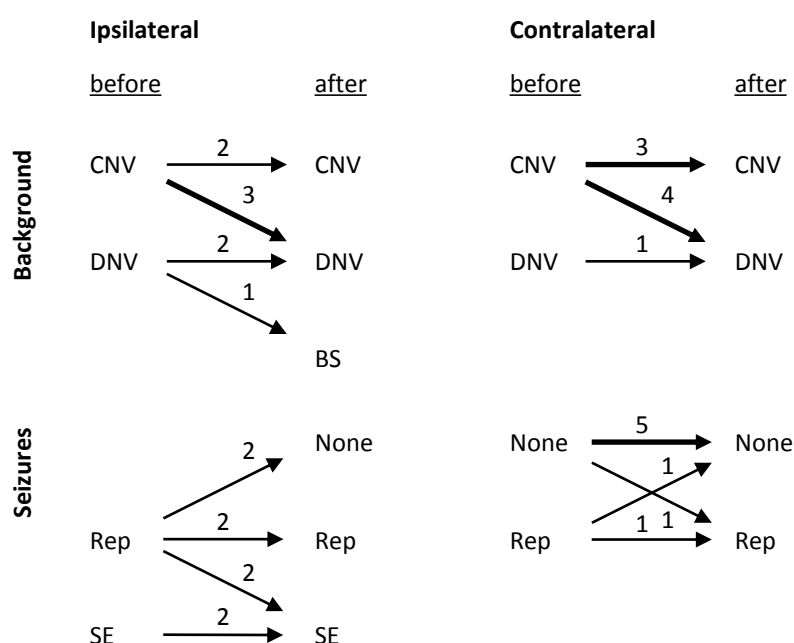


Figure 3.4: Illustration of changes in background patterns and seizure activity for both hemispheres among the patients receiving midazolam. Midazolam suppresses background activity and does not show a clear effect on seizure activity. Note that thicker arrows represent larger numbers. Seizure abbreviations are: Rep=repetitive seizures, SE=*status epilepticus*. See Appendix A for the classifications of background patterns and seizure activity.

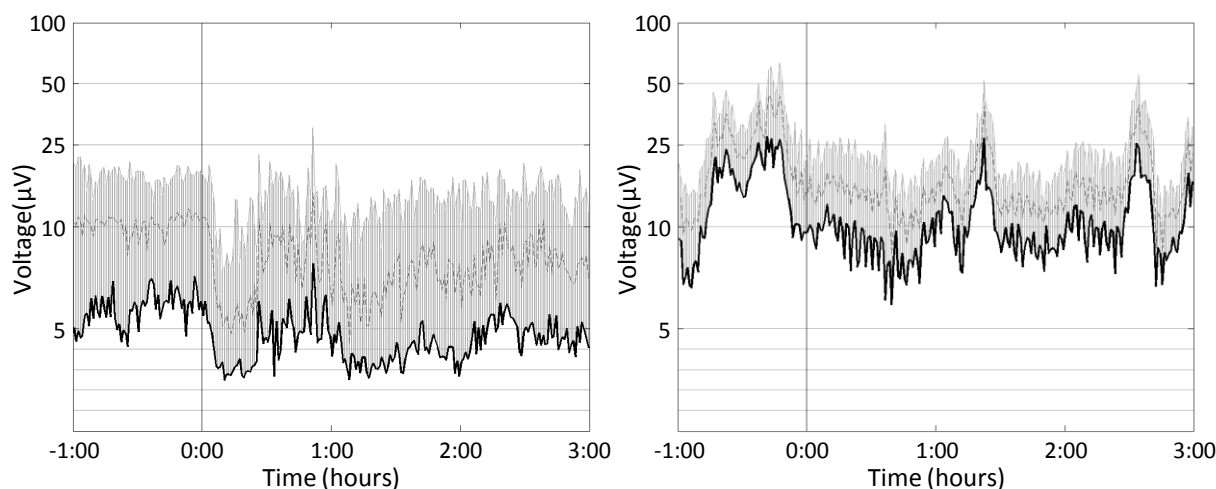


Figure 3.5: Typical aEEG response following midazolam administration. Midazolam introduces an immediate suppression of aEEG background (a). Seizure activity, appearing as sharp and sudden spikes of increased voltage, remains present in most patients following midazolam administration (b). The time of AED administration is indicated in the graphs with the vertical line located at 0:00.

Lidocaine: Ten patients have received lidocaine as second-line AED following midazolam. See Figure 3.6 for an overview of background and seizure activity changes for both hemispheres following AED administration. No significant suppression of aEEG background patterns is observed after receiving lidocaine. Eight patients retained either CNV or DNV in both hemispheres. Ipsilaterally, one CNV degrades to DNV and one DNV degrades to BS. Contralaterally, one DNV changes to CLV. The quality of the aEEG background is similar between the hemispheres (approximately equal numbers of patients with CNV in both hemispheres).

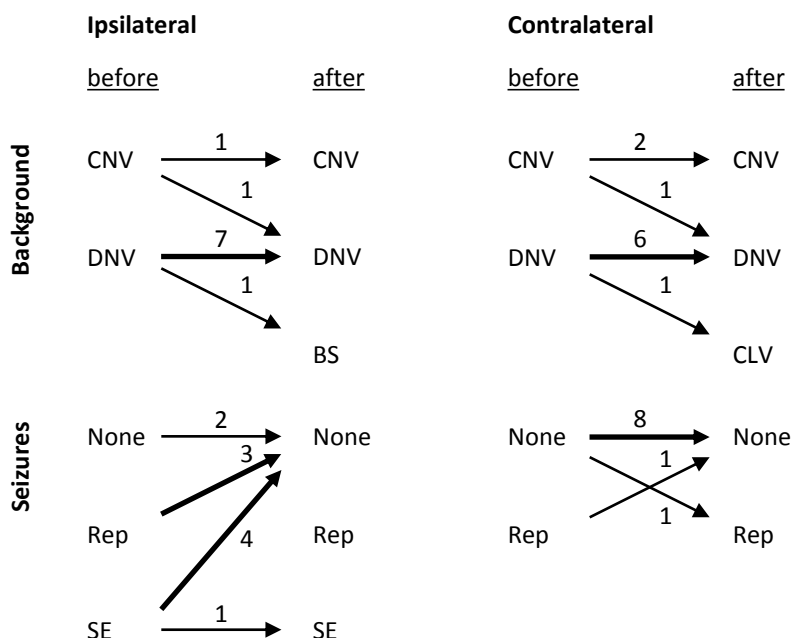


Figure 3.6: Illustration of changes in background patterns and seizure activity for both hemispheres among the patients receiving lidocaine. Lidocaine does not clearly affect the background pattern, but does suppress seizure activity significantly. Note that thicker arrows represent larger numbers. Seizure abbreviations are: Rep=repetitive seizures, SE=*status epilepticus*. See Appendix A for the classifications of background patterns and seizure activity.

Again, seizure activity is most prominent in the ipsilateral hemisphere. Five patients have *status epilepticus* and three patients have repetitive seizures in this hemisphere prior to AED administration. Lidocaine suppresses seizure activity in four out of five *status epilepticus* patients and in all three patients with repetitive seizures. No *status epilepticus* and only one case of repetitive seizures are present contralaterally. Typical aEEG responses in the absence and presence of seizures are shown in Figure 3.7.

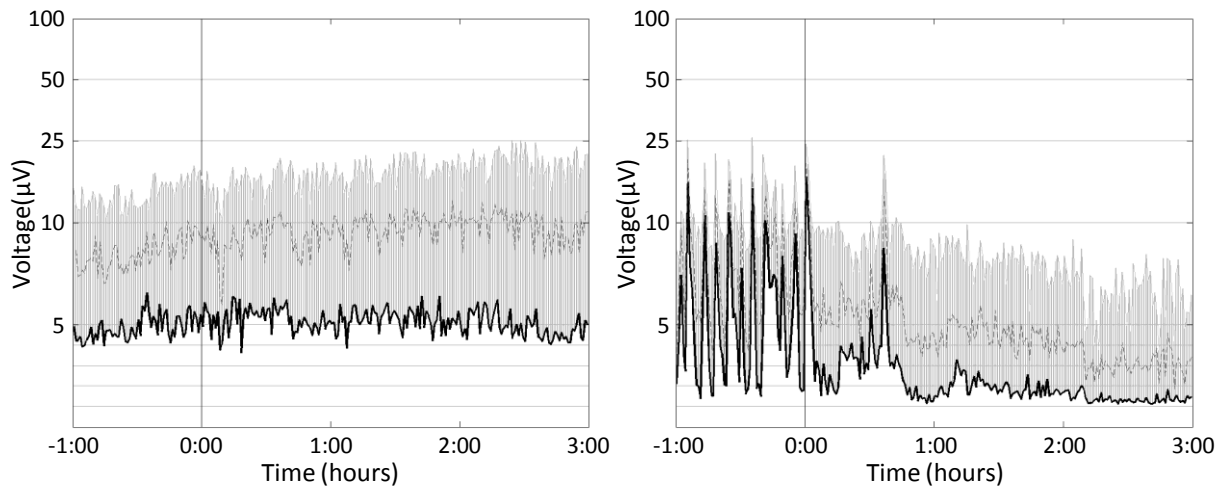


Figure 3.7: Typical aEEG response following lidocaine administration. Lidocaine does not alter aEEG background (a). Seizure activity, in this example *status epilepticus*, is suppressed in 7 of 8 patients following lidocaine administration (b). The time of AED administration is indicated in the graphs with the vertical line located at 0:00.

3.4.2 EEG spectral analysis

Midazolam: Absolute spectral powers of EEG for the 8 patients receiving midazolam are displayed in Figure 3.8 for ipsilateral (a) and contralateral (b) hemispheres. Significant suppression with respect to the first hour is found across all frequency bands. The normalized absolute spectral powers with pre-medication baseline values (c) and (d) show similar behavior. The largest suppression occurs in the first hour after AED administration, and the following second and third hours show stabilized absolute and normalized powers. Two exceptions are the normalized absolute δ and θ powers in the contralateral hemisphere that show a gradual but continuous decrease for all hours following administration. Corresponding baseline and maximum effect values are given Table B.1 in Appendix B. There are no significant differences in midazolam-related changes in absolute power value between ipsilateral and contralateral hemispheres (see Table B.2 in Appendix B for interhemispheric p-values).

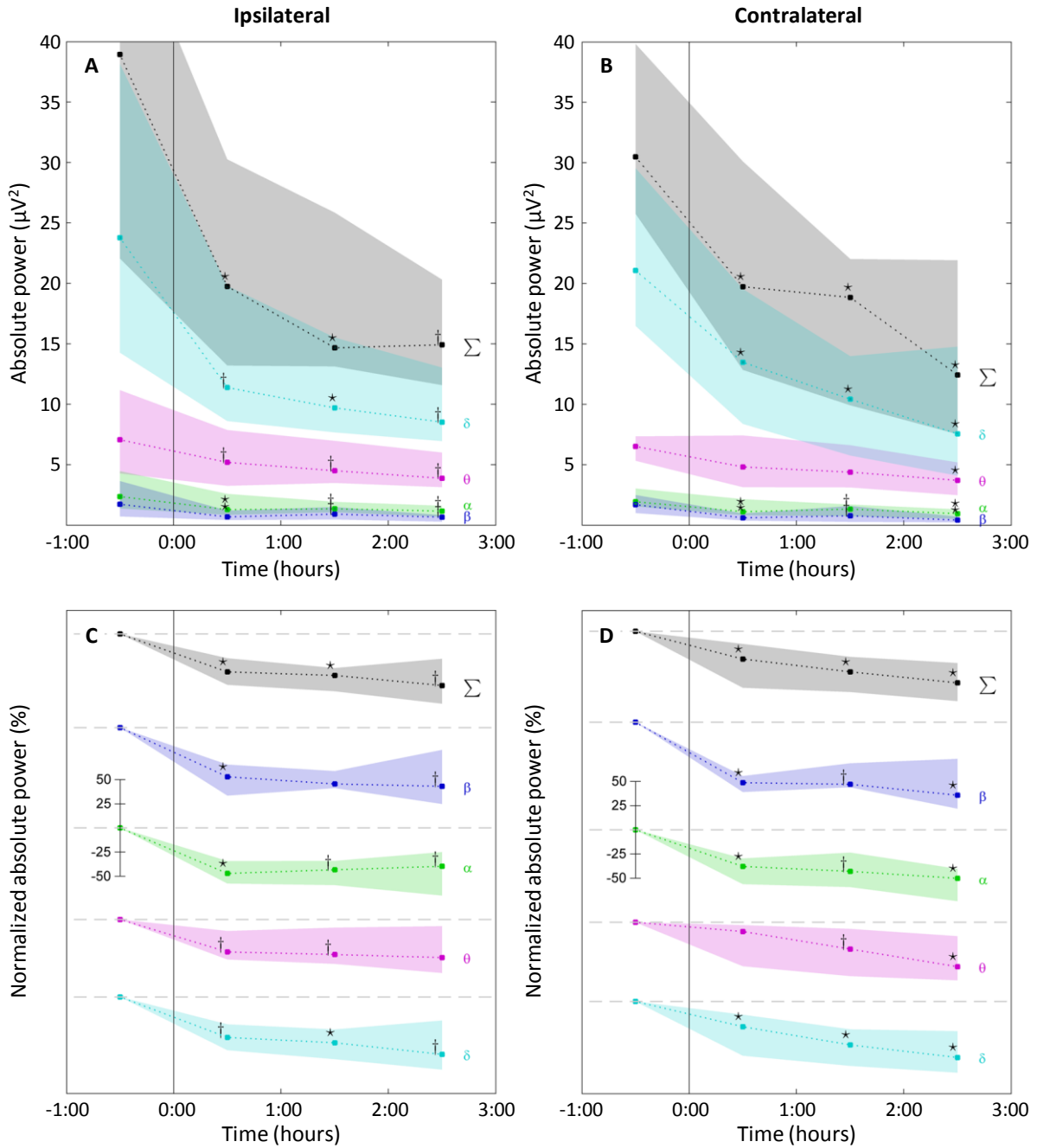


Figure 3.8: Absolute spectral powers following midazolam administration. Median values ($n=8$) of total power (Σ) and frequency band powers (δ , θ , α and β) are shown with IQR for ipsilateral (a) and contralateral hemisphere (b), and normalized with pre-medication baseline values for each patient individually in (c) and (d). Statistical significant changes with baseline values are indicated with: * $p<0.01$ and † $p<0.05$.

Relative spectral powers following midazolam are displayed in Figure 3.9 (a) and (b) and normalized relative spectral powers in (c) and (d). Most spectral power resides in the δ frequency band, followed by the θ band. The relative δ power shows a small decrease and the θ band a significant increase in the second and third hour following midazolam administration. Corresponding baseline and maximum effect values are given in Appendix B. The spectral edge frequency (SEF) in the contralateral hemisphere shows a significant 3.4 Hz decrease during the first hour after the administration of midazolam (see Table B.1 in Appendix B). Simultaneously, the IQR decreases from 6 Hz to 1 Hz, indicating a convergence

of the SEF to approximately 10 Hz for all neonates after midazolam administration. From the second hour after administration onwards, the IQR increases again. There is no significant change of the SEF in the ipsilateral hemisphere. There are no significant differences in the effect of midazolam on relative power values between ipsilateral and contralateral hemispheres (see Table B.2 in Appendix B for interhemispheric p-values).

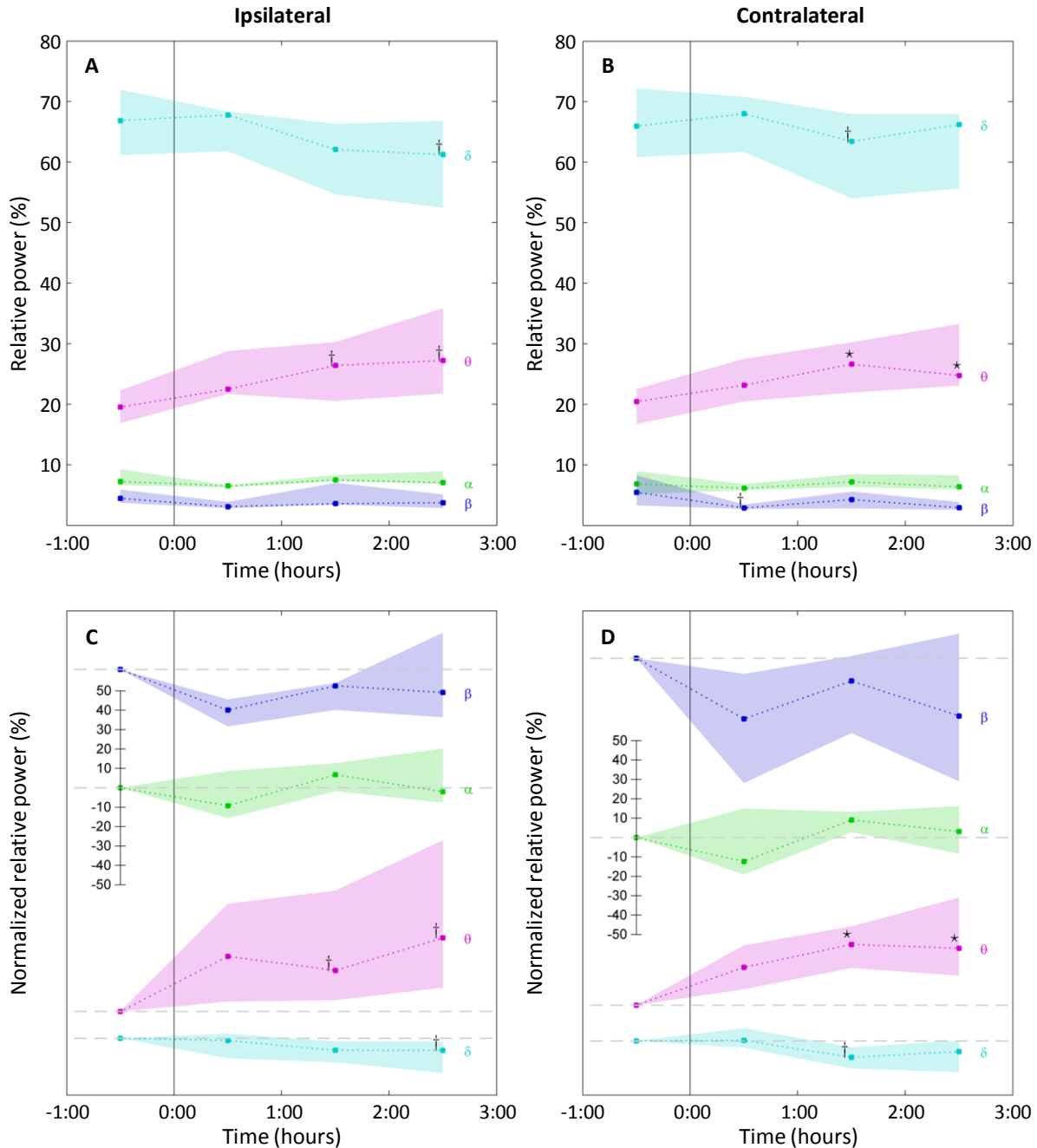


Figure 3.9: Relative spectral powers following midazolam administration in 8 patients. Statistical significant changes with baseline values are indicated with: * $p < 0.01$ and † $p < 0.05$.

Lidocaine: Absolute spectral powers following lidocaine administration for 10 patients are displayed in Figure 3.10 (a) and (b) and normalized absolute spectral powers in (c) and (d). No significant changes in total absolute power are observed following lidocaine. The normalized absolute frequency band powers show no significant change, except for a

significant ipsilateral decrease in δ power after administration. Corresponding baseline and maximum effect values are given in Table C.1 in Appendix C. Absolute power values are not significantly different between ipsilateral and contralateral hemispheres, with exception of normalized total power and δ power in the third hour after administration of lidocaine ($p < 0.05$ and $p < 0.01$ respectively, see Table C.2 in Appendix C for interhemispheric p-values).

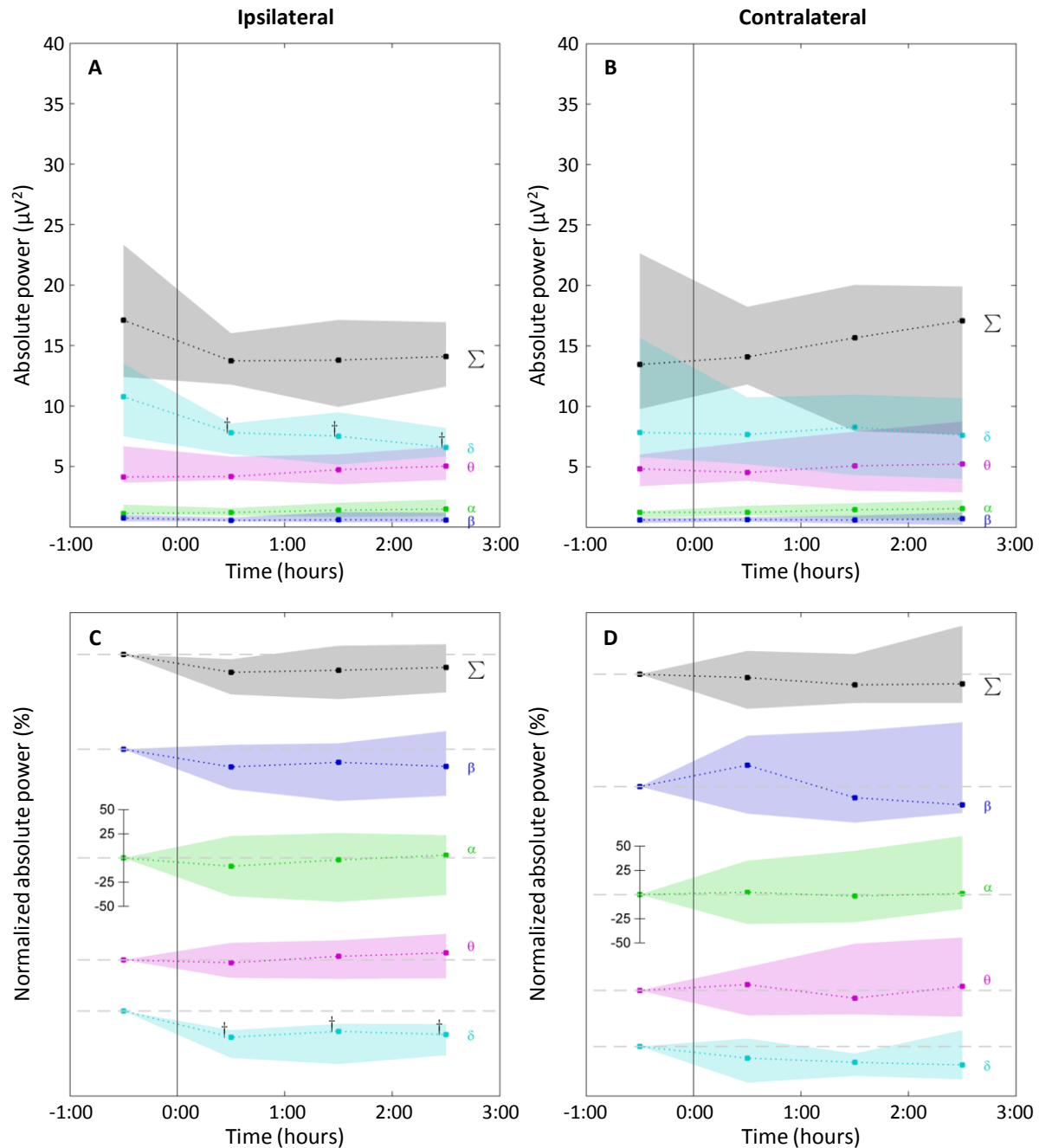


Figure 3.10: Absolute spectral powers following lidocaine administration in 10 patients. Statistical significant changes with baseline values are indicated with: * $p < 0.01$ and † $p < 0.05$.

Relative spectral powers following lidocaine are displayed in Figure 3.11 (a) and (b) and normalized relative spectral powers in (c) and (d). The normalized relative δ power shows a significant decrease from the first hour after lidocaine administration in both hemispheres, while an increase of normalized relative θ and α power is observed. Relative β band power

and SEF do not show consistent change after lidocaine administration. Corresponding baseline and maximum effect values for relative band powers and SEF are shown in Table C.1 in Appendix C. Lidocaine-induced changes in normalized relative spectral powers are more pronounced in the ipsilateral hemisphere. Normalized relative δ power only differs significantly ($p < 0.05$) between the ipsilateral and contralateral hemispheres in the second hour after administration, while normalized relative θ power differs significantly for first ($p < 0.01$), second and third hour (both $p < 0.05$) after administration of lidocaine. See Table C.2 in Appendix C for interhemispheric p-values.

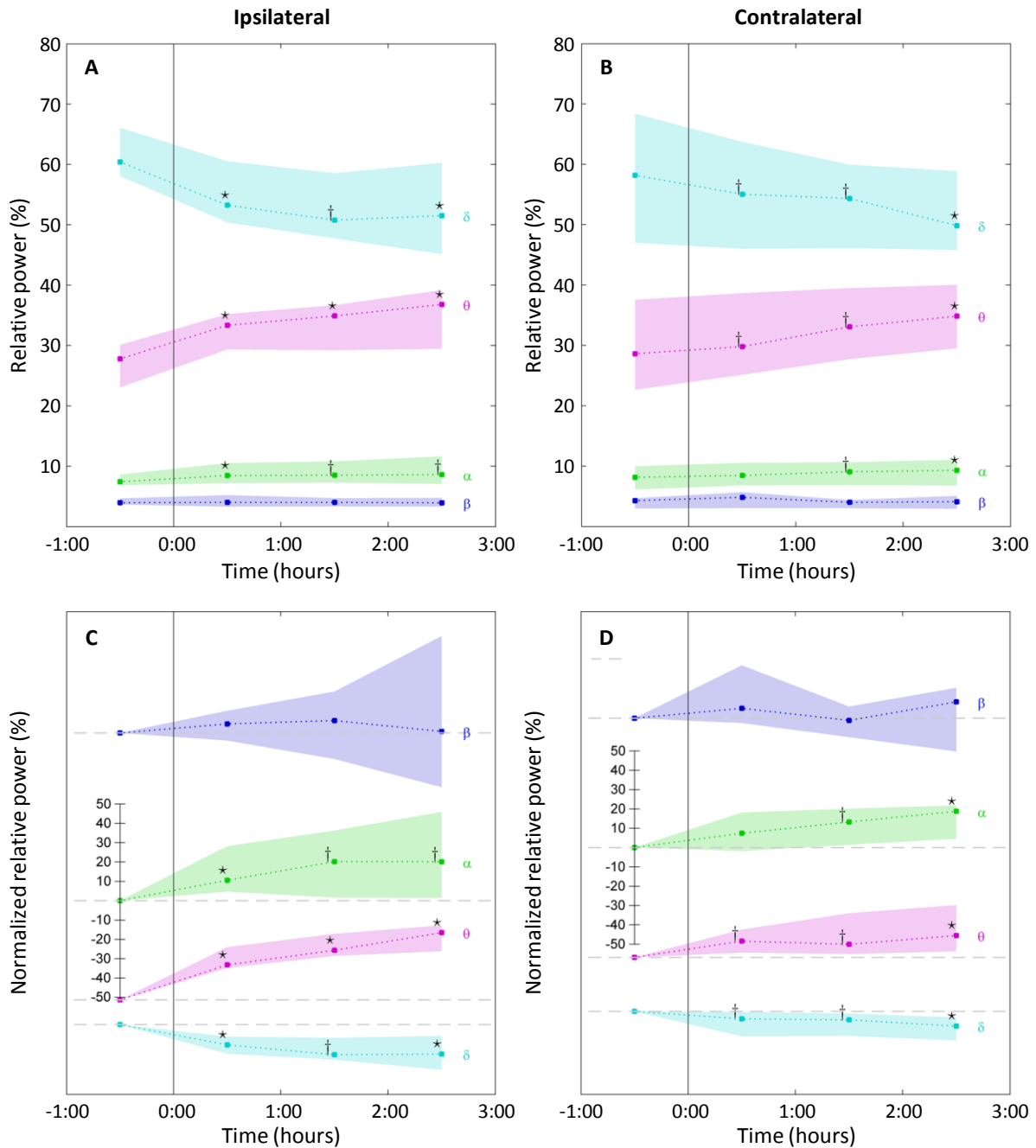


Figure 3.11: Relative spectral powers following lidocaine administration in 10 patients. Statistical significant changes with baseline values are indicated with: * $p < 0.01$ and † $p < 0.05$.

3.5 Discussion

3.5.1 aEEG

Midazolam: Spectral analysis of the neonatal EEG after administration of midazolam and lidocaine in full-term neonates with PAIS has been performed. Previous studies of AED effects in neonates have mainly focused on background patterns and seizure activity through monitoring the aEEG [38-41, 80]. In this study, a background suppression of 30-60 minutes following midazolam administration has been observed. This is in accordance with studies reporting a background suppression of 30-120 minutes after a midazolam loading dose [39, 41]. In four out of eight patients receiving midazolam in this study, the suppression of aEEG background is large enough to induce a change of background pattern (3 CNV→DENV, 1 DENV→BS). Contrarily, Leuven *et al.* have observed background suppression of CNV or DENV in only 1 patient out of 15, but in patients with bad background patterns, BS and CLV, almost all patterns are suppressed to CLV or FT respectively [39]. Suppression from DENV to BS, as is observed once in this study, has been reported by ter Horst *et al.* in 2004 [40]. Midazolam does not adequately reduce seizure activity in the patients of this study and mixed success rates have been reported in literature [39, 40, 66].

Lidocaine: Lidocaine administration suppresses the aEEG background pattern in only 2 out of 10 patients. Other studies also report a very minor suppression of the background pattern [38, 41]. It has to be noted that the aEEG background is harder to assess reliably in the four neonates with *status epilepticus* at the time of AED administration. Efficient seizure suppression is observed for lidocaine, reducing repetitive seizures or *status epilepticus* in 7 out of 8 neonates, which is in agreement with other studies [38, 70, 81].

3.5.2 EEG spectral analysis

Midazolam: In literature, spectral analysis of the effect of midazolam on the EEG is limited to adult studies [54-60]. See Appendix D for an overview of the reported EEG changes after AED administration. The spectral analysis of neonatal EEG in the current study shows a suppression of total and absolute band powers following midazolam administration. This is in agreement with the aEEG background pattern suppression as observed in this study and others [39, 41]. Change in total spectral power is only evaluated in one other study and an increase has been reported after midazolam administration [54]. Absolute frequency band powers in the neonatal EEG are all found to decrease significantly. Durka *et al.* also see a decrease in absolute δ and θ band power, but also an increase in β power is noted. Feshchenko *et al.* noted an increase in absolute α and β powers in health volunteers after midazolam intake. In the current study a significant decrease in relative δ power is observed accompanied by a significant increase of relative θ power. Two studies also report this decrease of relative δ power, but this is accompanied by increases of relative α and β power [55, 56]. Since all the spectral studies in literature are performed on adults, these discrepancies may result from the relative immaturity of the neonatal brain. The maturing brain signals increase in complexity, due to regional specialization and the formation of neuronal networks [82]. The lack of a response in α and β bands in neonates following midazolam might also be attributed to the maturational stage of the neonatal brain. With brain maturation comes an increase of WM myelination increasing neuronal signal conducting [83, 84], which may increase high frequency activity.

Midazolam is a benzodiazepine and this group of drugs enhances the effect of the inhibitory neurotransmitter GABA, increasing the permeability of neuronal chloride ions (see section

3.2.1). In mature brains the extracellular concentration of Cl^- is lower than the intracellular concentration and this leads to an influx of Cl^- into the cell causing hyperpolarization and decreased excitability [14]. In neonates however, this Cl^- gradient is reversed and GABA receptor activation by midazolam increases Cl^- efflux and can cause depolarization and increase excitability [61]. This might explain the large increase in relative δ power observed in the neonatal EEG in this study.

Lidocaine: Reports on spectral analysis of the effect of lidocaine on the EEG are very limited in numbers and again only investigated in adults [69, 70]. See Appendix D for an overview of spectral changes after lidocaine administration as has been reported by other studies. Spectral changes of absolute total power after lidocaine administration show no significant trend. Normalized total power shows an increased IQR indicating a possible increase or decrease on an individual patient basis, but no net effect for the study group. This is in agreement with observations of aEEG background patterns in this study, which remain constant after lidocaine administration. Significant decrease of relative δ power and significant increases of θ and α powers are observed in the neonatal EEG following lidocaine. This is in contrast with Madhavan *et al.* [70], that have reported an increase of relative δ power and decrease of θ and α powers. As with midazolam, these discrepancies may result from the immaturity of the neonatal brain. Normalization of neonatal EEG with baseline values in this study may be inaccurate due to the presence of *status epilepticus* in several patients prior to AED administration. However, the significant rise in relative δ power is accompanied by a small IQR indicating a general trend among the entire study group.

Lidocaine is a local anesthetic and class I antiarrhythmic agent that blocks the fast voltage gated sodium channels in the neuronal cell membrane, decreasing conduction of sodium ions and thus signal propagation (for a description of signal propagation see section 2.1.3). With sufficient blockage, the membrane of the postsynaptic neuron will not depolarize and no action potential will be transmitted [68]. In a rat study no maturation-related differences have been observed in the effects of lidocaine sodium channel blockage [85]. Other studies indicate that lidocaine plasma levels are dependent on the maturity of the metabolism in the neonate, but that seizure reduction effectiveness is independent of plasma concentrations [74].

3.5.3 Limitations

This study of spectral properties of neonatal EEG after AED administration contains several limitations. First, the size of the study group is relatively small. This may result in increased variability of the effects after AED administration and might explain the large IQR values that are observed. However, statistical tests do show significant changes of spectral parameters following AEDs. Other studies investigating the effects of AEDs in neonates generally have similar or slightly larger study groups, but mainly focus on changes in aEEG background patterns and seizure activity [38, 39, 80]. Studies that do focus on spectral changes of EEG after AED administration generally have larger study groups [55, 57], but these consists mostly of healthy adult volunteers.

The patients in this study have received multiple AEDs. Phenobarbital is often administered as a first-line AED following the standard medication protocol. If seizure activity persists, midazolam is administered in addition, followed by lidocaine if necessary. All patients are outborn and phenobarbital is administered at the referring hospital and prior to the start of aEEG monitoring. The effects of phenobarbital on the aEEG and spectral properties of the EEG can therefore not be assessed. The success rate of resolving EEG seizures with phenobarbital has been reported to be low [86, 87], and often a complete lack of EEG or

clinical response is observed. From rat studies it is known that phenobarbital can increase the high frequency β power while reducing θ power for several hours [62]. Pharmacokinetic studies in neonates have shown serum half-life of approximately 115 hours for phenobarbital [64, 65]. We have therefore assumed steady-state influence of phenobarbital during the 4-hour analysis of midazolam and lidocaine. Midazolam is administered during the aEEG recording for most infants and lidocaine is administered after a median period of 141 minutes (range: 77-254). No relation is observed between the time from midazolam to lidocaine administration and the effect of lidocaine on spectral parameters. Baseline values of the total power and absolute band powers, except θ power, are significantly lower for the lidocaine group. Relative band power baseline values are similar for both groups, again with exception of θ power. The decreased baseline total power and absolute band powers and increased relative θ power in the lidocaine group may be the result of preceding midazolam administration. To minimize the influence of maintenance levels of AEDs, medication-related spectral changes have been determined through analysis of normalized data, i.e. relative to baseline values.

The time of administration is extracted from annotations present in the aEEG recordings. These annotations are entered by nursing personnel and are possibly inaccurate resulting in less accurate spectral analysis. This has been dealt with by averaging the power spectra over time periods of an hour, but the exact influence of this inaccuracy is unknown.

Furthermore, the medication serum levels have not been measured during the aEEG monitoring period. Variation of serum levels may decrease sensitivity to medication-related changes due to an increased variability between patients. Leuven *et al.* have reported no relation between midazolam metabolite serum levels and anticonvulsive effects [39]. A rat study of Mandema *et al.* has showed EEG spectral changes to be a function of midazolam plasma concentration [88]. For lidocaine, seizure reduction has been reported to be independent of plasma concentrations [74], but EEG spectral properties can be influenced by actual serum levels [70].

Finally, due to differences in firmware and hardware versions of the aEEG monitors used in this study, the power spectra of 11 out of 12 patients have been recalibrated in this study. This correction may induce noise in the very low (0-2 Hz) and high (15-20 Hz) frequency ranges. Frequency bins below 1 Hz are omitted for this reason. In 6 patients the correction factors are 10% for δ power and 55% for β power. In 5 patients the β power band has been corrected by 26%. The β power correction may appear large, but β powers only have a small contribution towards the total spectral power ($\sim 3\%$).

3.6 Conclusion

The EEG and aEEG are important diagnostic tools in assessing neonatal encephalopathy. A deep understanding of the effects of AEDs on the neonatal EEG is therefore crucial. For this reason spectral analysis of neonatal EEG has been performed during administration of AEDs in full-term neonates with PAIS. Both midazolam and lidocaine introduce a relative frequency shift towards higher frequency bands, mainly from δ band to θ band. This effect is more pronounced after lidocaine administration. Also, for lidocaine the effects are more pronounced for the ipsilateral (stroke-affected) hemisphere. Additionally, absolute total power is suppressed by midazolam, but not by lidocaine. This is also visible from aEEG background pattern observations. Midazolam decreases the aEEG background pattern immediately after administration for a duration of 30-60 minutes, whereas lidocaine does not have an effect on the aEEG background pattern. The aEEG results also indicate that midazolam is not effective in treating seizures in most neonates, while lidocaine has a high success rate of terminating seizure activity.

In conclusion, the effects of midazolam and lidocaine on neonatal (a)EEG have been quantified and shown to be profound. The results have shown that additional care has to be taken when evaluating (a)EEGs of neonates that are under the influence of AEDs. The spectral changes as seen in this study also differ significantly from spectral studies on AEDs as performed in adults, further indicating the importance of this study.

4 swLORETA source localization

4.1 Introduction

At the present time, most research into predictors for adverse neurological developmental outcome focuses on MRI-based techniques (including DWI) and longitudinal EEG [89-92]. The topic of 3D localization of electrical sources responsible for EEG has attracted increased attention in recent years, due to improvements in source reconstruction models [16-18, 93]. Since EEG is sensitive for brain injury immediately after birth, source reconstruction of the EEG might provide 3D localization information of encephalopathy at a very early stage, when MRI is typically still unavailable. Current EEG source localization studies have mainly been limited to adults and is not frequently used in newborns because of technical difficulties, e.g. lack of data concerning the newborn skull conductivity, thickness and homogeneity [19]. The aim of the study presented in this chapter is to evaluate the monitoring feasibility of EEG source localization by standardized weighted low resolution brain electromagnetic tomography (swLORETA) in full-term newborns with HIE.

4.2 Theory

4.2.1 Inverse problem

The main advantage of EEG measurements is their temporal resolution, which is in the order of milliseconds, while its biggest drawback is its spatial resolution. The 3D reconstruction of electrical sources responsible for EEG activity is termed the inverse problem. It is highly underdetermined due to the limited number of electrodes that can physically be attached to the scalp of the patient. The inverse problem is non-unique; there exist infinite numbers of electrical source distributions that will result in the exact same EEG signal. To limit the solution space, additional constraints about the physical and mathematical nature of the currents inside the brain have to be set (see section 4.2.2). In order to calculate a true tomography, the distributed electrical activity has to be computed throughout the brain volume. Towards this end the brain volume is discretized by a 3D grid of electrical sources of variable strength and orientation (i.e. voxels). For a definition of the forward problem, from which the inverse problem is derived, see Appendix E.

4.2.2 swLORETA

The source reconstruction model called LORETA (low resolution brain electromagnetic tomography) has been first published by Pascual-Marqui *et al.* in 1994 [16]. The physiological constraint that is imposed by this model to limit the number of solutions is the high probability of synchronicity between neighboring neurons. The view that EEG activity is produced by spatial summation of synchronized clusters of neurons undergoing postsynaptic potentials is widely accepted, and neuronal synchronicity is experimentally verified in several studies [94-96]. This physiological constraint translates to synchronicity between neighboring voxels in the discretized brain volume, i.e. the neighboring simulated sources are likely of similar magnitude and orientation. Mathematically, maximum synchronicity corresponds to the smoothest possible solution. This inherently means that the solution is a ‘blurred’ representation of the low spatial resolution of the actual distribution, but this solution does

comply with the EEG activity that is measured. Since its first publication, LORETA has been used for research in epilepsy [97-101], migraine [102], Alzheimer's disease [103] and Huntington's disease [104].

The model has been improved by the publication of standardized LORETA (sLORETA) by Pascual-Marqui in 2002 [17]. sLORETA produces probabilistic source distributions (whereas LORETA produces actual current distributions), that reflect the likelihood of the electrical generators to be found at a certain location in the brain. Hotspots in the probabilistic maps correspond to the high probability of the electrical generator to be situated at that location. The model has been shown to have zero-localization error for single dipoles in noiseless simulated data [17]. Standardized-weighted LORETA (swLORETA) is a subsequent modification of sLORETA, introduced by Palmero-Soler in 2009 [18]. This model compensates for the reconstruction of sources close to the location of the sensors by sLORETA. It enables the accurate reconstruction of surface and deep current sources in simulated data, even in the presence of noise or two simultaneously active dipoles [18]. It achieves this by implementation of a singular value decomposition of the lead field weighting matrix (that contains information about geometry and conductivity of the head model), which compensates for the sensors' sensitivity to current sources at different depths. swLORETA has been used for event-related potential studies on alcoholism [105] and attention [106].

A complete mathematical review of the swLORETA source localization method is out of the scope of this thesis. For the mathematical derivation of LORETA, sLORETA and swLORETA, see their respective articles [16-18].

4.3 Methods

4.3.1 Patient group

For this study two neonates with severe perinatal HIE and one neonate with MCA infarction have been selected. The three patients have been admitted to the Máxima Medical Center (Veldhoven, the Netherlands), between 2008 and 2010. These cases are representative examples of neonates with encephalopathy as encountered in the neonatal intensive care unit (NICU). The diagnosis of HIE is given when the following three criteria are met: (i) umbilical cord pH < 7.10, (ii) 5 minute Apgar score < 6, (iii) advanced resuscitation required immediately following birth. Details of the patient group are given in Table 4.1.

Table 4.1: Details of the three patients whose EEGs have been used in the 3D source localization study. Abbreviations are: ph=phenobarbital, mi=midazolam, li=lidocaine, cl=clonazepam, py=pyridoxine and n/a represents data that is not available.

	Patient 1	Patient 2	Patient 3
Male/female	Male	Male	Male
Diagnosis	HIE	HIE	MCA stroke
Gestational age (wks ^{days})	42 ⁰	38 ²	41 ¹
Birth weight (g)	3900	3225	3760
Apgar score at 1-5-10 min	5-5-6	4-5-8	9-10-n/a
Umbilical cord pH	6.80	6.82	n/a
Medication	ph-mi-li-cl	ph-mi-li-cl-py	none

Patient 1 – Hypoxic-Ischemic Encephalopathy

The first neonate is a boy born at full-term (gestational age 42⁰) by caesarean section after a placental abruption. Apgar scores are 5-5-6 at one, five and ten minutes after birth respectively. The neonate is intubated for ventilation by nasal continuous positive airway pressure (nCPAP) due to respiratory failure. During admission to the NICU the neonate has developed clinical seizures, which are treated with phenobarbital, midazolam and lidocaine. Initially the seizures are suppressed, but they return after terminating the administration of lidocaine. Pyridoxine dependent epilepsy has been ruled out. After administration of clonazepam, the EEG at day 6 shows a burst suppression pattern with epileptic spikes present during bursts. These spikes are more evident in the left hemisphere. Serial EEG performed during the first week has shown slit-like ventricles, without evidence of focal lesions. The MRI at day 6 shows extensive damage of the cortical areas, basal ganglia, optic radiation and WM, consistent with perinatal asphyxia (Sarnat III). Follow-up after 1 year has shown severe encephalopathy with motor, mental and visual disabilities.

Patient 2 – Hypoxic-Ischemic Encephalopathy

The second neonate is a boy born at full term (gestational age 38²) through vacuum extraction after a decelerated cardiotocogram. The amniotic fluid is meconium stained and umbilical cord strangulation is observed. Apgar scores are 4-5-8 at one, five and ten minutes after birth respectively. The neonate has been intubated and ventilated by nCPAP for two days due to respiratory failure. Ventilation is ceased after improvements are visible. The neonate develops neonatal convulsions and is transferred to the NICU subsequently. Treatment of seizures is started with phenobarbital and midazolam. Pyridoxine dependent epilepsy is ruled out. The EEG at day 2 initially shows *status epilepticus* which, after admission of lidocaine, turns into burst suppression with alternating long periods of little activity and bursts of epileptic activity. Clonazepam is administered but has no visual effect on the EEG. An MRI at day 2 shows ischemic damage at the cortex, the posterior limb of the capsula interna, thalamus and caudate nucleus. Also visible are generalized WM edema and a focal medio-occipital hemorrhage at the right hemisphere consistent with severe hypoxic ischemia. After multi-disciplinary consideration, intensive care treatment is withdrawn and the neonate has died in the second week of life.

Patient 3 – Middle Cerebral Artery infarction

The third neonate is a boy born at full term (gestational age 41¹) after a spontaneous vaginal partus. The amniotic fluid is stained with meconium. Apgar scores are 9 and 10 at 1 and 5 minutes after birth respectively. The patient develops central apnea at 12 hours of age, is resuscitated, intubated and transferred to the NICU. EEG at day 1 shows asymmetrical ventricles and an area of increased echodensity parieto-temporally, indicative of stroke. CT at day 1 shows a large MCA of the right hemisphere. An MRI on day 4 shows an additional partial infarction in the right occipital region and agenesis of the right posterior communicating artery. Damage to the basal ganglia as well as to the corticospinal tract is also visible. The aEEG shows no signs of convulsions. EEG at day 5 shows a disturbed background pattern and predominant activity of the left hemisphere with sharp spikes. No AEDs are administered. At 6 months of age the patient has developed refractory epilepsy and a hemispherectomy (i.e. removal of the ipsilateral hemisphere) is performed to control seizures in combination with AEDs. Follow-up at 2 years of age shows severe encephalopathy with left-sided hemiplegia and mental disabilities.

4.3.2 Data acquisition

EEG: Digital EEG recordings are obtained on day six (neonate 1), day two (neonate 2) and day five (neonate 3) after birth. Recordings are acquired with a Nicolet Monitor (NicoletOne, Viasys Healthcare, Conshohocken, PA, USA). Patient skin is prepared with a slightly abrasive gel (Nuprep Gel, D.O. Weaver, Aurora, CO, USA), effectively lowering skin impedance and improving the quality of the recordings. Twenty-one electrodes (nineteen scalp electrodes) are placed according to the international 10-20 system (a description is given in section 2.2.1). These electrodes are filled with a conductive past (Ten20, D.O. Weaver, Aurora, CO, USA), assuring optimal signal conduction and electrode adhesiveness. Electrode impedance is kept below 10 k Ω . The EEG is sampled with 512 Hz and digitally stored.

MRI: MRI images are obtained within one day from the EEG recordings; on day six (neonate 1), day two (neonate 2) and day four (neonate 3) after birth. MRI sequencing is performed on a 1.0 Tesla imaging unit (Gyrosan, Philips Medical Systems, Best, the Netherlands). The imaging protocol is described by van Pul *et al.* [92]. Patients are sedated with chloral hydrate and fixated using a vacuum pillow. The heads of the patients are placed in a standard birdcage coil. MRI acquisition consists of T₁-weighted spin-echo (repetition time: 568 ms, echo time: 18 ms), T₂-weighted fast spin-echo (repetition time: 4381 ms, echo time: 120 ms) and inversion recovery (repetition time: 3436 ms, echo time 18 ms and inversion time: 400 ms). Additionally, the protocol also includes DWI with single-shot echo-planar MRI. Twenty adjacent sections are recorded within 3 minutes (repetition time: 3595 ms, echo time: 82 ms) and a voxel size of $1.56 \times 1.56 \times 3$ mm. Three b-values (0, 400, 800 s/mm²) are used for calculation of the apparent diffusion coefficient (ADC). The MRI images are compared with the EEG inverse solutions as obtained from swLORETA analysis.

4.3.3 Data analysis

Head model: A 3D head model is required for source localization of the EEGs by swLORETA. Accurate head models can be obtained from individual MRI data by segmentation. However, in this study a head model constructed from a standard MRI data set is used for all patients. The reason for this approach is twofold: (i) the aim of this study is to investigate the feasibility of monitoring aspects of swLORETA shortly after birth, when EEG recordings typically are available and MRI data are not, (ii) the MRI data as obtained following the clinical acquisition protocol (described in section 4.3.2) are inadequate for 3D source localization (low spatial resolutions, small and incomplete scan volumes and low image contrasts).

A standard high resolution adult MRI dataset (Colin 27, Montreal Neurological Institute) is used for construction of the head model [107]. This dataset is constructed from 27 T₁-weighted volumes (7×0.78 mm³ and 20×1.0 mm³) and 12 T₂-proton density-weighted volumes that are registered to a common stereotaxic space and intensity averaged. Signal-to-noise ratio increases with the square root of the number of scans and the resulting dataset consists of high quality anatomical images with high signal-to-noise ratio, see Figure 4.1. A head model is constructed from this dataset by segmentation using ASA® (ANT, Enschede, the Netherlands). Segmentation of MRI slices consists of applying intensity thresholds and using a region-growing algorithm to separate brain, skull and scalp areas. The head model is obtained by subsequent application of a boundary element method. A 0.14 mm mesh with an additional 0.1 mm scalp-rendering for the scalp is used, and a 0.16 mm mesh for skull and brain. The resulting model consists of brain, skull and scalp volumes and is displayed in Figure 4.2. Each volume is attributed a conductivity value; 0.33, 0.0042 and 0.33 S/m for brain, skull and scalp, respectively [19, 108, 109].

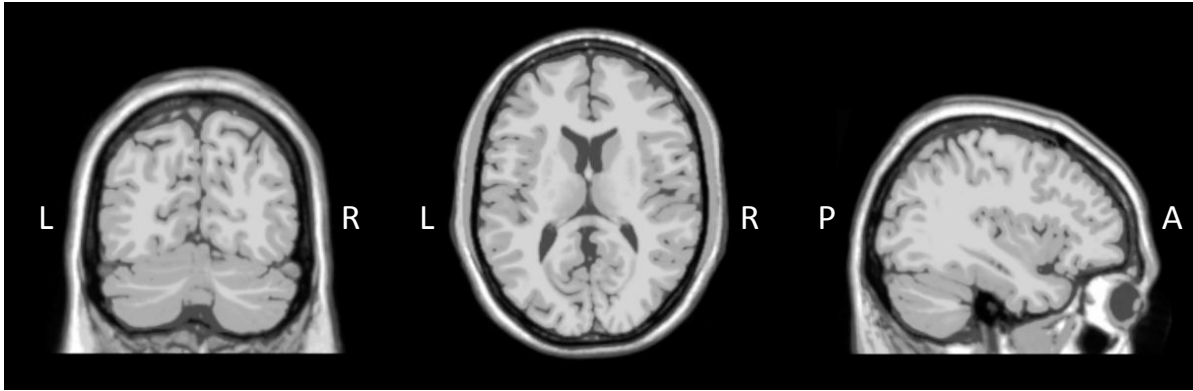


Figure 4.1: High resolution adult MRI dataset (Colin 27) as used for generating the head model in this study. 27 T_1 -weighted scans and 12 T_2 -proton density-weighted scans are intensity averaged resulting in a single volume with high signal to noise ratio in all 3 dimensions. Abbreviations are: L=left, R=right, P=posterior and A=anterior.

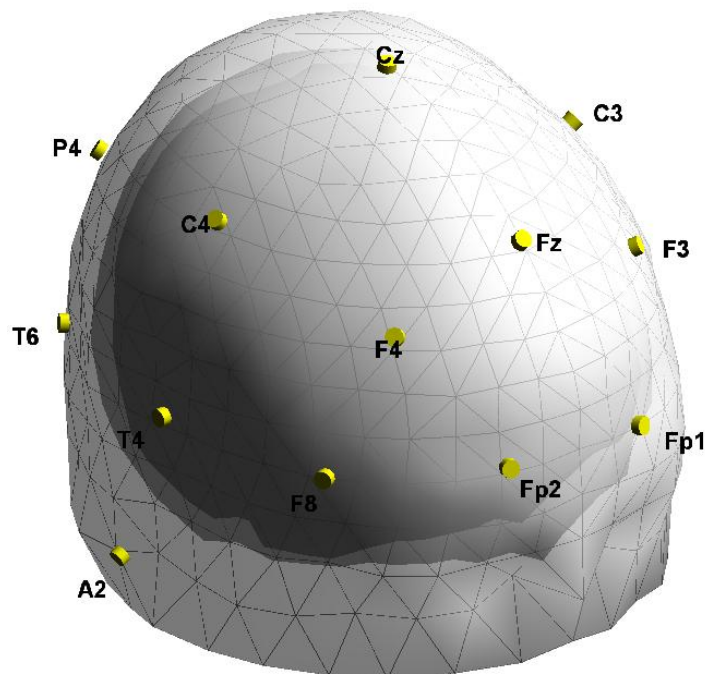


Figure 4.2: Standard head model as used for 3D source localization for all patients in this study. The model is constructed by segmentation of the Colin 27 MRI dataset and consists of a brain, skull and scalp volume. Electrode locations are situated on the surface of the scalp volume.

swLORETA: Source localization is performed by the calculation of swLORETA inverse solutions, again in ASA® (ANT, Enschede, the Netherlands). First, EEG data are high-pass filtered at 0.53 Hz, low-pass filtered at 30 Hz and a 50 Hz notch filter is applied. EEG segments that are selected for source localization vary in length from 35 minutes (neonate 1), 40 minutes (neonate 2) and 25 minutes (neonate 3). swLORETA inverse solutions are calculated for every time sample (512 solutions for every second) and subsequently averaged over the entire length of the EEG segment. To reduce memory load during average calculation the EEG data are divided into 2-s segments prior to source localization and subsequent averaging. The inverse solution is calculated by modeling current dipoles of varying magnitude and orientation inside the brain volume at 7 mm isotropic resolution (results in 5902 dipoles). An example of a source localization result is shown in Figure 4.3. The EEG

inverse solution is projected onto slices of a standard MRI dataset and is ready to be compared with MRI data of the patient.

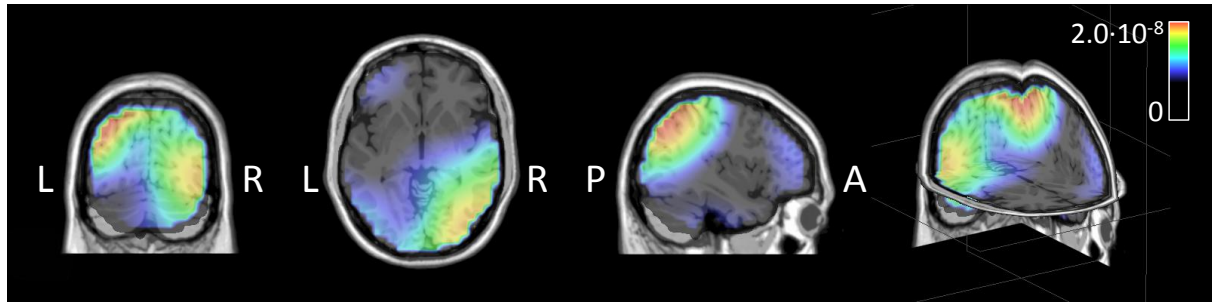


Figure 4.3: Example swLORETA inverse solution data. From left to right a coronal, axial and sagittal slice are shown together with an orientation of these slices in 3D space. Inverse solution data is modeled by 5902 dipoles of varying magnitude at 7 mm resolution and depicted by a color map onto a standard MRI dataset. The values are standardized and unitless. Abbreviations are: L=left, R=right, P=posterior and A=anterior. Two hotspots are visible in the posterior area of the brain both left and right.

Robustness of the swLORETA method as applied in this study has been assessed by analyzing the EEG recordings with varying spatial resolution and sub-segment length. Spatial resolution of the solution space (i.e. voxel size) is varied between 7 mm and 20 mm, while EEG segment length is varied between 0.5 and 8 seconds prior to swLORETA source localization and averaging. Both parameters do not significantly change the current density probability distributions as calculated by swLORETA.

4.4 Results

Patient 1

A representative 20-s segment of the 35-min EEG recording of patient 1 performed at day six after birth is shown in Figure 4.4. The EEG background is discontinuous and interhemispheric asynchrony is evident. Abnormal activity included random and rhythmic delta brushes in left and right temporal and parietal regions of the brain, i.e. delta waves (0.3-1.5 Hz) with an amplitude of 50-300 μV and superimposed alpha or beta rhythms (>8 Hz). Delta brushes are typical in preterm neonates, but normally disappear in healthy full-term neonates. The EEG does not display electrographic seizure activity.

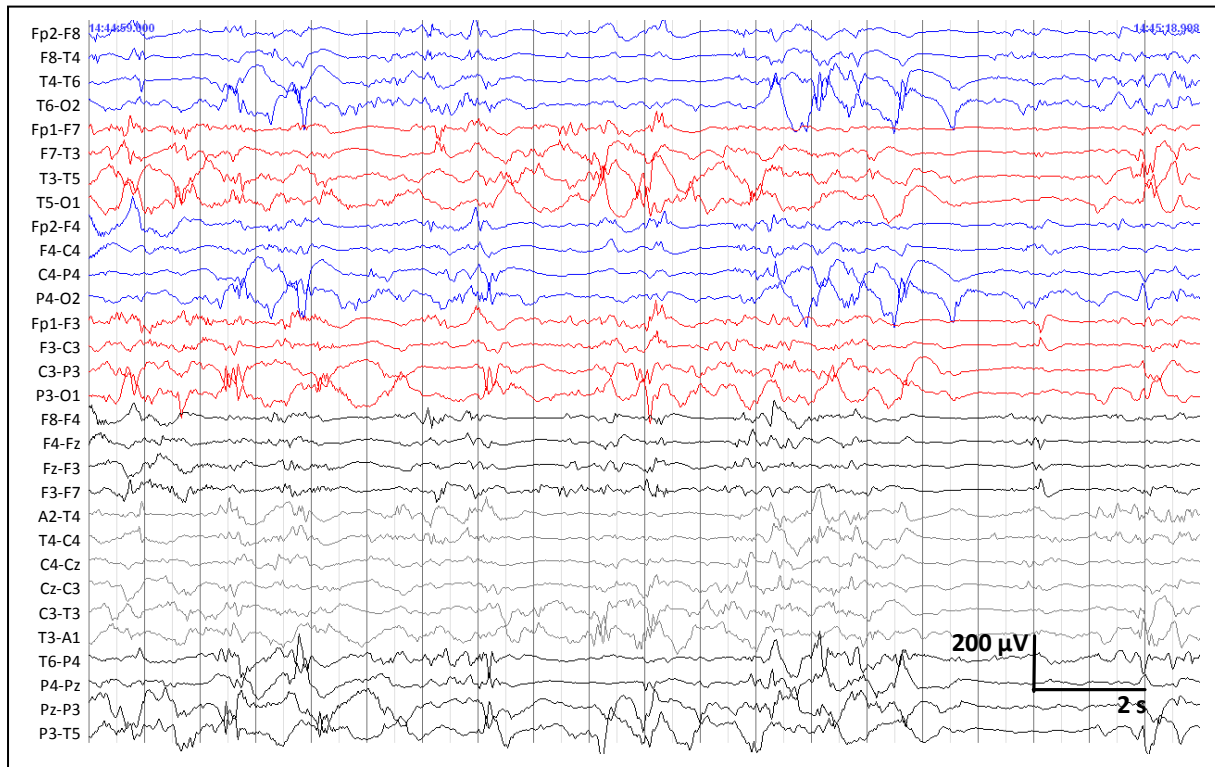


Figure 4.4: A representative 20-s segment of EEG data of patient 1 performed at day 6 after birth. The background pattern is discontinuous with interhemispheric asynchrony. Delta brushes and rhythmic delta activity with short bursts of spikes over left and right temporal and parietal regions are present. No electrographic seizure activity is observed.

MRI scans (DWI, ADC, T_2), performed on day six after birth, are displayed together with the swLORETA source localization in Figure 4.5. DWI shows extensive damage of the cortical areas, basal ganglia, optic radiation and WM, indicating severe hypoxic-ischemic encephalopathy. Diffusion abnormalities are present in corpus callosum and splenium. Follow-up MRI performed at day ten after birth shows diffusion abnormalities in basal ganglia and cortical highlighting (abnormal signal intensity at the cortex, not shown).

The current density distribution as calculated by swLORETA from the 35-min EEG recording shows maximum current density probability in left and right parietal, temporal and occipital regions of the brain (Figure 4.5). Maximum dipole probability is $0.69 \cdot 10^{-8}$ while the probabilities in central and frontal areas are $0.40 \cdot 10^{-8}$ and $0.37 \cdot 10^{-8}$. The low current density probability in the swLORETA inverse solution correlates with the MRI abnormalities in basal ganglia and frontal areas. This low probability indicates a loss of EEG activity in these areas.

Abnormalities in optic radiation and WM, as observed in the MRI data, are not visible in the inverse solution.

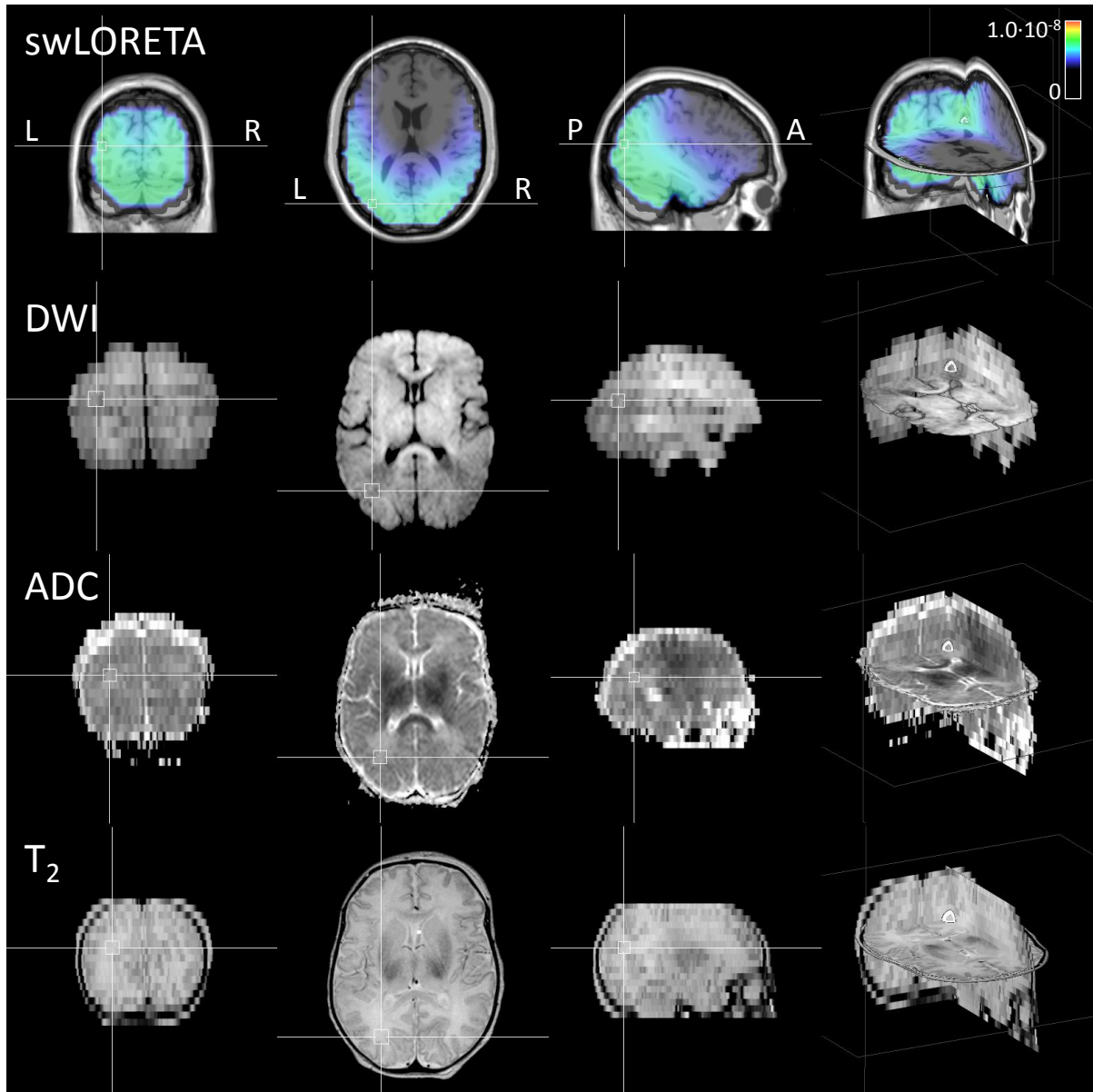


Figure 4.5: MRI images of patient 1 (DWI, ADC, T_2) displayed together with the swLORETA source localization. The color bar represents the current density probability, with red indicating a high probability for a current density hotspot. The inverse solution indicates that most EEG activity is situated in parietal, temporal and occipital lobes.

Patient 2

A representative 20-s segment of the 40-min EEG recording of patient 2 performed at day two after birth is shown in Figure 4.6. The background pattern is severely depressed initially, with slow seizure activity in the frontal and temporal regions. This seizure activity is mainly present in the right hemisphere. After midazolam administration the EEG background changes to burst suppression. On average one burst occurs every ten seconds, often consisting of multiple spikes. The electrographic seizure activity disappears, but short and sharp spikes are occasionally observed in left and right frontal regions.

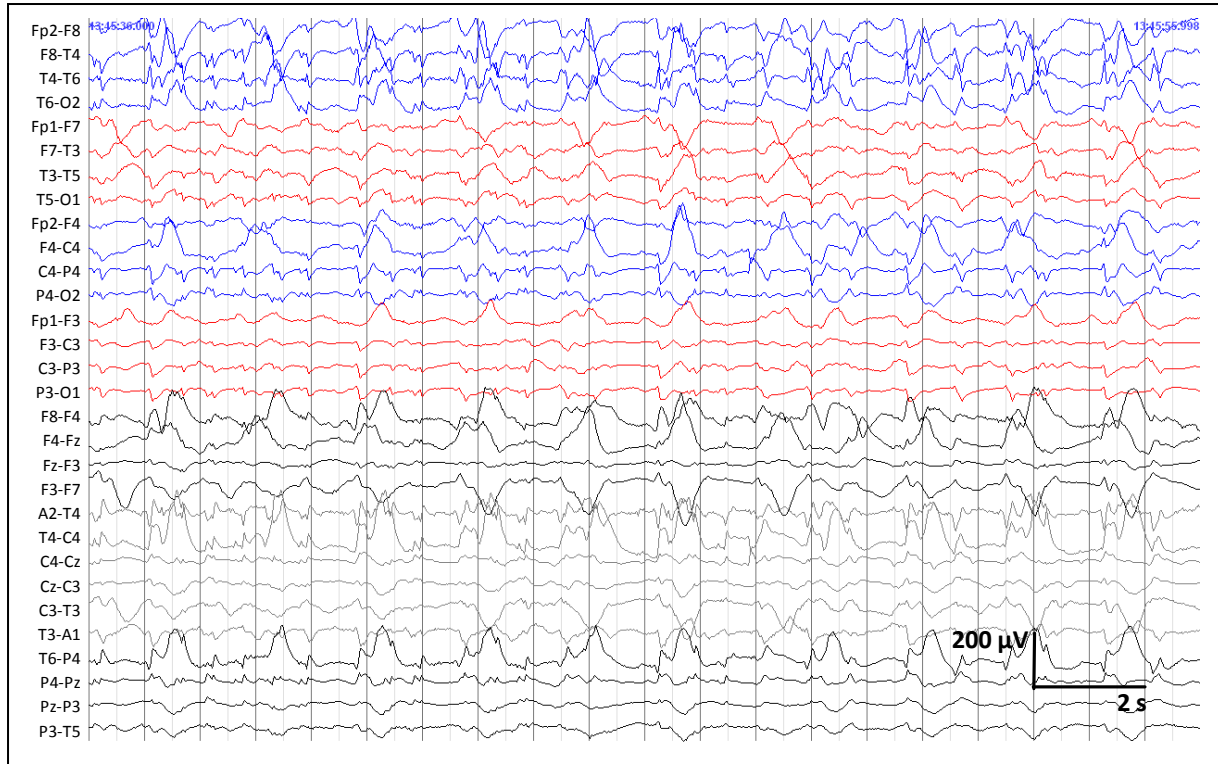


Figure 4.6: A representative 20-s segment of EEG data of patient 2 performed at day 2 after birth. Initially, the EEG background pattern is severely suppressed with continuous slow seizure activity over frontal and temporal regions. After midazolam administration the background pattern changed to burst suppression. The electrographic seizure activity disappeared, but sharp short spikes over left and right frontal regions are occasionally observed.

MRI scans (DWI, ADC, T_2), performed on day two after birth, are displayed together with the swLORETA inverse solution in Figure 4.7. DWI shows ischemic damage at the cortex (cortical highlighting), posterior limb of the capsula interna, thalamus and caudate nucleus. Also visible is generalized WM edema and a focal medio-occipital hemorrhage in the right hemisphere.

The inverse solution of the 40-minute EEG recording shows a current density probability hotspot in the right frontal and temporal lobes, corresponding with the Fp2, F4, F8 and T4 electrodes (Figure 4.7). The maximum current density probability in this region is $0.97 \cdot 10^{-8}$. The current density probability in other areas of the brain is distributed homogeneously at an average value of $0.47 \cdot 10^{-8}$ and lowest in the left parietal region. The right frontal and temporal hotspots in the inverse solution correlate well with the EEG recording, showing seizure activity mainly at these locations. The hemorrhage in the right occipital, as observed in the MRI, is not seen in the inverse solution.

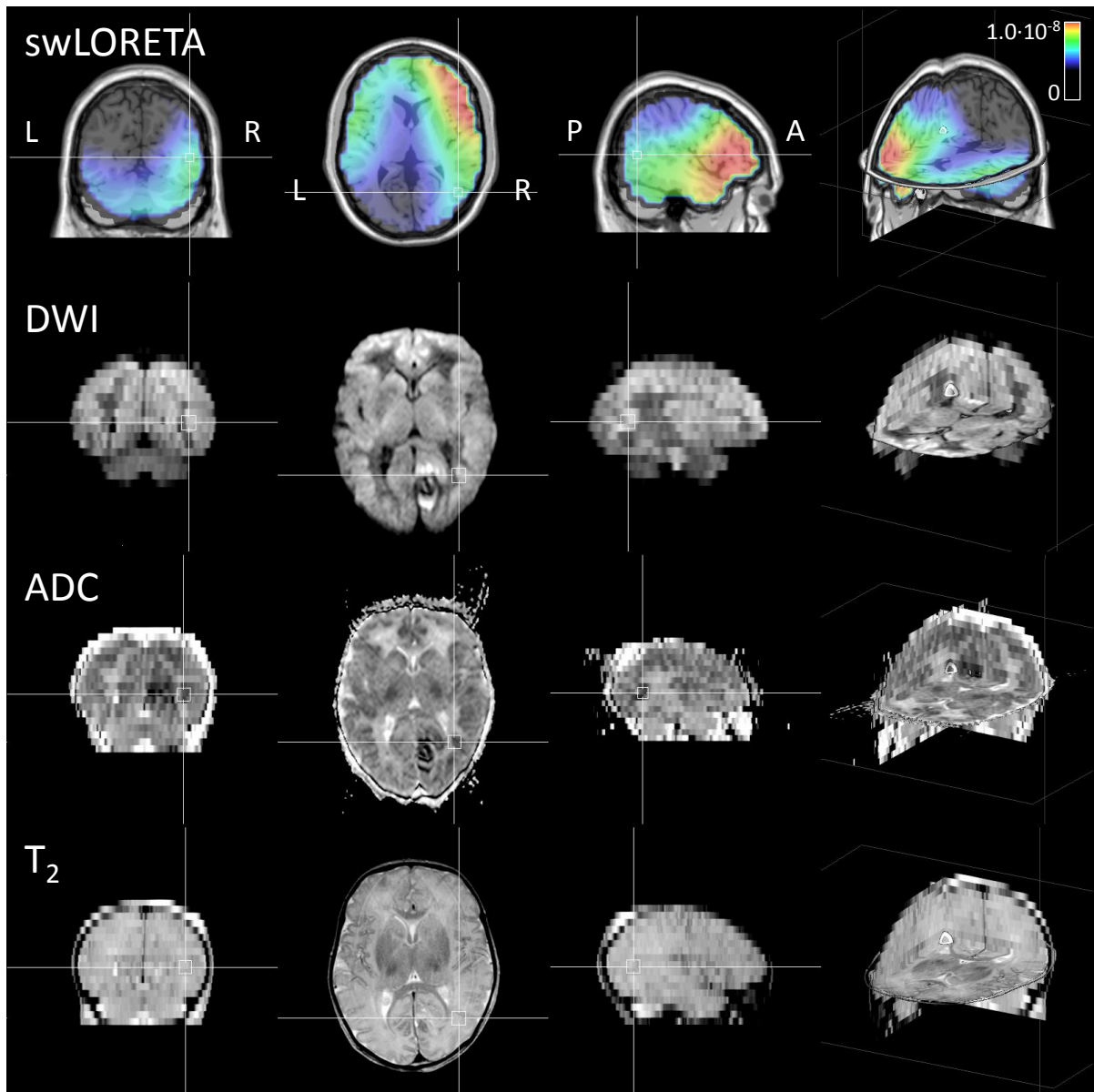


Figure 4.7: MRI images of patient 2 (DWI, ADC, T_2) displayed together with the swLORETA inverse solution. The inverse solution indicates that most EEG activity is situated in the right frontal and temporal lobes. The focal hemorrhage in the right occipital region as visible in the MRI is not observed in the inverse solution.

Patient 3

A representative 20-s segment of the 25-min EEG recording of patient 3, performed at day five after birth, is shown in Figure 4.8. The EEG background pattern shows asymmetric activity. On the left side, a continuous background pattern is observed with mainly delta and beta activity. The right side has a depressed background pattern and displays a large number of frontal sharp transients.

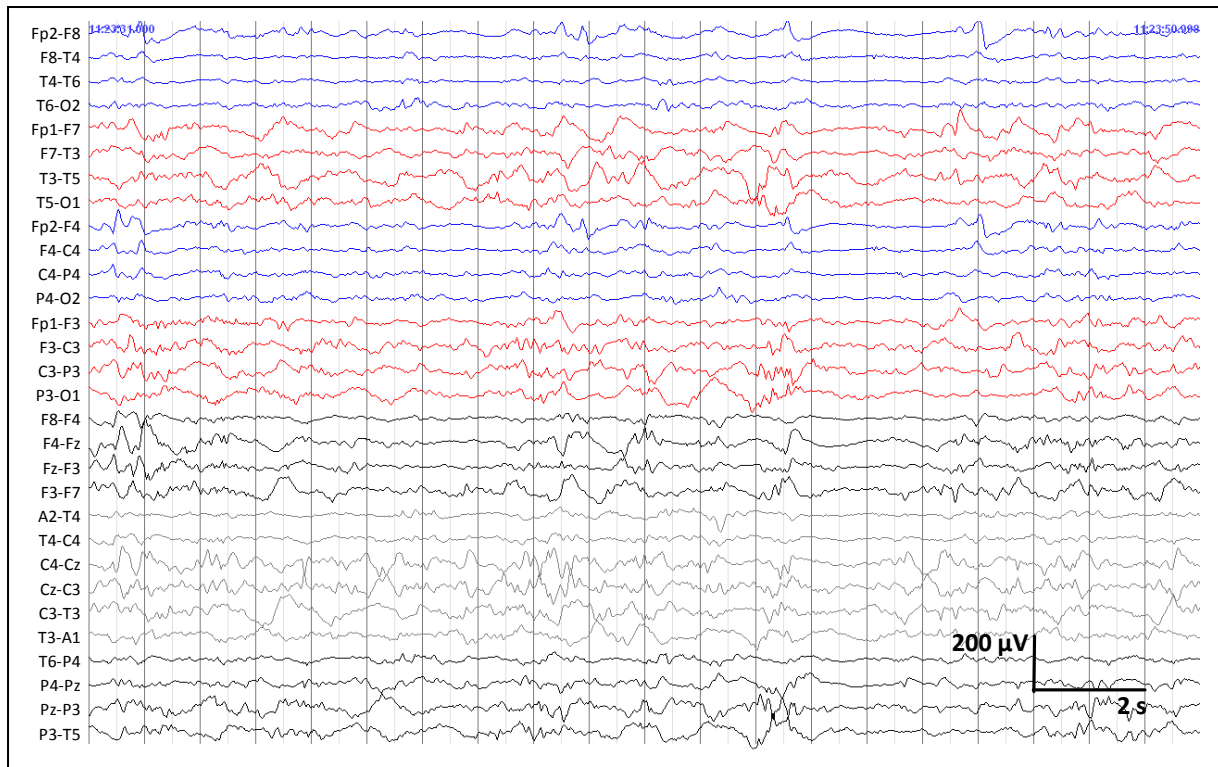


Figure 4.8: Representative 20-s segment of the 25-min EEG recording of patient 3 performed at day 5 after birth. The background activity is asymmetric, the left hemisphere has a continuous background pattern with delta and beta activity, the background pattern of the right hemisphere is depressed and shows frontal sharp transients.

MRI data (DWI, ADC, T_2), obtained on day four after birth, are shown together with the swLORETA inverse solution in Figure 4.9. DWI shows large diffusion abnormalities in the right hemisphere, indicative of a right MCA occlusion. An additional infarction in the right occipital region together with agenesis of the right posterior communicating artery is also visible. High signal intensities at the corticospinal tract are visible, indicative of Wallerian degeneration, i.e. degeneration of an axon that is separated from the body of the neuronal cell. Reduced diffusion is visible in corpus callosum and anterior and posterior limb of the internal capsule.

The inverse solution as calculated by swLORETA from the 25-min EEG recording shows activity to be mainly situated in the left hemisphere. The maximum current density probability in this hemisphere is $0.63 \cdot 10^{-8}$, while the stroke-affected hemisphere has an average probability of $0.30 \cdot 10^{-8}$. This low probability correlates with the location of the infarction as visible in the MRI data.

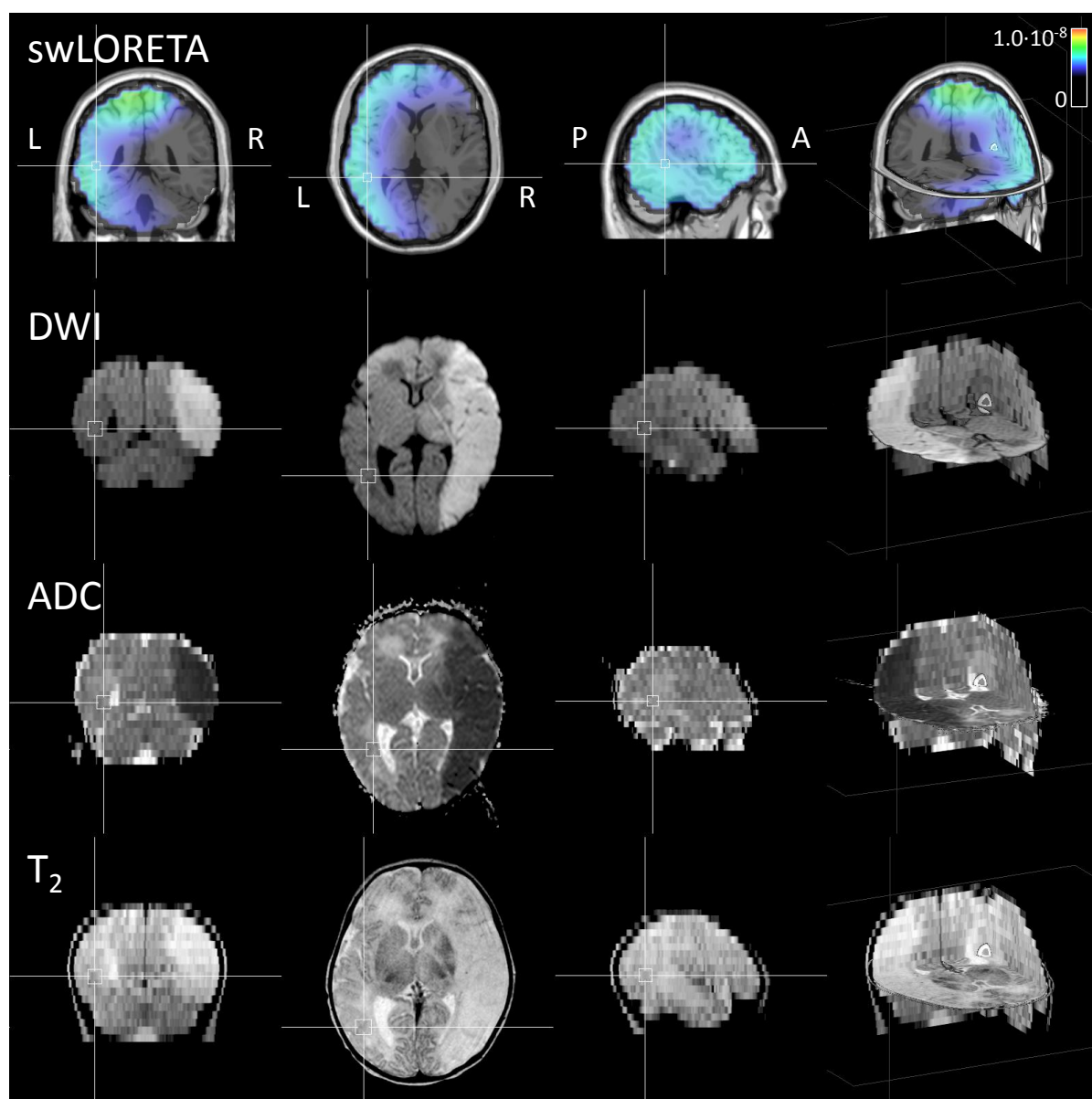


Figure 4.9: MRI images of patient 3 displayed together with the swLORETA inverse solution. The inverse solution indicates that most EEG activity is situated in the left hemisphere. MRI data shows a large MCA infarction in the right hemisphere.

4.5 Discussion

Patient 1

The MRI data has shown abnormalities in frontal areas and basal ganglia, indicative of hypoxic-ischemic encephalopathy. The inverse solution calculated with swLORETA shows low signal probability in these regions correlating with MRI images. Thordstein *et al.* have shown that post-asphyctic full-term neonates have suppressed low frequency EEG power when compared with healthy neonates, while high frequency power remained the same [110]. The swLORETA method as implemented in this study calculates inverse solutions of the total EEG spectrum, and does not discriminate changes in low and high frequency activity. Source localization of delta band filtered EEG data (1-4 Hz) confirms reduced low frequency power in the hypoxic-ischemic regions, in agreement with Thordstein *et al* (not shown).

The MRI data also shows damage to the optic radiation which is not observed in the calculated inverse solution. This is likely due to the inability of the swLORETA calculation to detect features at the small scale of the optic radiation. Additionally, damage to the occipital WM is observed in the MRI images, but not seen after source localization. Inder *et al.* have seen a decreased SEF following WM damage while the EEG amplitude remained the same [111]. This indicates that EEG total power remains unchanged after WM damage, but a frequency shift from high to low frequencies occurs. Since the swLORETA calculation in this study relies on the total EEG power this might explain why WM damage is not observed in the inverse solution.

Patient 2

The MRI of this patient indicates frontal cortical highlighting. This may cause the seizure activity as seen in the EEG and the increased current density probability in the swLORETA inverse solution. The focal medio-occipital hemorrhage in the right hemisphere as seen in DWI is not detected by swLORETA. Mirkovic *et al.* have shown good correlation between hemorrhage location and reconstructed sources of epileptic spikes in neonatal EEG recordings [112]. Segments are ultra-short (40 ms) and located at the maximum peak value of the spikes. In the same study it has been shown that selecting segments of away from the epileptic spike peak value result in a lower accuracy of reconstructed sources compared with hemorrhage location. In this study reconstructed sources are averaged over long segments possibly preventing accurate hemorrhagic lesion localization. Also, in the study from Mirkovic *et al.* lesions are located near the cortex, whereas in this patient the lesion is situated in the WM. Claassen *et al.* have shown that electrographic seizure activity occurs in only a small percentage of patients with intracerebral hemorrhage, and incidence decreases with increasing distance from the cortex [113]. Possibly, the hemorrhage in this patient may not generate electrographic seizures and this prevents detection. Finally, Inder *et al.* have shown that EEG amplitude is largely unaffected by WM lesions which may hamper detection by swLORETA as implemented in this study.

Patient 3

The large stroke-induced diffusion abnormality in the right hemisphere as seen in the MRI corresponds to a region of low current density probability in the swLORETA inverse solution. The resulting regional loss of cerebral function is also evident in the EEG recording from which the inverse solution is calculated. This is in agreement with Koelfen *et al.* who have reported a correlation between the infarction location and the region of abnormalities as observed in EEG recordings [114]. EEG abnormalities include focal slowing and sharp waves, or localized amplitude suppression at the site of infarction. This localized amplitude reduction is clearly evident in the EEG of patient 3 and easily seen after swLORETA source

localization. Thordstein *et al.* have shown that low frequency EEG power is reduced when hypoxic-ischemic damage is present [110]. As most power in the neonatal EEG resides in the delta band (section 3.4.2), this indicates that hypoxic-ischemia reduces total EEG power, as is evident in the stroke-affected region of this patient.

In summary, hypoxic-ischemic areas visible in MRI data correlate with regions of low current density probability of the inverse solution as calculated by swLORETA (patient 1 and 3). Additionally, electrographic seizure activity may be localized by swLORETA, while corresponding focal abnormalities might not be visible in the MRI (patient 2).

Limitations

The head model used in this study is based on a standardized set of MRI data from a single adult. This likely introduces uncertainties in source localizations due to the size difference when compared to a neonatal head, but also due to possible differences in volume ratios of the brain/skull/scalp compartments and conductivities. Higher source localization accuracy may be expected when head models are based on individual neonatal MRI data. This would require a change of the standard neonatal scanning protocol to meet the requirements necessary for accurate head model generation (increased resolution and included scalp and skull areas in the scan volume). Roche-Labarbe *et al.* have studied the influence of different neonatal head models on the accuracy of dipole localizations reconstructed from EEG data. Influence of skull layer thickness, conductivity and presence of a fontanel are investigated. Skull layer thickness is shown to have a large influence on dipole magnitude, but not on orientation and location of the dipole. The mean difference in dipole locations between normal and increased skull thickness are 5.9 ± 3.2 mm, with a 7.9% increase in dipole magnitude for the model with increased skull thickness. Likewise, skull conductivity only influences dipole strength, but not dipole orientation. The mean difference between dipole locations in 0.0042 and 0.33 S/m skull conductivity head models is 11.6 ± 2.6 mm, with an average decrease of 29.7% in dipole magnitude for the 0.33 S/m model. The presence of a fontanel does not have a significant effect on both dipole magnitude and orientation. The mean distance between dipole locations for the normal and fontanel head model is only 2.0 ± 2.1 mm, and the dipole magnitude is 2.1% higher in the fontanel head model. These results indicate that higher accuracy may be obtained when an accurate neonatal head model is used when performing source localizations. However, improvements are mainly anticipated in dipole magnitudes and not orientation. It is likely that this will not influence the interpretation of swLORETA inverse solutions, since the hotspot locations of the probability distributions will likely remain situated at the same position in the brain. Furthermore, a generic head model allows for bed-side monitoring at an early stage after birth when MRI is commonly not yet available.

Another limitation is the model of the brain volume in the head model as applied in this study. This volume includes the entire brain and no distinction is made between GM and WM. Other studies have limited the dipole locations of the inverse solution to the GM [93, 97, 98, 100-103, 115], based on probabilistic brain tissue maps [106, 116, 117]. Voxels are labeled GM if three conditions are met: (i) GM probability is higher than WM probability, (ii) GM probability is higher than cerebrospinal fluid probability and (iii) GM probability is higher than 33%. In this study, visual assessment shows that hotspots of current density probability distributions are mainly located in GM.

Several studies have investigated the location error of electrode placement and errors up to 10 mm are reported [118-120]. These errors arise mainly due to anatomical variability of the inion and the difficulty in determining its location by palpation. According to Hellström *et al.* these errors are higher for neonates than adults [121]. Due to the immaturity of the neonatal

brain the anatomical landmarks and the underlying areas of the cerebral cortex may differ between neonates. Scalp looseness and extra difficulty in determining inion location in neonates can further decrease electrode placement accuracy. These errors can be important when subsequent source localization is performed, as is the case in this study. Dipole source localization errors due to electrode location inaccuracy have been reported to be up to 10 mm [118, 119].

The source analysis algorithm swLORETA assumes synchronicity between neighboring voxels of the brain volume to limit the number of inverse solutions. This is based on the generally accepted view that extracranial EEG measurements are generated by cortical pyramidal neurons undergoing synchronous postsynaptic potentials. The amplitude of the measured signal is the result of a spatial summation of underlying clustered and synchronized neurons. Experimental evidence of synchronization between neighboring neurons has been reported in literature [94-96]. The inter-electrode distance is in the order of centimeters and this is often criticized to be a limiting factor for the resolution of the solution space, and is used as an argument for the inappropriateness of selecting voxel sizes below 1 cm [122]. However, a limit in the resolution of measurement space does not prohibit the modeling of the solution space at higher resolutions [123]. According to Hämäläinen *et al.* typical cluster sizes of simultaneously active synapses of 40-200 mm² are necessary for generating experimentally measured current densities of 100-250 nA/mm² [29].

4.6 Conclusion

Interest in source localization of EEG recordings has been growing rapidly in recent years. Research has focused mainly on the improvement of source reconstruction methods and applications in encephalopathy research in adults. This is the first study demonstrating monitoring applications of source localization by swLORETA in full-term neonates with perinatal hypoxic-ischemia. Low current density probabilities in the swLORETA inverse solutions correlate with hypoxic-ischemic areas as visible on MRI. Furthermore, neonatal seizure activity may be localized by swLORETA which is not visible in MRI data. The calculated inverse solutions of the EEG recordings may provide easy-to-interpret localized information of neonatal brain function, possibly enabling longitudinal monitoring and assessment of treatment efficacy as well as providing a guide for cerebral imaging studies. Additionally, since EEG data are available from the first day after birth, whereas MRI data are typically available one week after birth, EEG source localization may allow early diagnosis of possible encephalopathy in neonates.

5 Summary

The first aim of this study has been the quantification of the spectral effects of AEDs on the EEG in full-term neonates with PAIS (**Chapter 3**). The second aim of this has been the investigation of the feasibility of monitoring applications of 3D source localization by swLORETA in full-term neonates with HIE (**Chapter 4**).

The spectral effects of AED have been quantified in full-term neonates with PAIS. Results have been compared with analysis of aEEG following AED administration. Profound effects of AEDs on neonatal (a)EEG have been quantified. Midazolam decreases absolute total power within 30-60 minutes and then stabilizes. This suppression may result in aEEG background degradation. Relative frequency powers following midazolam administration indicate a shift towards higher frequencies ($\delta \rightarrow \theta$). Effectiveness of midazolam seizure suppression has been shown to be low. Lidocaine does not suppress total absolute power or aEEG background. Relative frequency powers again show a shift towards higher frequencies following AED administration ($\delta \rightarrow \theta$ & α). The effects of lidocaine are more pronounced in the stroke-affected hemisphere. Contrary to midazolam, lidocaine is highly effective in suppressing repetitive seizures and *status epilepticus*.

The results from this study differ significantly from spectral studies on AEDs as performed in adults. The results indicate that EEGs from neonates under the influence of AEDs should be interpreted with extra care to prevent misinterpretation of the increased relative high frequency activity.

Spatial information obtained through EEG measurements is limited to the cortex. However, abnormalities in WM or deep nuclei may indirectly affect electrocortical activity as measured by EEG, since they are part of relay networks connected with the cerebral cortex. Therefore, 3D source localization by swLORETA has been performed for the first time in neonates with HIE, to investigate the feasibility of monitoring applications.

The results indicate that low current density probabilities in the swLORETA inverse solutions correspond to hypoxic-ischemic areas as visible on MRI. Furthermore, neonatal seizure activity may be localized by swLORETA, which is not visible in MRI data. These results indicate that the current study setup may enable longitudinal bed-side monitoring of neonates at-risk, assessment of treatment efficacy as well as providing a guide for cerebral imaging studies. Additionally, since EEG data are available from the first day after birth, whereas MRI data are typically available one week after birth, EEG source localization may allow early diagnosis of possible encephalopathy in neonates.

6 Recommendations

The study on spectral effects of AEDs in neonates with PAIS can be improved in several aspects. The current patient group is small and contains variety in infarct sizes, infarct locations and timing of AED administration. A larger and more homogeneous patient group would likely results in smaller IQR ranges of the averaged parameters of the power spectra. However, a larger patient group would allow a subdivision into smaller patient groups with similar AED administration timings. The number of patients presenting with PAIS is limited per hospital and thus collaboration between hospitals would be necessary to enlarge the patient group. Direct control of AED administration timings is not possible, since AEDs are administered at onset of clinical symptoms.

An improvement in measurement setup is also possible. Different aEEG monitors have different frequency responses and this hampers direct comparison of data. It has been shown that firmware upgrades of a single aEEG monitor can result in significantly altered frequency responses due to adjusted filter settings. If frequency responses between different aEEG monitors are matched prior to the measurements, e.g. by changing filter settings, the calculated power spectra do not have to be corrected afterwards, which would reduce the introduction of noise and improve the overall quality of the analysis.

As a final improvement the measurement of AED serum levels during (a)EEG recordings is recommended. It has been shown in literature that midazolam and lidocaine serum levels can influence EEG activity. It has also been shown in literature that lidocaine serum level is dependent on gestational age. EEG activity following similar lidocaine loading doses may therefore differ between patients. It is important to further investigate the dependence of EEG activity on actual AED serum levels.

The study on the monitoring capabilities of swLORETA source localization can also be further improved. The current study setup should be applied to a larger patient group and of homogeneous encephalopathy. Multiple patient groups can be defined based on different encephalopathy. This would allow the exploration of the monitoring capabilities across distinct types of brain injury.

The current 3D source localizations are performed on a generic adult head model. A generic neonatal head model has to be constructed, since differences in size, volume ratios of brain/skull/scalp compartments and conductivities are likely to be of importance to the accuracy of the reconstruction. The brain compartment also needs to be modeled more realistically, i.e. containing actual hemispheres and a distinction between WM and GM. The influence between a generic head model and an individual head model may also be explored further. Possible monitoring applications of swLORETA will rely on a generic head model when used shortly after birth. It is therefore important to know the amount of inaccuracy this introduces when compared with the use of an individual head model.

The study setup can also be altered to investigate other aspects of the swLORETA source localization algorithm. Using short EEG segments allows the exploration of source reconstruction of short and lower voltage EEG transients, which are lost when multiple current density distributions of large segments are averaged. swLORETA can also be investigated in the frequency domain. Studies have indicated that WM injury introduces frequency shifts that can possibly be detected by performing source localization in the frequency domain.

Finally, inter-subject deviations in electrode placement may decrease the accuracy of the source localizations. The reported errors for electrode placement and source localizations are based on studies performed on adults. Although the overall visualization and interpretation of cerebral function is expected to be similar when errors in electrode placement are lowered, this effect has to be studied based on neonatal data.

Appendix A Classification of aEEG

Background patterns

The classification of aEEG background patterns is based on minimum and maximum amplitudes of the signals [37, 42-44]. The five possible background patterns, ordered from good to bad, are: continuous normal voltage (CNV), discontinuous normal voltage (DNV), continuous low voltage (CLV), burst suppression (BS) and flat trace (FT). Examples are shown in Figure A.1. The classification of the patterns according to their amplitude ranges is given in Table A.1.

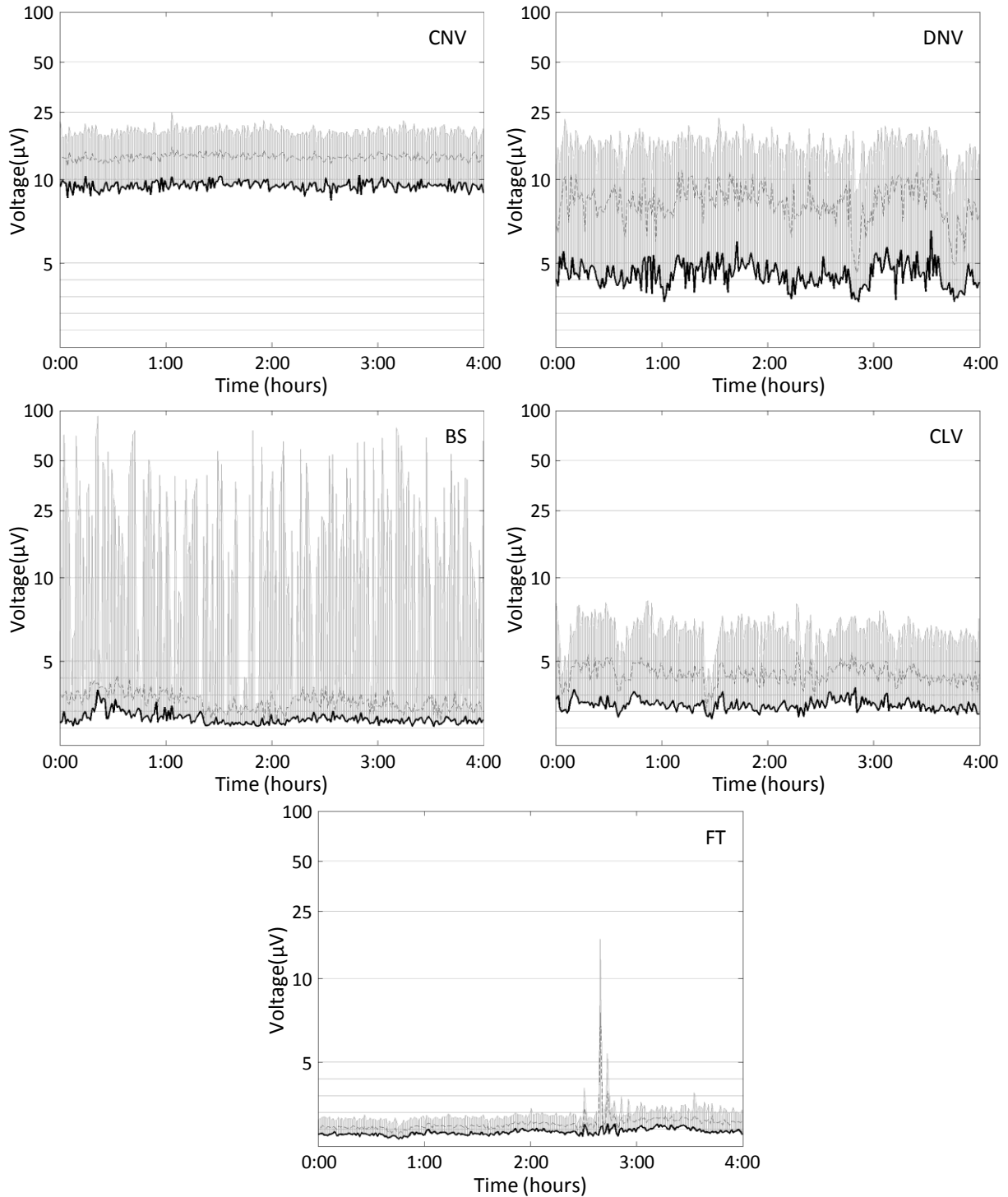


Figure A.1: Example aEEG data showing the five different patterns.

Table A.1: Classification of aEEG background patterns based on lower and upper amplitude limits.

Background	Continuity	Limits (μV)	
		Lower	Upper
CNV	continuous	7-10	10-25
DNV	discontinuous	<5	>10
BS	discontinuous	0-1	>25
CLV	continuous	~ 5	
FT	mainly flat	<<5	

Seizure activity

Seizure activity can be classified as: (i) single seizures, (ii) repetitive seizures or (iii) *status epilepticus* [44]. Repetitive seizures are similar to single seizures, but they occur more frequently than at 30-min intervals. *Status epilepticus* is classified as ongoing seizure activity lasting longer than 30 minutes [43, 44]. The appearance of these three types of seizures in both aEEG and EEG is shown in Figure A.2 and Figure A.3.

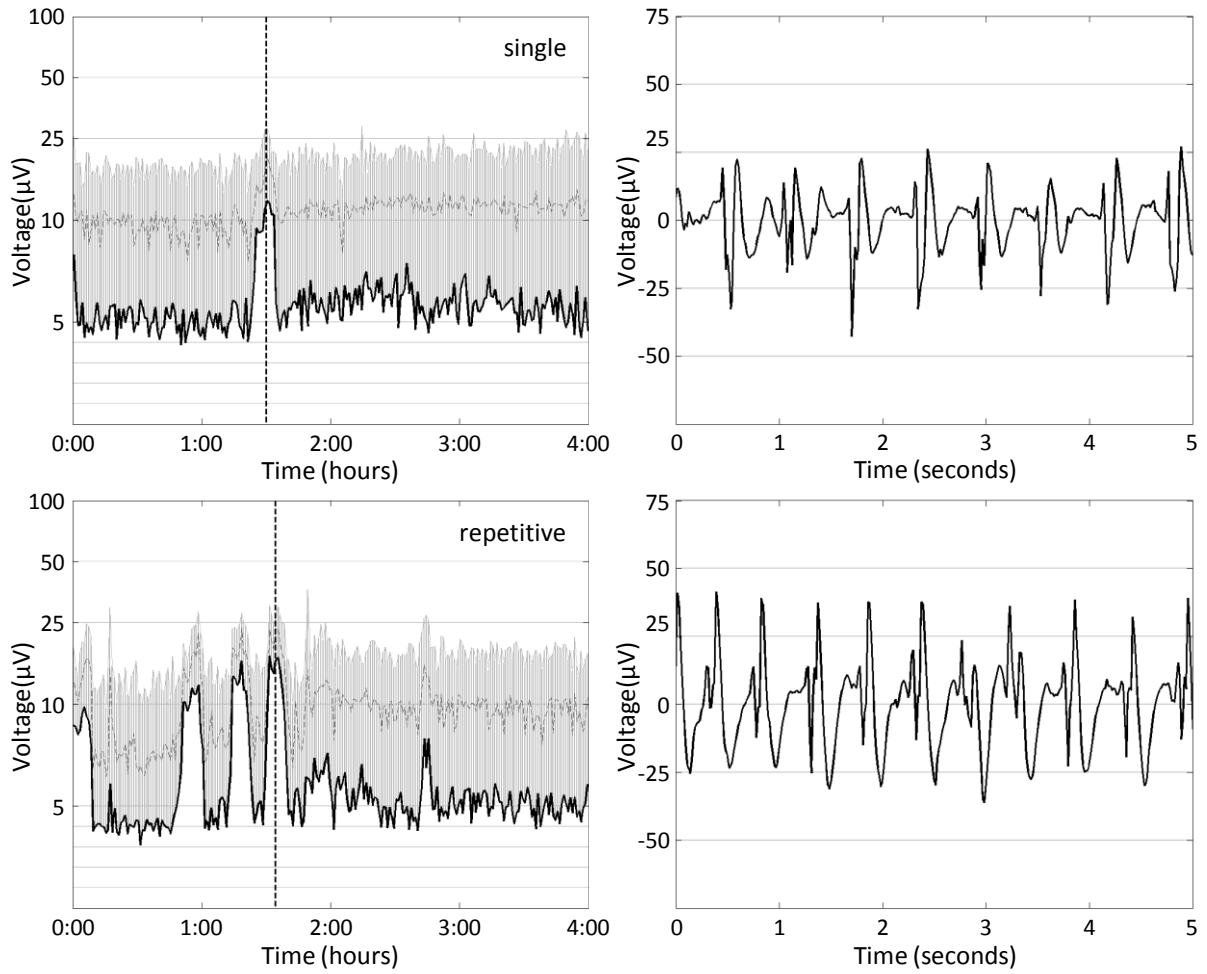


Figure A.2: The appearance of single and repetitive seizures in both aEEG (left) and EEG (right). The dashed line in the aEEG plots marks the position of the EEG segment containing the seizure.

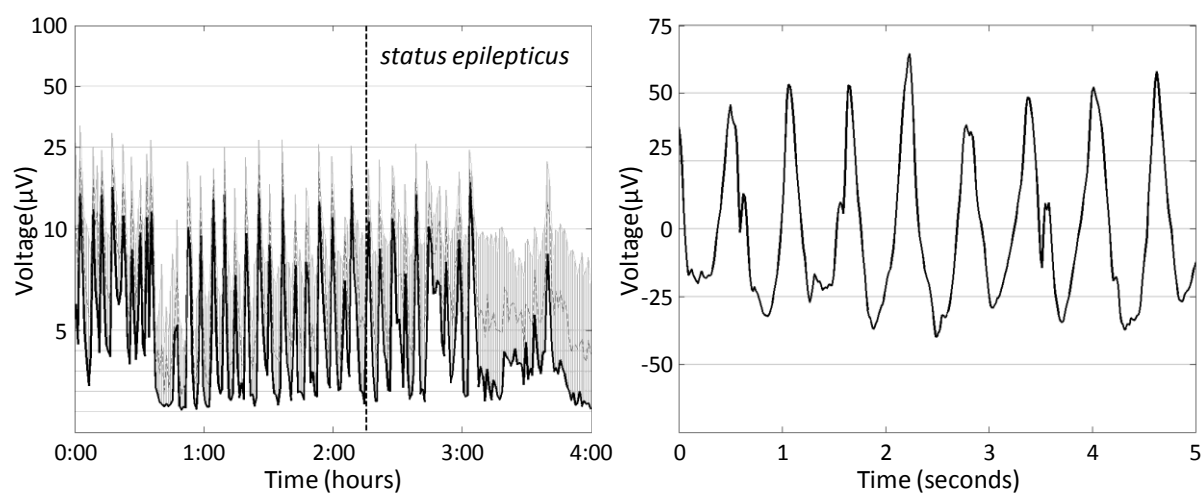


Figure A.3: The appearance of *status epilepticus* in both aEEG (left) and EEG (right). The dashed line in the aEEG plots marks the position of the EEG segment that is displayed.

Appendix B Midazolam spectral power values

Table B.1: Change of spectral parameters following a loading dose of midazolam.

			Baseline value		Normalized value at maximum effect (%)	
			Ipsi	Contra	Ipsi	Contra
Absolute	Σ	[μV^2]	39 (22-52)	30 (26-40)	47 [†] (28-74)	47* (28-67)
	δ	[μV^2]	24 (14-38)	21 (17-30)	41 [†] (25-76)	42* (26-69)
	θ	[μV^2]	7 (4-11)	7 (5-7)	61 (45-93)	54* (40-86)
	α	[μV^2]	2 (1-4)	2 (2-3)	53* (43-66)	50* (26-60)
	β	[μV^2]	2 (1-4)	2 (1-3)	39 [†] (21-77)	25* (11-62)
Relative	δ	[%]	67 (61-72)	66 (61-72)	94 [†] (82-98)	92 [†] (86-97)
	θ	[%]	20 (17-22)	20 (17-23)	138 [†] (112-188)	131* (108-131)
	α	[%]	7 (7-9)	7 (5-9)	91 (84-109)	88 (81-115)
	β	[%]	4 (4-6)	5 (3-8)	79 (71-85)	69 (36-92)
SEF		[Hz]	11 (10-13)	12 (9-15)	90 (86-94)	85 (62-99)

Legend: Changes in spectral parameters after midazolam administration. Baseline and normalized values at maximum effect are given for absolute total power (Σ), absolute and relative frequency band power (δ , θ , α and β) and SEF for ipsilateral (Ipsi) and contralateral (Contra) hemispheres. Values are expressed as median (IQR). Statistical significant changes with baseline values are indicated with: * $p < 0.01$ and [†] $p < 0.05$.

Table B.2: Interhemispheric significance p-values during four hours surrounding midazolam administration.

		hours				normalized to first hour			
		-1	1	2	3	-1	1	2	3
Absolute	Σ	0.461	0.547	0.195	0.313	1.000	0.742	0.945	0.742
	δ	0.461	0.641	0.195	0.461	1.000	0.641	0.945	0.844
	θ	0.641	0.547	0.461	0.250	1.000	0.461	0.844	0.742
	α	0.313	0.250	0.109	0.109	1.000	0.461	1.000	0.461
	β	0.383	0.195	0.195	0.078	1.000	0.383	0.383	0.148
Relative	δ	0.742	0.641	0.742	0.313	1.000	0.547	1.000	0.195
	θ	0.461	0.742	0.461	0.461	1.000	0.844	0.461	0.945
	α	0.383	0.461	0.641	0.148	1.000	0.945	0.641	1.000
	β	0.945	0.148	0.742	0.547	1.000	0.250	0.383	0.641

Legend: Interhemispheric significance p-values are calculated from one hour before until three hours after midazolam administration. This is done for absolute powers, relative powers and normalized absolute/relative powers. Statistical significant changes are defined as: * $p < 0.01$ and [†] $p < 0.05$. No significant differences are present following midazolam administration.

Appendix C Lidocaine spectral power values

Table C.1: Change in spectral parameters following lidocaine administration.

			Baseline value		Normalized value at maximum effect (%)	
			Ipsi	Contra	Ipsi	Contra
Absolute	Σ	[μV^2]	17 (12-23)	13 (10-23)	82 (59-95)	89 (70-121)
	δ	[μV^2]	11 (8-14)	8 (6-16)	73 [†] (51-80)	81 (66-117)
	θ	[μV^2]	4 (4-7)	5 (3-6)	107 (81-127)	92 (75-148)
	α	[μV^2]	1 (1-2)	1 (1-1)	91 (61-123)	102 (70-135)
	β	[μV^2]	1 (0-1)	1 (0-1)	82 (59-105)	122 (72-153)
Relative	δ	[%]	60 (58-66)	58 (47-68)	85* (77-94)	92* (85-97)
	θ	[%]	28 (23-30)	29 (23-38)	135* (125-139)	111* (103-127)
	α	[%]	7 (7-9)	8 (6-10)	120 [†] (102-136)	119* (105-122)
	β	[%]	4 (4-5)	4 (3-5)	106 (87-121)	108* (83-116)
	SEF	[Hz]	17 (12-23)	13 (10-23)	82 (59-95)	89 (70-121)
			11 (8-14)	8 (6-16)	73 [†] (51-80)	81 (66-117)

Legend: Changes in spectral parameters after lidocaine administration. Baseline and normalized values at maximum effect are given for absolute total power (Σ), absolute and relative frequency band power (δ , θ , α and β) and SEF for ipsilateral (Ipsi) and contralateral (Contra) hemispheres. Values are expressed as median (IQR). Statistical significant changes with baseline values are indicated with: * $p < 0.01$ and [†] $p < 0.05$.

Table C.2: Interhemispheric significance p-values during four hours surrounding lidocaine administration.

		hours				normalized to first hour			
		-1	1	2	3	-1	1	2	3
Absolute	Σ	0.275	0.846	1.000	1.000	1.000	0.193	0.193	0.037 [†]
	δ	0.322	0.770	0.922	0.922	1.000	0.105	0.105	0.010*
	θ	0.492	0.625	0.695	0.770	1.000	0.846	0.625	0.275
	α	0.375	0.695	1.000	0.770	1.000	0.432	0.375	0.105
	β	0.375	0.322	0.557	0.492	1.000	0.027	0.846	0.193
Relative	δ	0.232	0.922	0.695	1.000	1.000	0.064	0.049 [†]	0.232
	θ	0.232	0.846	0.922	0.695	1.000	0.002*	0.014 [†]	0.037 [†]
	α	0.375	0.695	0.922	1.000	1.000	0.084	0.232	0.432
	β	0.922	0.695	0.193	0.846	1.000	0.846	0.232	0.557

Legend: Interhemispheric significance p-values are calculated from one hour before until three hours after lidocaine administration for absolute powers, relative powers and normalized absolute/relative powers. Statistical significance is defined as: * $p < 0.01$ and [†] $p < 0.05$. Normalized absolute total and delta power is significantly different in the third hour after lidocaine administration. Normalized relative delta power is significantly changed in the second hour, while normalized relative theta power differs significantly in all hours following lidocaine administration.

Appendix D Literature on EEG spectral effects of AEDs

Table D.1: Changes in spectral parameters following midazolam or lidocaine administration as reported in literature.

		Method	Total	δ		θ		α		β	
			power	abs	rel	abs	rel	abs	rel	abs	rel
Midazolam	Bührer [54]	IV	↑					↓		↑	
	Hering [55]	IV			↓				↑		↑
	Aeschbach [56]	Oral			↓		↓		↑		↑
	Billard [57]	IV			↑						↑
	Feshchenko [58]	Buccal						↑		↑	
	Scott [59]	Buccal			=		=		↑		↑
	Durka [60]	IV		↓		↓				↑	
	<i>Current study</i>	IV	↓	↓	↓	↓	↑	↓	=	↓	=
Lidocaine	Detsch [69]	IV		↑		=		=		↑	
	Madhavan [70]	Cortical			↑		↓		↓		↓
	<i>Current study</i>	IV	=	=	↓	=	↑	=	↑	=	=

Legend: An overview of available studies on EEG spectral effects following administration of either midazolam or lidocaine. All studies are performed on healthy volunteers, with exception of Madhavan *et al.* who focused on patients with focal epilepsy [70]. Administration methods are listed (IV = intravenous), together with absolute total power and absolute and relative frequency band powers. ↑ and ↓ indicate reported increase and decrease, respectively, and = indicates no change

Appendix E The forward problem

The EEG forward problem is defined as

$$\Phi = \mathbf{K}\mathbf{J} \quad \text{Eq. E.1}$$

with $\Phi \in \mathbb{R}^{N_E \times 1}$ a vector containing the electrode potentials measured at N_E extracranial scalp electrodes. The primary current density in the brain $\mathbf{J} \in \mathbb{R}^{(3N_V) \times 1}$ is defined as

$$\mathbf{J} = (\mathbf{J}_1^T, \mathbf{J}_2^T, \mathbf{J}_3^T, \dots, \mathbf{J}_{N_V}^T) \quad \text{Eq. E.2}$$

where $\mathbf{J}_l \in \mathbb{R}^{3 \times 1}$ for $l = 1, \dots, N_V$. At the l^{th} voxel, $\mathbf{J}_l^T = (\mathbf{J}_x^T, \mathbf{J}_y^T, \mathbf{J}_z^T)$ contains the unknown dipole moments, and the superscript ‘T’ denotes the transpose.

The lead field $\mathbf{K} \in \mathbb{R}^{N_E \times (3N_V)}$ contains information about geometry and conductivity of the head model and has the following structure

$$\mathbf{K} = \begin{pmatrix} \mathbf{k}_{1,1} & \cdots & \mathbf{k}_{1,N_V} \\ \vdots & \ddots & \vdots \\ \mathbf{k}_{N_E,1} & \cdots & \mathbf{k}_{N_E,N_V} \end{pmatrix} \quad \text{Eq. E.3}$$

with $\mathbf{k}_{i,l} \in \mathbb{R}^{1 \times 3}$, for $i = 1, \dots, N_E$, and $l = 1, \dots, N_V$. Note $\mathbf{k}_{i,l} = (\mathbf{k}_{i,l}^x, \mathbf{k}_{i,l}^y, \mathbf{k}_{i,l}^z)$ where $\mathbf{k}_{i,l}^x$ is the scalp electric potential at the i^{th} electrode, due to a unit strength X-oriented dipole at the l^{th} voxel, $\mathbf{k}_{i,l}^y$ is the scalp electric potential at the i^{th} electrode, due to a unit strength Y-oriented dipole at the l^{th} voxel, $\mathbf{k}_{i,l}^z$ is the scalp electric potential at the i^{th} electrode, due to a unit strength Z-oriented dipole at the l^{th} voxel.

The source reconstruction models calculate \mathbf{J} from the inverse problem, which follows from Eq. E.1, and apply physiological constraints to the solution space to obtain the electrical source distribution. For the mathematical derivations of LORETA, sLORETA and swLORETA, see their respective publications [16-18].

Bibliography

1. Finer NN, Robertson CM, Richards RT, Pinnell LE, Peters KL (1981) Hypoxic-ischemic encephalopathy in term neonates: perinatal factors and outcome. *J Pediatr* 98:112-117
2. Lynch JK (2009) Epidemiology and classification of perinatal stroke. *Semin Fetal Neonatal Med* 14:245-249
3. Lynch JK, Nelson KB (2001) Epidemiology of perinatal stroke. *Curr Opin Pediatr* 13:499-505
4. Apgar V (1953) A proposal for a new method of evaluation of the newborn infant. *Curr Res Anesth Analg* 32:260-267
5. Sarnat HB, Sarnat MS (1976) Neonatal encephalopathy following fetal distress. A clinical and electroencephalographic study. *Arch Neurol* 33:696-705
6. Neil JJ, Inder TE (2004) Imaging perinatal brain injury in premature infants. *Semin Perinatol* 28:433-443
7. Toet MC, Hellstrom-Westas L, Groenendaal F, Eken P, de Vries LS (1999) Amplitude integrated EEG 3 and 6 hours after birth in full term neonates with hypoxic-ischaemic encephalopathy. *Arch Dis Child Fetal Neonatal Ed* 81:F19-F23
8. Holmes G, Rowe J, Hafford J, Schmidt R, Testa M, Zimmerman A (1982) Prognostic value of the electroencephalogram in neonatal asphyxia. *Electroencephalogr Clin Neurophysiol* 53:60-72
9. Leijser LM, Vein AA, Liauw L, Strauss T, Veen S, Wezel-Meijler G (2007) Prediction of short-term neurological outcome in full-term neonates with hypoxic-ischaemic encephalopathy based on combined use of electroencephalogram and neuro-imaging. *Neuropediatrics* 38:219-227
10. Wertheim D, Mercuri E, Faundez JC, Rutherford M, Acolet D, Dubowitz L (1994) Prognostic value of continuous electroencephalographic recording in full term infants with hypoxic ischaemic encephalopathy. *Arch Dis Child* 71:F97-102
11. ter Horst HJ, Sommer C, Bergman KA, Fock JM, van Weerden TW, Bos AF (2004) Prognostic significance of amplitude-integrated EEG during the first 72 hours after birth in severely asphyxiated neonates. *Pediatr Res* 55:1026-1033
12. Hellstrom-Westas L, Rosén I, Svenningsen NW (1995) Predictive value of early continuous amplitude integrated EEG recordings on outcome after severe birth asphyxia in full term infants. *Arch Dis Child Fetal Neonatal Ed* 72:F34-F38
13. Ronen GM, Buckley D, Penney S, Streiner DL (2007) Long-term prognosis in children with neonatal seizures: a population-based study. *Neurology* 69:1816-1822
14. Dzhalal VI, Staley KJ (2003) Excitatory actions of endogenously released GABA contribute to initiation of ictal epileptiform activity in the developing hippocampus. *J Neurosci* 23:1840-1846

15. Holmes GL, Ben-Ari Y (1998) Seizures in the developing brain: perhaps not so benign after all. *Neuron* 21:1231-1234
16. Pascual-Marqui RD, Michel CM, Lehmann D (1994) Low resolution electromagnetic tomography: a new method for localizing electrical activity in the brain. *Int J Psychophysiol* 18:49-65
17. Pascual-Marqui RD, R.D. (2002) Standardized low-resolution brain electromagnetic tomography (sLORETA): Technical details.8
18. Palmero-Soler E, Dolan K, Hadamschek V, Tass PA (2007) swLORETA: a novel approach to robust source localization and synchronization tomography. *Phys Med Biol* 52:1783-1800
19. Roche-Labarbe N, Aarabi A, Kongolo G, Gondry-Jouet C, Dumpelmann M, Grebe R, Wallois F (2008) High-resolution electroencephalography and source localization in neonates. *Hum Brain Mapp* 29:167-176
20. Doya K (2000) Complementary roles of basal ganglia and cerebellum in learning and motor control. *Curr Opin Neurobiol* 10:732-739
21. Allen G, Buxton RB, Wong EC, Courchesne E (1997) Attentional activation of the cerebellum independent of motor involvement. *Science* 275:1940-1943
22. Lotze M, Montoya P, Erb M, Hulsmann E, Flor H, Klose U, Birbaumer N, Grodd W (1999) Activation of cortical and cerebellar motor areas during executed and imagined hand movements: an fMRI study. *J Cogn Neurosci* 11:491-501
23. Packard MG, Knowlton BJ (2002) Learning and memory functions of the Basal Ganglia. *Annu Rev Neurosci* 25:563-593
24. DeLong MR, Alexander GE, Georgopoulos AP, Crutcher MD, Mitchell SJ, Richardson RT (1984) Role of basal ganglia in limb movements. *Hum Neurobiol* 2:235-244
25. Alexander GE, Crutcher MD (1990) Preparation for movement: neural representations of intended direction in three motor areas of the monkey. *J Neurophysiol* 64:133-150
26. Healthline Networks Inc. (2012) Healthline BodyMaps™. Retrieved February 2, 2012, from <http://www.healthline.com/human-body-maps/thalamus#3/1>
27. Hodgkin AL, Huxley AF (1952) A quantitative description of membrane current and its application to conduction and excitation in nerve. *J Physiol* 117:500-544
28. Olejniczak P (2006) Neurophysiologic basis of EEG. *J Clin Neurophysiol* 23:186-189
29. Hämäläinen M, Hari R, Ilmoniemi RJ, Knuutila J, Lounasmaa OV (1993) Magnetoencephalography-theory, instrumentation, and applications to noninvasive studies of the working human brain. *Reviews of Modern Physics* 65:413-497
30. Steriade M, Llinas RR (1988) The functional states of the thalamus and the associated neuronal interplay. *Physiol Rev* 68:649-742

31. Jasper HH (1958) Report of the committee on methods of clinical examination in electroencephalography. *Electroencephalography and Clinical Neurophysiology* 10:370-375
32. Klem GH, Luders HO, Jasper HH, Elger C (1999) The ten-twenty electrode system of the International Federation. *The International Federation of Clinical Neurophysiology. Electroencephalogr Clin Neurophysiol Suppl* 52:3-6
33. Biagioni E, Boldrini A, Bottone U, Pieri R, Cioni G (1996) Prognostic value of abnormal EEG transients in preterm and full-term neonates. *Electroencephalogr Clin Neurophysiol* 99:1-9
34. Maynard DE, Prior PF, Scott DF (1969) Device for continuous monitoring of cerebral activity in resuscitated patients. *Br Med J* 4:545-546
35. Prior PF, Maynard DE, Sheaff PC, Simpson BR, Strunin L, Weaver EJ, Scott DF (1971) Monitoring cerebral function: clinical experience with new device for continuous recording of electrical activity of brain. *Br Med J* 2:736-738
36. al Naqeeb N, Edwards AD, Cowan FM, Azzopardi D (1999) Assessment of neonatal encephalopathy by amplitude-integrated electroencephalography. *Pediatrics* 103:1263-1271
37. Toet MC, van Rooij LG, de Vries LS (2008) The use of amplitude integrated electroencephalography for assessing neonatal neurologic injury. *Clin Perinatol* 35:665-78, v
38. Hellstrom-Westas L, Westgren U, Rosén I, Svenningsen NW (1988) Lidocaine for treatment of severe seizures in newborn infants. I. Clinical effects and cerebral electrical activity monitoring. *Acta Paediatr Scand* 77:79-84
39. van Leuven K, Groenendaal F, Toet MC, Schobben AF, Bos SA, de Vries LS, Rademaker CM (2004) Midazolam and amplitude-integrated EEG in asphyxiated full-term neonates. *Acta Paediatr* 93:1221-1227
40. ter Horst HJ, Brouwer OF, Bos AF (2004) Burst suppression on amplitude-integrated electroencephalogram may be induced by midazolam: a report on three cases. *Acta Paediatr* 93:559-563
41. Shany E, Benzaquen O, Friger M, Richardson J, Golan A (2008) Influence of antiepileptic drugs on amplitude-integrated electroencephalography. *Pediatr Neurol* 39:387-391
42. de Vries LS, Toet MC (2006) Amplitude Integrated Electroencephalography in the Full-Term Newborn. *Clinics in Perinatology* 33:619-632
43. Hellstrom-Westas L, Rosén I (2006) Continuous brain-function monitoring: state of the art in clinical practice. *Semin Fetal Neonatal Med* 11:503-511
44. Hellstrom-Westas L, Rosén I, de Vries LS, Greisen G (2006) Amplitude-integrated EEG Classification and Interpretation in Preterm and Term Infants. *NeoReviews* 7:e76-e87

45. Cooley J, Tukey J (1965) An Algorithm for the Machine Calculation of Complex Fourier Series. *Mathematics of Computation* 19:297-301
46. Schoukens J, Rolain Y, Pintelon R (2006) Analysis of windowing/leakage effects in frequency response function measurements. *Automatica* 42:27-38
47. Philips CL, Parr JM, Riskin EA (2002) *Signals, Systems, and Transforms*. Prentice Hall, New Jersey.
48. Harris FJ (1978) On the use of windows for harmonic analysis with the discrete Fourier transform. *Proceedings of the IEEE* 66:51-83
49. Butterworth S (1930) On the Theory of Filter Amplifiers. *Experimental Wireless & the Wireless Engineer* 7:536-541
50. Oppenheim AV, Schaffer RW, Buck JR (1999) *Discrete-Time Signal Processing*. Prentice Hall, New Jersey.
51. Hatskevich CW, Itkis ML, Maloletnev VI (1992) Off-Line Methods for Detection and Correction of Eeg Artifacts of Various Origin. *International Journal of Psychophysiology* 12:179-185
52. Young GB, Campbell VC (1999) EEG monitoring in the intensive care unit: Pitfalls and caveats. *Journal of Clinical Neurophysiology* 16:40-45
53. Benbadis SR, Rielo D (2010) EEG Artifacts. Retrieved January 15, 2012, from <http://emedicine.medscape.com/article/1140247-overview#showall>
54. Buhner M, Maitre PO, Hung O, Stanski DR (1990) Electroencephalographic effects of benzodiazepines. I. Choosing an electroencephalographic parameter to measure the effect of midazolam on the central nervous system. *Clin Pharmacol Ther* 48:544-554
55. Hering W, Geisslinger G, Kamp HD, Dinkel M, Tschaikowsky K, Rugheimer E, Brune K (1994) Changes in the EEG power spectrum after midazolam anaesthesia combined with racemic or S- (+) ketamine. *Acta Anaesthesiol Scand* 38:719-723
56. Aeschbach D, Dijk DJ, Trachsel L, Brunner DP, Borbely AA (1994) Dynamics of slow-wave activity and spindle frequency activity in the human sleep EEG: effect of midazolam and zopiclone. *Neuropsychopharmacology* 11:237-244
57. Billard V, Gambus PL, Chamoun N, Stanski DR, Shafer SL (1997) A comparison of spectral edge, delta power, and bispectral index as EEG measures of alfentanil, propofol, and midazolam drug effect. *Clin Pharmacol Ther* 61:45-58
58. Feshchenko VA, Veselis RA, Reinsel RA (1997) Comparison of the EEG effects of midazolam, thiopental, and propofol: the role of underlying oscillatory systems. *Neuropsychobiology* 35:211-220
59. Scott RC, Besag FM, Boyd SG, Berry D, Neville BG (1998) Buccal absorption of midazolam: pharmacokinetics and EEG pharmacodynamics. *Epilepsia* 39:290-294

60. Durka PJ, Szelenberger W, Blinowska KJ, Androsiuk W, Myszka M (2002) Adaptive time-frequency parametrization in pharmaco EEG. *J Neurosci Methods* 117:65-71
61. Silverstein FS, Jensen FE (2007) Neonatal seizures. *Ann Neurol* 62:112-120
62. Sato H (1980) Relationship between serum levels and fast EEG activities in rats by a single administration of phenobarbital. *Electroencephalogr Clin Neurophysiol* 50:509-514
63. Schwarz E, Kielholz P, Hobi V, Goldberg L, Hofstetter M, Ladewig D (1982) Changes in EEG, blood levels, mood scales and performance scores during long term treatment with diazepam, phenobarbital or placebo in patients. *Prog Neuropsychopharmacol Biol Psychiatry* 6:249-263
64. Pitlick W, Painter M, Pippenger C (1978) Phenobarbital pharmacokinetics in neonates. *Clin Pharmacol Ther* 23:346-350
65. Touw DJ, Graafland O, Cranendonk A, Vermeulen RJ, van Weissenbruch MM (2000) Clinical pharmacokinetics of phenobarbital in neonates. *Eur J Pharm Sci* 12:111-116
66. Boylan GB, Rennie JM, Chorley G, Pressler RM, Fox GF, Farrer K, Morton M, Binnie CD (2004) Second-line anticonvulsant treatment of neonatal seizures: a video-EEG monitoring study. *Neurology* 62:486-488
67. Dundee JW, Collier PS, Carlisle RJ, Harper KW (1986) Prolonged midazolam elimination half-life. *Br J Clin Pharmacol* 21:425-429
68. Butterworth JF, Strichartz GR (1990) Molecular mechanisms of local anesthesia: a review. *Anesthesiology* 72:711-734
69. Detsch O, Erkens U, Jacofsky U, Thiel A, Kochs E, Hempelmann G (1997) Topographical analysis of the EEG effects of a subconvulsive dose of lidocaine in healthy volunteers. *Acta Anaesthesiol Scand* 41:1039-1046
70. Madhavan D, Mirowski P, Ludvig N, Carlson C, Doyle W, Devinsky O, Kuzniecky R (2008) Effects of subdural application of lidocaine in patients with focal epilepsy. *Epilepsy Res* 78:235-239
71. LeLorier J, Grenon D, Latour Y, Caille G, Dumont G, Brosseau A, Solignac A (1977) Pharmacokinetics of lidocaine after prolonged intravenous infusions in uncomplicated myocardial infarction. *Ann Intern Med* 87:700-706
72. Scriver CR, Hutchison JH (1963) The vitamin B6 deficiency syndrome in human infancy: biochemical and clinical observations. *Pediatrics* 31:240-250
73. Maartens IA, Wassenberg T, Buijs J, Bok L, de Kleine MJ, Katgert T, Andriessen P (2011) Neurodevelopmental outcome in full-term newborns with refractory neonatal seizures. *Acta Paediatr*
74. Malingre MM, van Rooij LG, Rademaker CM, Toet MC, Ververs TF, van KC, de Vries LS (2006) Development of an optimal lidocaine infusion strategy for neonatal seizures. *Eur J Pediatr* 165:598-604

75. van den Broek MP, Huitema AD, van Hasselt JG, Groenendaal F, Toet MC, Egberts TC, de Vries LS, Rademaker CM (2011) Lidocaine (lignocaine) dosing regimen based upon a population pharmacokinetic model for preterm and term neonates with seizures. *Clin Pharmacokinet* 50:461-469
76. van de Velde M, van Erp G, Cluitmans PJ (1998) Detection of muscle artefact in the normal human awake EEG. *Electroencephalogr Clin Neurophysiol* 107:149-158
77. Janssen F (2011) A quantitative analysis of EEG parameters in full-term neonates with unilateral stroke. Master's thesis, Eindhoven University of Technology
78. Lilliefors HW (1967) On the Kolmogorov-Smirnov test for normality with mean and variance unknown. *Journal of the American Statistical Association* 62:399-402
79. Wilcoxon F (1945) Individual Comparisons by Ranking Methods. *Biometrics Bulletin* 1:80-83
80. Shany E, Benzaquen O, Watemberg N (2007) Comparison of continuous drip of midazolam or lidocaine in the treatment of intractable neonatal seizures. *J Child Neurol* 22:255-259
81. De Giorgio CM, Altman K, Hamilton-Byrd E, Rabinowicz AL (1992) Lidocaine in refractory status epilepticus: confirmation of efficacy with continuous EEG monitoring. *Epilepsia* 33:913-916
82. Vakorin VA, Lippe S, McIntosh AR (2011) Variability of brain signals processed locally transforms into higher connectivity with brain development. *J Neurosci* 31:6405-6413
83. Neil J, Miller J, Mukherjee P, Huppi PS (2002) Diffusion tensor imaging of normal and injured developing human brain - a technical review. *NMR Biomed* 15:543-552
84. Yakovlev PI, Lecours AR (1967) The Myelogenetic Cycle of Regional Maturation of the Brain. In: Minkowski A (ed) *Regional Development of the Brain in Early Life*. Blackwell, Oxford, pp 3-70.
85. Ribeiro MA, Costa PF (2003) The sensitivity of sodium channels in immature and mature rat CA1 neurones to the local anaesthetics procaine and lidocaine. *Brain Res Dev Brain Res* 146:59-70
86. Connell J, Oozeer R, de VL, Dubowitz LM, Dubowitz V (1989) Clinical and EEG response to anticonvulsants in neonatal seizures. *Arch Dis Child* 64:459-464
87. Castro Conde JR, Hernandez Borges AA, Domenech ME, Gonzalez CC, Perera SR (2005) Midazolam in neonatal seizures with no response to phenobarbital. *Neurology* 64:876-879
88. Mandema JW, Tukker E, Danhof M (1991) Pharmacokinetic-pharmacodynamic modelling of the EEG effects of midazolam in individual rats: influence of rate and route of administration. *Br J Pharmacol* 102:663-668

89. Pisani F, Sisti L, Seri S (2009) A scoring system for early prognostic assessment after neonatal seizures. *Pediatrics* 124:e580-e587
90. Rennie JM, Boylan GB (2003) Neonatal seizures and their treatment. *Curr Opin Neurol* 16:177-181
91. Tekgul H, Gauvreau K, Soul J, Murphy L, Robertson R, Stewart J, Volpe J, Bourgeois B, du Plessis AJ (2006) The current etiologic profile and neurodevelopmental outcome of seizures in term newborn infants. *Pediatrics* 117:1270-1280
92. van Pul C, Buijs J, Vilanova A, Roos FG, Wijn PF (2006) Infants with perinatal hypoxic ischemia: feasibility of fiber tracking at birth and 3 months. *Radiology* 240:203-214
93. Pascual-Marqui RD, Esslen M, Kochi K, Lehmann D (2002) Functional imaging with low-resolution brain electromagnetic tomography (LORETA): a review. *Methods Find Exp Clin Pharmacol* 24 Suppl C:91-95
94. Llinas RR (1988) The intrinsic electrophysiological properties of mammalian neurons: insights into central nervous system function. *Science* 242:1654-1664
95. Haalman I, Vaadia E (1997) Dynamics of neuronal interactions: relation to behavior, firing rates, and distance between neurons. *Hum Brain Mapp* 5:249-253
96. Sukov W, Barth DS (1998) Three-dimensional analysis of spontaneous and thalamically evoked gamma oscillations in auditory cortex. *J Neurophysiol* 79:2875-2884
97. Clemens B, Piros P, Bessenyei M, Varga E, Puskas S, Fekete I (2009) The electrophysiological "delayed effect" of focal interictal epileptiform discharges. A low resolution electromagnetic tomography (LORETA) study. *Epilepsy Res* 85:270-278
98. Clemens B, Bessenyei M, Fekete I, Puskas S, Kondakor I, Toth M, Hollody K (2010) Theta EEG source localization using LORETA in partial epilepsy patients with and without medication. *Clin Neurophysiol* 121:848-858
99. Lantz G, Michel CM, Pascual-Marqui RD, Spinelli L, Seeck M, Seri S, Landis T, Rosen I (1997) Extracranial localization of intracranial interictal epileptiform activity using LORETA (low resolution electromagnetic tomography). *Electroencephalogr Clin Neurophysiol* 102:414-422
100. Puskas S, Bessenyei M, Fekete I, Hollody K, Clemens B (2010) Quantitative EEG abnormalities in persons with "pure" epileptic predisposition without epilepsy: a low resolution electromagnetic tomography (LORETA) study. *Epilepsy Res* 91:94-100
101. Zumsteg D, Andrade DM, Wennberg RA (2006) Source localization of small sharp spikes: low resolution electromagnetic tomography (LORETA) reveals two distinct cortical sources. *Clin Neurophysiol* 117:1380-1387
102. Clemens B, Bank J, Piros P, Bessenyei M, Veto S, Toth M, Kondakor I (2008) Three-dimensional localization of abnormal EEG activity in migraine: a low resolution

- electromagnetic tomography (LORETA) study of migraine patients in the pain-free interval. *Brain Topogr* 21:36-42
103. Gianotti LR, Kunig G, Lehmann D, Faber PL, Pascual-Marqui RD, Kochi K, Schreiter-Gasser U (2007) Correlation between disease severity and brain electric LORETA tomography in Alzheimer's disease. *Clin Neurophysiol* 118:186-196
 104. Painold A, Anderer P, Holl AK, Letmaier M, Saletu-Zyhlarz GM, Saletu B, Bonelli RM (2011) EEG low-resolution brain electromagnetic tomography (LORETA) in Huntington's disease. *J Neurol* 258:840-854
 105. Maurage P, Philippot P, Joassin F, Pauwels L, Pham T, Prieto EA, Palmero-Soler E, Zanow F, Campanella S (2008) The auditory-visual integration of anger is impaired in alcoholism: an event-related potentials study. *J Psychiatry Neurosci* 33:111-122
 106. Bocquillon P, Bourriez JL, Palmero-Soler E, Betrouni N, Houdayer E, Derambure P, Dujardin K (2011) Use of swLORETA to localize the cortical sources of target- and distracter-elicited P300 components. *Clin Neurophysiol* 122:1991-2002
 107. Holmes CJ, Hoge R, Collins L, Woods R, Toga AW, Evans AC (1998) Enhancement of MR images using registration for signal averaging. *J Comput Assist Tomogr* 22:324-333
 108. Geddes LA, Baker LE (1967) The specific resistance of biological material--a compendium of data for the biomedical engineer and physiologist. *Med Biol Eng* 5:271-293
 109. Goncalves S, de Munck JC, Verbunt JP, Heethaar RM, da Silva FH (2003) In vivo measurement of the brain and skull resistivities using an EIT-based method and the combined analysis of SEF/SEP data. *IEEE Trans Biomed Eng* 50:1124-1128
 110. Thordstein M, Flisberg A, Lofgren N, Bagenholm R, Lindecrantz K, Wallin BG, Kjellmer I (2004) Spectral analysis of burst periods in EEG from healthy and post-asphyctic full-term neonates. *Clin Neurophysiol* 115:2461-2466
 111. Inder TE, Buckland L, Williams CE, Spencer C, Gunning MI, Darlow BA, Volpe JJ, Gluckman PD (2003) Lowered electroencephalographic spectral edge frequency predicts the presence of cerebral white matter injury in premature infants. *Pediatrics* 111:27-33
 112. Mirkovic N, Adjouadi M, Yaylali I, Jayakar P (2003) 3-d source localization of epileptic foci integrating EEG and MRI data. *Brain Topogr* 16:111-119
 113. Claassen J, Jette N, Chum F, Green R, Schmidt M, Choi H, Jirsch J, Frontera JA, Connolly ES, Emerson RG, Mayer SA, Hirsch LJ (2007) Electrographic seizures and periodic discharges after intracerebral hemorrhage. *Neurology* 69:1356-1365
 114. Koelfen W, Freund M, Varnholt V (1995) Neonatal stroke involving the middle cerebral artery in term infants: clinical presentation, EEG and imaging studies, and outcome. *Dev Med Child Neurol* 37:204-212

115. Thatcher RW, North D, Biver C (2007) Intelligence and EEG current density using low-resolution electromagnetic tomography (LORETA). *Hum Brain Mapp* 28:118-133
116. Collins DL, Neelin P, Peters TM, Evans AC (1994) Automatic 3D intersubject registration of MR volumetric data in standardized Talairach space. *J Comput Assist Tomogr* 18:192-205
117. Mazziotta JC, Toga AW, Evans A, Fox P, Lancaster J (1995) A probabilistic atlas of the human brain: theory and rationale for its development. The International Consortium for Brain Mapping (ICBM). *Neuroimage* 2:89-101
118. Towle VL, Bolanos J, Suarez D, Tan K, Grzeszczuk R, Levin DN, Cakmur R, Frank SA, Spire JP (1993) The spatial location of EEG electrodes: locating the best-fitting sphere relative to cortical anatomy. *Electroencephalogr Clin Neurophysiol* 86:1-6
119. de Munck JC, Vijn PC, Spekreijse H (1991) A practical method for determining electrode positions on the head. *Electroencephalogr Clin Neurophysiol* 78:85-87
120. Law SK, Nunez PL (1991) Quantitative representation of the upper surface of the human head. *Brain Topogr* 3:365-371
121. Hellström B, Karlsson B, Müssbichler H (1963) Electrode placement in EEG of infants and its anatomical relationship studied radiographically. *Electroencephalogr Clin Neurophysiol* 15:115-117
122. Ilmoniemi RJ (1995) Estimating brain source distributions: Comments on LORETA. *ISBET Newsletter* 6:12-14
123. Pascual-Marqui RD (1995) Reply to comments by Hämäläinen, Ilmoniemi, and Nunez. *ISBET Newsletter* 6:12-14